Department of Applied Physics

Nitrogen-doped single-walled carbon nanotube thin films

Toma Susi

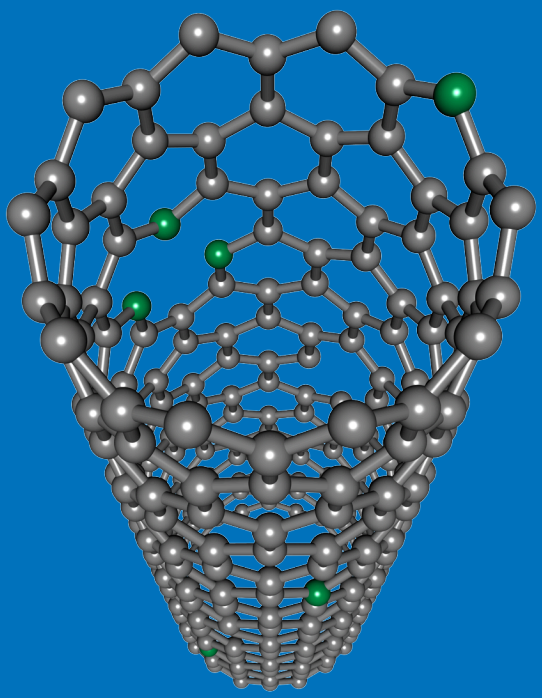

Aalto University

DOCTORAL DISSERTATIONS

Aalto University publication series
DOCTORAL DISSERTATIONS 41/2011

Nitrogen-doped single-walled carbon nanotube thin films

Toma Susi

Doctoral dissertation for the degree of Doctor of Science in Technology (Doctor of Philosophy) to be presented with due permission of the School of Science for public examination and debate in Auditorium T2 of the Computer Science Building of the Aalto University School of Science (Espoo, Finland) on the 20th of May 2011 at 12 noon.

Aalto University
School of Science
Department of Applied Physics
NanoMaterials Group

Supervisor
Prof. Esko I. Kauppinen

Instructor
Dr. Albert G. Nasibulin

Preliminary examiners
Dr. Christopher Ewels, IMN, Universite de Nantes, France
Dr. Avetik R. Harutyunyan, Honda Research Institute, USA

Opponent
Prof. Mauricio Terrones, Penn State University, USA

Aalto University publication series
DOCTORAL DISSERTATIONS 41/2011

ISBN 978-952-60-4124-7 (pdf)
ISBN 978-952-60-4123-0 (printed)
ISSN-L 1799-4934
ISSN 1799-4942 (pdf)
ISSN 1799-4934 (printed)

Aalto Print
Helsinki 2011

Finland

The dissertation can be read at http://lib.tkk.fi/Diss/

Publication orders (printed book):
julkaisut@aalto.fi

Author
Toma Susi

Name of the doctoral dissertation
Nitrogen-doped single-walled carbon nanotube thin films

Publisher School of Science

Unit Department of Applied Physics

Series Aalto University publication series DOCTORAL DISSERTATIONS 41/2011

Field of research Nanomaterials

Manuscript submitted 8 April 2011 **Manuscript revised** 3 May 2011

Date of the defence 20 May 2011 **Language** English

☐ **Monograph** ☒ **Article dissertation (summary + original articles)**

Abstract

Carbon nanotubes are one of the most exciting materials for emerging practical nanotechnologies. However, a significant issue for applications is the mixture of semiconducting and metallic tubes in all typical samples. One of the proposed solutions for this problem is to tailor the electronic structure by doping the lattice with heteroatoms, most notably nitrogen.

In this thesis, nitrogen-doped single-walled carbon nanotubes (N-SWCNTs) were synthesized using an ambient pressure floating catalyst chemical vapor deposition method. A novel combination of precursors was used, with carbon monoxide (CO) acting as the carbon source and ammonia (NH_3) as the nitrogen source. Experiments were conducted with two reactor setups, both utilizing iron nanoparticles as the catalysts. The material was deposited as grown directly from the gas phase as films on various substrates and subsequently characterized by a variety of microscopic and spectroscopic methods, as well as sheet resistance measurements.

The sheet resistance measurements of the thin film samples revealed that the doped films had unexpectedly high resistances. To understand this effect, a resistor network model was developed, which allowed the disentanglement of the contribution of bundle–bundle contacts when combined with data for undoped films. Assuming doping does not significantly change the contacts, the increased resistances of the doped films are likely due to enhanced carrier scattering by defect sites in the nanotubes. This work represents the first experimental report on macroscopic N-SWCNT thin films.

Finally, the mechanism of the initial stages of N-SWCNT growth was studied for the first time by tandem infrared and mass spectrometry gas measurements and first principles electronic-structure calculations. We investigated the bonding and chemistry of CO, NH_3, and their fragments on a model Fe_{55} icosahedral cluster. A possible dissociation path for NH_3 to atomic nitrogen and hydrogen was identified, with a reaction barrier consistent with an experimentally determined value. Both C–C and C–N bond formation reactions were found to be barrierless and exothermic, while a parasitic reaction of hydrogen cyanide formation had a large barrier of over 1 eV.

Keywords nitrogen doping, SWCNT, chirality control, electode, growth mechanism

ISBN (printed) 978-952-60-4123-0 **ISBN (pdf)** 978-952-60-4124-7

ISSN-L 1799-4934 **ISSN (printed)** 1799-4934 **ISSN (pdf)** 1799-4942

Location of publisher Espoo **Location of printing** Helsinki **Year** 2011

Pages 99 **The dissertation can be read at** http://lib.tkk.fi/Diss/

Aalto-yliopisto

Tiivistelmä

Aalto-yliopisto, PL 11000, 00076 Aalto www.aalto.fi

Tekijä
Toma Susi

Väitöskirjan nimi
Typpiseostettujen yksiseinäisten hiilinanoputkien ohutkalvot

Julkaisija Perustieteiden korkeakoulu

Yksikkö Teknillisen fysiikan laitos

Sarja Aalto University publication series DOCTORAL DISSERTATIONS 41/2011

Tutkimusala Nanomateriaalit

Käsikirjoituksen pvm 08.04.2011 **Korjatun käsikirjoituksen pvm** 03.05.2011

Väitöspäivä 20.05.2011 **Kieli** Englanti

☐ **Monografia** ☒ **Yhdistelmäväitöskirja (yhteenveto-osa + erillisartikkelit)**

Tiivistelmä

Hiilinanoputket ovat yksi mielenkiintoisimmista materiaaleista käytännön nanoteknologiassa. Tyypillisten näytteiden sisältämä sekoitus puolijohtavia ja metallisia putkia on kuitenkin merkittävä ongelma sovellusten kannalta. Eräs ehdotettu ratkaisu on niiden sähköisten ominaisuuksien räätälöinti seostamalla hilaa typpiatomeilla.

Tässä väitöskirjassa typpisaostettuja yksiseinäisiä hiilinanoputkia (N-SWCNT) syntetisoitiin käyttäen ympäristön paineessa kelluvilla katalyyteillä tapahtuvaa kemiallista kaasufaasikasvatusta. Hiilimonoksidi (CO) ja ammoniakki (NH_3), joiden yhdistelmää ei oltu aiemmin kokeiltu, toimivat hiili- ja typpiatomien lähtöaineina. Kokeet suoritettiin käyttäen kahta reaktorijärjestelyä, joissa molemmissa hyödynnettiin raudan nanohiukkasia katalyytteinä. Tuotettu materiaali kerättiin sellaisenaan suoraan kaasufaasista eri alustoille ohutkalvoiksi, jotka karakterisoitiin useilla mikroskooppisilla ja spektroskooppisilla menetelmillä sekä kalvoresistanssimittauksilla.

Ohutkalvonäytteiden resistanssimittaukset paljastivat, että typellä saostetuista nanoputkista muodostuneilla kalvoilla oli odottamattoman korkeat resistanssit. Tämän ilmiön ymmärtämiseksi kehitettiin resistoriverkkomalli, joka mahdollisti nanoputkikimppujen välisten kontaktien osuuden selvittämisen, kun malli yhdistettiin saostamattomista kalvoista kerättyyn dataan. Jos oletetaan, että saostus ei merkittävästi muuta nanoputkikimppujen kontakeja, saostettujen kalvojen suurentuneet resistanssit ovat todennäköisesti selitettävissä varauksenkuljettajien voimistuneella sironnalla nanoputkien hilavirheistä. Tämä työ edustaa ensimmäistä kokeellista tutkimusta makroskooppisista N-SWCNT ohutkalvoista.

Lopuksi tutkittiin ensimmäistä kertaa N-SWCNT kasvun alustavia vaiheita käyttäen samanaikaista infrapuna- ja massaspektrometriaa sekä kvanttimekaanisia elektronirakennelaskuja. Niillä tutkittiin CO- ja NH_3-molekyylien ja niiden fragmenttien sitoutumista ja kemiaa ikosaedrisella Fe_{55} mallihiukkasella. Ammoniakin mahdollinen dissosiaatiopolku atomaariseksi typeksi ja vedyksi tunnistettiin, ja sen reaktiovalli oli yhtäpitävä kokeellisesti määritetyn arvon kanssa. Sekä C–C että C–N sidosten muodostumisreaktiot olivat esteettömiä ja eksotermisiä, minkä sijaan loisreaktiolla, vetysyanidin muodostumisella, oli yli yhden elektronivoltin reaktiovalli.

Avainsanat typpiseostus, SWCNT, kiraliteetin hallinta, elektrodi, kasvumekanismi

ISBN (painettu) 978-952-60-4123-0 **ISBN (pdf)** 978-952-60-4124-7

ISSN-L 1799-4934 **ISSN (painettu)** 1799-4934 **ISSN (pdf)** 1799-4942

Julkaisupaikka Espoo **Painopaikka** Helsinki **Vuosi** 2011

Sivumäärä 99 **Luettavissa verkossa osoitteessa** http://lib.tkk.fi/Diss/

People miss the enrichment that just a basic knowledge of the physical world can bring to the most ordinary experiences. It's like there's a pulsating, hidden world, governed by ancient laws and principles, underlying everything around us – from the movements of electrical charges to the motions of planets – and most people are completely unaware of it. To me that's a shame.

–Carolyn Porco

We live on an insignificant planet of a humdrum star lost in a galaxy tucked away in some forgotten corner of a Universe in which there are far more galaxies than people. We make our World significant by the courage of our questions, and by the depth of our answers.

–Carl Sagan

The state of mind which enables a man to do work of this kind is akin to that of the religious worshiper or the lover; the daily effort comes from no deliberate intention or program, but straight from the heart.

–Albert Einstein

Acknowledgements

The research presented in this thesis was conducted between January 2008 and April 2011 in the NanoMaterials Group of the Department of Applied Physics of the Aalto University School of Science (Helsinki University of Technology until January 2010).

None of it would had been possible without the guidance of Prof. Esko I. Kauppinen. He provided the ideal thesis environment, motivating the big picture of the research and then making sure the necessary resources, contacts and equipment were in place for successful independent work.

My supervisor Dr. Albert G. Nasibulin was always available for discussions and help whenever the need arose. I am especially indebted to his deep understanding of the reactors, and the chemistry of nanotube synthesis, which was instrumental in guiding the growth mechanism studies.

Without a doubt, this thesis would had been immensely poorer without the expertise, encouragement, and the occasionally well deserved criticism from my mentor and friend Dr. Paola Ayala. Her comments on the draft manuscript were also greatly appreciated.

My many co-authors, particularly within the BNC Tubes project, have contributed significantly to the direction and scientific level of this thesis. My heartfelt thanks go to all of them, but particularly to Dr. Giorgio Lanzani, and Prof. Kari Laasonen, Dr. Raul Arenal and Dr. Annick Loiseau.

Of course, collaboration starts at home, and everyone in the NanoMaterials Group has had their part to play along the way. In particular I wish to acknowledge the close collaboration with Dr. Hua Jiang, Zhen Zhu, Antti Kaskela, Ying Tian, Prasantha Mudimela, and summer students Juha Mali and Patrik Laiho.

I am much oblidged for the insightful and expedient feedback from the pre-examiners of the thesis, Dr. Chris Ewels and Dr. Avetik Harutyunyan.

Financial support from the European Commission, Finnish TEKES and the Aalto University MIDE program CNB-E project was deeply appreciated.

Finally, I wish to express my gratitude and love to my life companion Kukka for the best kind of support a scientist (and a man) can hope for.

Contents

Thesis publications

I. Susi, T., Nasibulin, A.G., Ayala, P., Tian, Y., Zhu, Z., Jiang, H. Roquelet, C., Garrot, D., Lauret, J-S., Kauppinen, E.I, 2009. High quality SWCNT synthesis in the presence of NH_3 using a vertical flow aerosol reactor, *Physica Status Solidi B* 246, 2507–2510, doi: 10.1002/pssb.200982338.

II. Zhu, Z., Jiang, H., Susi, T., Nasibulin, A.G., and Kauppinen, E.I., 2010. The Use of NH_3 to Promote the Production of Large-Diameter Single-Walled Carbon Nanotubes with a Narrow (n,m) Distribution, *Journal of the American Chemical Society* 133, 1224–1227, doi: 10.1021/ja1087634.

III. Susi, T., Zhu, Z., Ruiz-Soria, G., Arenal, R., Ayala, P., Nasibulin, A.G., Lin, H., Jiang, H., Stephan, O., Pichler, T., Loiseau, A., and Kauppinen, E.I., 2010. Nitrogen-doped SWCNT synthesis using ammonia and carbon monoxide, *Physica Status Solidi B* 247, 2726–2729, doi: 10.1002.pssb.20100312.

IV. Susi, T., Kaskela, A., Zhu, Z., Ayala, P., Arenal, R., Tian, Y., Laiho, P., Mali, J., Nasibulin, A.G., Jiang, H., Lanzani, G., Stephan, O., Laasonen, K., Pichler, T., Loiseau, A., Kauppinen, E.I., 2011. Nitrogen-doped Single-Walled Carbon Nanotube Thin Films Exhibiting Anomalous Sheet Resistances, *Chemistry of Materials* 23, 2201–2208, doi: 10.1021/cm200111b.

V. Mudimela, P.R., Nasibulin, A.G., Jiang, H., Susi, T., Chassaing, D., and Kauppinen, E.I., 2009. Incremental Variation in the Number of Carbon Nanotube Walls with Growth Temperature. *The Journal of Physical Chemistry C*, 113, 2212–2218, doi: 10.1021/jp808316p.

VI. Lanzani, G., Susi, T., Ayala, P., Jiang, T., Nasibulin, A.G., Bligaard, T., Laasonen, K., and Kauppinen, E.I., 2010. Mechanism study of floating catalyst CVD synthesis of SWCNTs, *Physica Status Solidi B* 247, 2708–2712, doi: 10.1002/pssb.201000226.

VII. Susi, T., Lanzani, G., Nasibulin, A.G., Ayala, P., Jiang, T., Bligaard, T., Laasonen, K., and Kauppinen, E.I., 2011. Mechanism of the initial stages of nitrogen-doped single-walled carbon nanotube growth, *Physical Chemistry Chemical Physics* (in press), doi: 10.1039/c1cp20454h.

Author's contribution

I. The author is mainly responsible for the work (apart from the STM and TEM measurements) and wrote the manuscript (contribution 70%).

II. The author is responsible for the synthesis of the materials, interpretation of the findings, and for co-writing the manuscript (contribution 30%).

III. The author is mainly responsible for the work (apart from the EELS, ED and Raman measurements), analyzed data, and wrote the manuscript (contribution 70%).

IV. The author is mainly responsible for the work (apart from the TEM, SEM and EELS measurements; and partly for developing the resistor network model) and wrote the manuscript (contribution 60%).

V. The author is responsible for the gas measurements and analysis in the manuscript (contribution 10%).

VI. The author is responsible for the gas measurements and co-wrote the manuscript (contribution 30%).

VII. The author is responsible for the design of the study, the gas measurements and analysis, and wrote the manuscript (contribution 50%).

Other featured publications

I. Kleshch, V.I., Susi, T., Nasibulin, A.G., Obraztsova, E.D., Obraztsov, A.N., and Kauppinen, E.I., 2010. A comparative study of field emission from NanoBuds, nanographite and pure or N-doped single-wall carbon nanotubes, *Phys. Status Solidi B* 247, 3051–3054, doi: 10.1002/pssb.201000212.

II. Susi, T., Zhu, Z., Tian, Y., Jiang, H., Nasibulin, A.G., and Kauppinen, E.I., 2011. TEM verification of optical diameter distribution analysis for nitrogen-doped SWCNT films, *To be published in the Journal of Nanoelectronics and Optoelectronics.*

III. Laiho, P., Susi, T., Kaskela, A., Nasibulin, A.G., Kauppinen, E.I., 2011. Optoelectronic performance of nitrogen-doped SWCNT films, *To be published in the Journal of Nanoelectronics and Optoelectronics.*

Symbols and abbreviations

1D	one-dimensional
2D	two-dimensional
BZ	Brillouin zone
CNT	carbon nanotube
CNTN	carbon nanotube network
CO	carbon monoxide
CO_2	carbon dioxide
CVD	chemical vapor deposition
DOS	density of (electronic) states
EELS	electron energy loss spectroscopy
EC	electrostatic collector
ESP	electrostatic precipitator
eV	electron volt
FC	ferrocene
FTIR	Fourier transform infrared spectroscopy
H_2O	water
HWG	hot wire generator
IR	infrared
keV	kiloelectron volt
LDOS	local density of (electronic) states
meV	millielectron volt
MFC	mass flow controller
MWCNT	multiwalled carbon nanotube
N-CNT	nitrogen-doped carbon nanotube
N-graphene	nitrogen-doped graphene
N-MWCNT	nitrogen-doped multiwalled carbon nanotube
N-SWCNT	nitrogen-doped single-walled carbon nanotube
NH_3	ammonia
nm	nanometer
OAS	optical absorption spectra (spectrum)
RBM	radial breathing mode
RGA	residual gas analysis
SEM	scanning electron microscopy
SWCNT	single-walled carbon nanotube
TCE	transparent conducting electrode
TEM	transmission electron microscopy
vHs	van Hove singularity
XPS	X-ray photoelectron spectroscopy
μm	micrometer

1. Introduction

The aim of this thesis was the development of a technique for synthesizing nitrogen-doped single-walled carbon nanotubes to be deposited directly as thin films on various substrates using a novel combination of precursors, carbon monoxide and ammonia. The applicability of the produced material for use as transparent conducting electrodes was studied in depth. Furthermore, the basic chemistry of the precursor reactions on iron nanoparticles was studied by infrared and mass spectrometry and computational methods to gain a better understanding of the growth mechanism.

1.1. Carbon nanotubes

Carbon nanotubes, or helical microtubules of graphitic carbon as they were originally called after their identification in 1991 [1], remain one of the most significant materials in the still emerging field of nanotechnology. Although their younger sibling graphene – a flat monolayer of carbon atoms in a two-dimensional (2D) honeycomb lattice – claimed the 2010 Nobel Prize in Physics, that achievement would not have been possible without intense preceding research into carbon nanotubes (CNTs), and also fullerenes. Nanotubes and graphene are both allotropes of carbon with the same kind of bonding between the carbon atoms.

A free carbon atom has the electronic structure $1s^2 2s^2 2p^2$. In graphene, carbon forms a hexagonal lattice where every atom has three neighbors. This is because the 2s orbital and the $2p_x$ and $2p_y$ orbitals form three hybridized sp^2 orbitals in the graphene plane, at 120° angles to each other. These orbitals form strong σ bonds with the sp^2 orbitals of neighboring carbon atoms. The remaining $2p_z$ orbital is perpendicular to the surface, forming metallic π bonds with the $2p_z$ orbitals of neighbouring carbon atoms. These π bonds are delocalized due to resonance stability, as in benzene. See Figure 1.1 for an illustrations of the sp^2 hybridization and bonding. Graphite consists of a number of these graphene planes stacked on top of each other. Interaction between different layers is of van der Waals type, and very weak compared to the covalent carbon–carbon bonds.

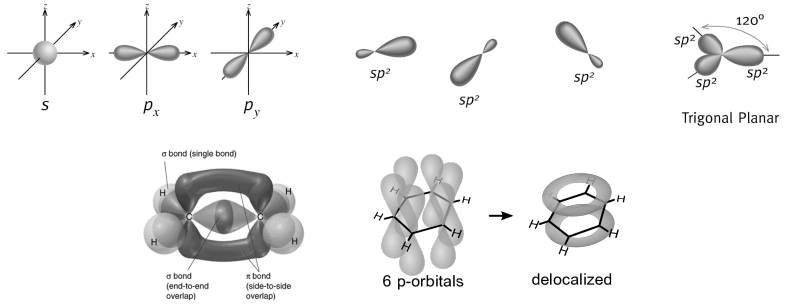

Figure 1.1 (Top) sp² hybridization of the electron orbitals in carbon. (Bottom) The formation of the σ and π bonds from the sp² orbitals, illustrated for the case of ethene; and the formation of the delocalized π orbital, illustrated for benzene. Adapted with permission from [2], Copyright 2011 by the University of Waterloo; and from [3] under the CC BY–SA 3.0 license.

The structure of carbon nanotubes, which consist of carbon atoms in the same kind of sp² honeycomb lattice, is specified by a vector (Figure 1.2)

$$\mathbf{C}_h = n\mathbf{a}_1 + m\mathbf{a}_2 \,, \tag{1.1}$$

where $\mathbf{a}_1$ and $\mathbf{a}_2$ are the unit cell base vectors of the graphene sheet, which joins two equivalent points in the graphene lattice. By folding a graphene sheet into a cylinder, so that the beginning and end of an (n,m) lattice vector join together, one obtains the structure of a certain nanotube. If the structure comprises only of this one wall, such a tube is called single-walled (SWCNT) [4, 5]. The structure can also consist of several concentric SWCNTs of different radii, which together make up a multiwalled carbon nanotube (MWCNT). The interlayer distance is typically very close to the lattice spacing in graphite at approximately 3.4 Å.

If n is equal to m, the resulting (n,n) tubes are dubbed ‘armchair’ due to the pattern the carbon atoms form in the direction perpendicular to the tube axis. Correspondingly, (n,0) tubes are called ‘zigzag’ nanotubes. Other kinds of tubes are all called ‘chiral’, with rows of hexagons spiraling along the nanotube axis. The smallest freestanding single-walled tubes have diameters of about 4.3 Å [6] (see also [7]), while the largest can have diameters of several nanometers (nm). Nanotubes have enormously high aspect ratios, with maximum lengths up to hundreds of micrometers or even centimeters [8]. The SWCNTs have a tendency to form bundles or ‘ropes’ due to the van der Waals interactions between adjacent nanotubes.

SWCNTs differ from MWCNTs in that all of their atoms form a single covalently bound network, composed only surface atoms. These factors give SWNTs more distinctive and varied electronic and optical properties, but also make them more sensitive to any defects in the structure.

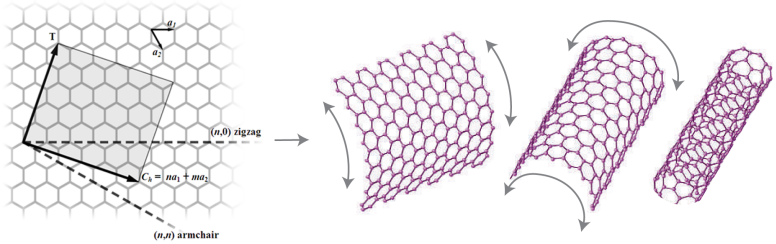

Figure 1.2 The chiral indices and an illustration on how the nanotube structure can be rolled from a graphene sheet. From Wikipedia; and adapted with permission from Macmillan Publishers Ltd: Nature Materials [9], Copyright 2007.

1.1.1. Electronic properties

The electronic properties of SWCNTs depend sensitively on the (*n*,*m*) indices, and therefore on their diameter and chirality. A SWCNT can be a metal, or a semiconductor with either a very small or a moderate band gap.

For a graphene sheet, the conduction and valence bands touch each other at the six corner points of the first Brillouin zone (BZ). A graphene sheet is accordingly semimetallic with zero band gap. Using a simple tight binding model with a nearest neighbor interaction, Wallace [10] determined the energy E_{2D} of an electron at a point defined by wavevectors k_x, k_y to be

$$E_{2D}(k_x k_y) = \pm\gamma_0 \left[1 + 4\cos(\frac{\sqrt{3}k_x a}{2})\cos(\frac{k_y a}{2}) + 4\cos^2(\frac{k_y a}{2})\right], \qquad (1.2)$$

where γ_0 is the nearest-neighbor transfer integral and a = 0.246 nm is the in-plane lattice constant.

Since the graphene unit cell has two atoms, there are four valence bands, three σ and one π. The bonding and antibonding π bands touch at the corners of the hexagonal 2D BZ (Figure 1.3). Since the energy as a function of the wavevector k (Equation 1.2) is linear for low energies near the six corners of the hexagonal 2D BZ, the electrons and holes have zero effective mass and behave like relativistic Dirac fermions. [11]

The situation is markedly different for carbon nanotubes because of their geometry, which confines the electronic states along the circumference, but extends along the tube axis as quasi–1–dimensional (1D). The electronic states of an infinitely long nanotube are thus parallel lines in reciprocal k space, continuous along the tube axis but quantized along the circumference (Figure 1.4). For armchair tubes, there are always states crossing the corner points of the first BZ, making such tubes metallic (Figure 1.4a).

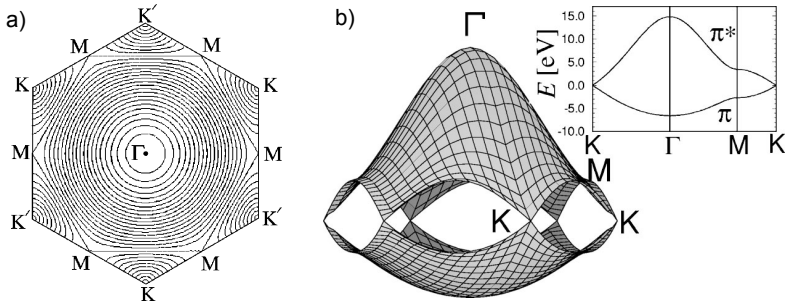

Figure 1.3 a) A 2D reciprocal space energy contour plot for graphene. The equienergy contours are circles near the K points and near the center of the Brillouin zone, but near the zone boundary they are straight lines that connect the nearest M points. b) The energy dispersion relations for the π and π* bands in 2D graphene shown throughout the Brillouin zone. The inset shows the energy dispersion along the high symmetry directions of the 2D BZ. Adapted with permission from [12], Copyright 2000 by The American Physical Society.

For (n,m) tubes with $n - m \neq 3 \times$ integer, there are no electronic states at the corner points at the Fermi level. This makes such tubes semiconducting (Figure 1.4b), with band gaps that scale inversely with the tube diameter. For tubes with $n - m = 3 \times$ integer, there are states at the corners of the first BZ. However, in contrast to armchair tubes, these tubes are metallic at room temperature, but exhibit a very small chirality-dependent gap at lower temperatures due to curvature-induced orbital rehybridization [13]. Furthermore, since the electronic structure is quasi-1D, the SWCNT density of states shows characteristic van Hove singularities (vHs) (Figure 1.5), which has major implications for its properties.

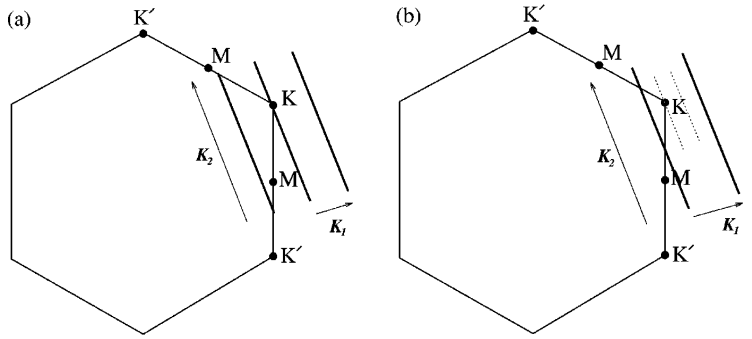

Figure 1.4 The wave vector k is shown in the 2D Brillouin zone of graphene as bold lines for a) metallic and b) semiconducting nanotubes. a) For metallic nanotubes, the bold line intersects a K point at the Fermi energy. b) For the semiconducting nanotubes, the K point always appears one-third of the distance between two bold lines. Adapted with permission from [12], Copyright 2000 by The American Physical Society.

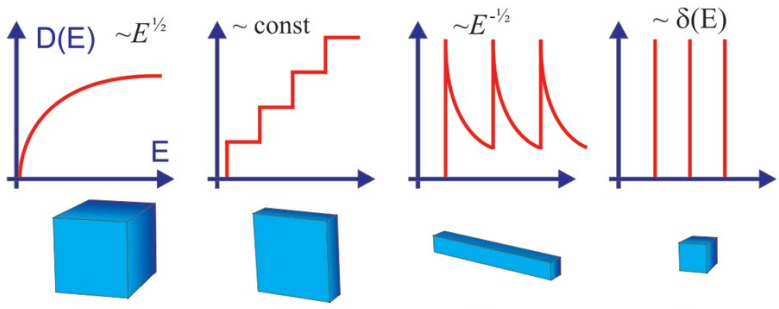

Figure 1.5 The density of electronic states (DOS) describes the number of states per interval of energy that are available to be occupied. The DOS depends on the dimensionality of the system as illustrated above. The (quasi) 1D case exhibits the characteristic van Hove singularities. Adapted from [14].

1.1.2. Optical properties

The optical properties of carbon materials vary greatly. Carbon in a perfect sp^3 diamond lattice absorbs only IR light, leaving diamonds transparent to visible light. Graphene, on the other hand, has a characteristic flat absorbance of $\pi\alpha \approx 2.3\%$, where α is the fine structure constant, due to the Dirac fermion character of the electrons [15].

The optical response of SWCNTs is more interesting, since their optical absorption spectra (OAS) contain peaks which correspond to dipole-allowed transitions between the *i*-th conduction band and *i*-th valence band van Hove singularities, denoted E_{ii}. Figure 1.6 shows the density of states (DOS) of a metallic and a semiconducting SWCNT. Transitions between *i*-th and and *j*-th bands, where $i \neq j$, are not optically active. Thus the optical response is also directly related to the band gap of semiconducting tubes.

Due to the quasi-1D nature of SWCNTs, excitonic effects play a large role [16]. An exciton is a bound state of a photo-excited electron and a hole. Since there is such poor screening in 1D, the Coulomb binding energies in semiconducting SWCNTs can be as large as 1 electron volt (eV), contrasted to ~10 meV in common semiconductors. Therefore these effects can be observed even at room temperature and are essential in explaining the optical response of SWCNTs. Higher order transitions E_{33} and E_{44} are also possible and contain interesting physics [17], but for practical purposes are less important.

Raman spectroscopy has proven to be an even more powerful technique for studying SWCNTs [18]. Raman is used to study vibrational, rotational, and other low-frequency modes in a material. It relies on inelastic scattering of monochromatic laser light. Photons in the laser light interact with molecular vibrations, phonons (quantized lattice vibrations) or other excitations in the system, resulting in the energy of the scattered photons

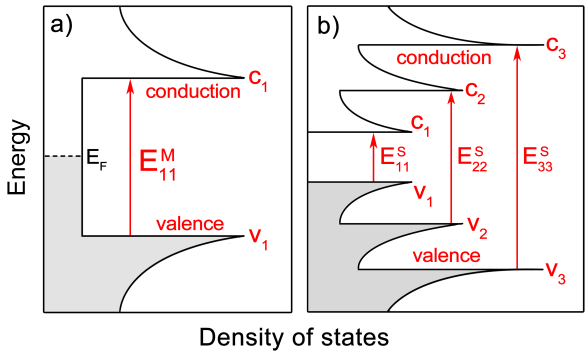

Figure 1.6 A schematic of the density of states (filled in gray, empty in white) for a) a metallic (M) SWCNT, where E_{11}^M denotes the first optical excitation for a metallic nanotube, E_F the Fermi level, and c_1 and v_1 the first vHs in the conduction and valence bands, respectively; b) for a semiconducting (S) SWCNT, where the first optical transition E_{11}^S is across the band gap.

being shifted up or down. The shift in energy gives information about the phonon modes in the system. Especially for bulk nanotube samples, Raman measurement is easy, since spectra can be recorded at ambient conditions with a quick, non-destructive and simple measurement.

A photo-excited electron will experience some processes before recombining with a hole in the valence band. One possible process is scattering from a phonon with a wave vector q. Thus the electronic wave vector is scattered to $k - q$ (phonon emission) or $k + q$ (absorption), and the electron energy is shifted by $\pm\hbar\omega_q$. A one-phonon scattering process is called a first-order Raman process. If the process explicitly involved only phonons, it would be independent of the electronic structure of the material and thus the laser energy E_{laser} used. However, when E_{laser} matches the energy between optically allowed transitions in the material, the scattering efficiency becomes larger. This is called the resonance Raman scattering effect [19]. Thus if either the initial k or the scattered $k \pm q$ states are real electronic states, the scattering amplitude is resonantly enhanced.

The resonance intensity depends on the joint density of electronic states in the conduction and valence bands separated by the photon energy. So although other carbon materials have similar phonons as SWCNTs, the optical response of SWCNTs is greatly enhanced due to the large DOS at the van Hove singularities. If both states in the resonance are real, this is called a double-resonance process. This resonance enhancement is understood by quantum perturbation theory, where the energy difference denominator for the scattering amplitude becomes zero.

A characteristic feature of the Raman spectra of SWCNTs is the radial breathing mode (RBM), where all atoms vibrate in phase in the radial direction (Figure 1.7). The frequency of the RBM depends inversely on the

tube diameter, and due to the resonance effect, only appears strong in the spectra when the laser energy is in resonance. This is a first order process, as is the G mode (around 1600 cm^{-1}), where two atoms in the unit cell are vibrating tangentially one against the other (Figure 1.7). The G mode in nanotubes contains multiple peaks because of the symmetry breaking of the tangential vibration in the cylindrical geometry and the quantum confinement of the phonon wave vector along the nanotube circumference. The lower energy peak (G^-) of metallic nanotubes exhibits a broadening of the Breit–Wigner–Fano lineshape, accounting for a coupling of the circumferential phonon with a continuum of conducting electrons [20].

In a second-order Raman processes, two phonons with the same or different frequencies are emitted, or there is one phonon scattering and one elastic scattering caused by the presence of a defect in the lattice. The two regions of Raman spectra related to second-order processes are the D mode (around 1200 cm^{-1}), arising from the elastic scattering off a defect, and the G' (alternatively called 2D, around 2600 cm^{-1}) mode, which is a two-phonon process requiring no defect to be activated. Both are doubly resonant. The D band intensity is related to the amount of disorder in the sample [21]. Thus the intensity ratio of the D to the G band has been widely used [22-25] as a rough measure of the quality of the produced nanotubes, though resonance [26] and charge transfer effects [27] complicate any simplistic analysis.

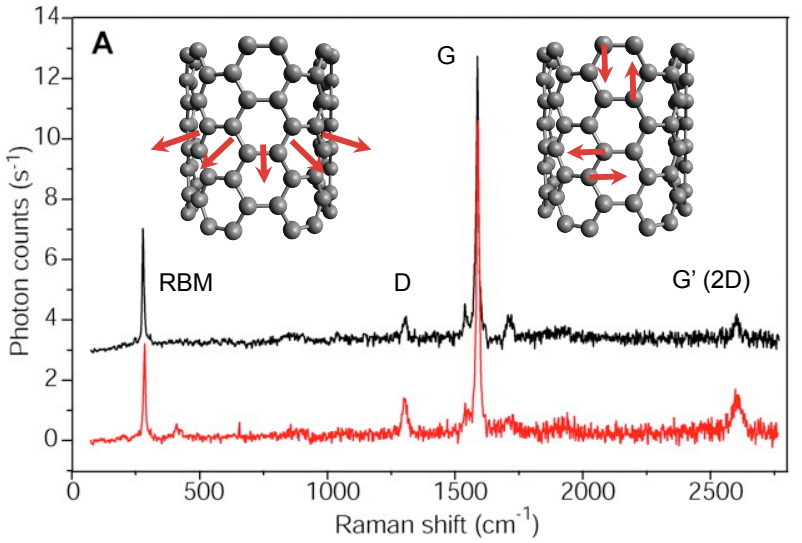

Figure 1.7 Identical resonance Raman spectra for two different individual (7,5) SWCNTs. The RBM, D, G and G' peaks are indicated, along with atomic displacements associated with the RBM and G-band normal-mode vibrations. Adapted with permission from [28], Copyright © 2003, American Association for the Advancement of Science.

1.1.3. Synthesis

Synthesis of novel materials is a staple of materials science research, and arguably even more so in the case of nanomaterials. Carbon nanotube synthesis has long been an intensive research topic, rendered slightly less so only lately due to increasing mastery over mass production techniques.

Synthesis of carbon nanotubes was originally achieved with so-called physical methods, referring to the mechanism used for obtaining free atomic carbon for the self-assembly of the graphitic network. In physical methods, atomic carbon is liberated by introducing large amounts of energy into a solid target, typically graphite. This can be achieved by either an electric arc (dubbed arc discharge [1, 29]) or by a high-power laser (dubbed laser ablation [30]). Multiwalled carbon nanotubes can be obtained without catalyst, while for making single-walled, the presence of metallic catalyst (typically Fe, Co, Ni, Y or Mo) in the target is required.

Most synthesis methods in widespread use rely on catalytic chemical reactions for the decomposition of carbon-containing precursors, and thus fall within the category of chemical vapor deposition (CVD). This is much more amenable to scale-up [31], and indeed almost all commercial production of CNTs today relies on some form of CVD. Furthermore, since the temperature required for the catalytic reaction is lower than in the physical methods, better control over the growth process is possible. MWCNTs produced by CVD are typically of lower structural quality than those produced by physical methods, but this does not seem to be the case for SWCNTs, where high structural perfection can be achieved [32].

Most CVD methods use hydrocarbons as the carbon source for CNT synthesis. Hydrocarbons, for example methane, acetylene, or octane, with n carbon and m hydrogen atoms, decompose with the overall reaction

$$\mathrm{C}_n\mathrm{H}_m \rightleftharpoons n\mathrm{C} + \frac{m}{2}\mathrm{H}_2 \,. \tag{1.3}$$

Hydrogen is also used as an additional process gas, often to reduce the catalysts. Hydrocarbons decompose easily on many surfaces heated to temperatures of 600–700 °C that are typically required for nanotube growth. This self-decomposition may lead to the formation of graphitic deposits or amorphous carbon on the nanotubes [33], which needs to be removed in subsequent processing steps.

By contrast, carbon monoxide (CO) is an alternative source of carbon for nanotube synthesis [33-35]. Carbon monoxide disproportionates by the Boudouard reaction

$$\mathrm{CO} + \mathrm{CO} \rightleftharpoons \mathrm{C} + \mathrm{CO}_2 \,. \tag{1.4}$$

CO disproportionation has a suitable temperature range for SWCNT production, it requires catalyst material for the reaction to occur so precursor self-decomposition is not an issue, and the reaction rates are small enough so that the number of walls that can grow is small. As can be seen from the balance of the reaction, the addition of CO_2 can be used to control the reaction.

Important in the context of this thesis, Nasibulin and coworkers have shown that CO_2 and H_2O play important roles in the synthesis of SWCNTs with CO [36] in a floating catalyst environment. At the high temperatures required for CO disproportionation, CO_2 and H_2O can serve to etch amorphous carbon precipitated on the surface of the CNTs and catalyst particles, resulting in CNT 'cleaning' and increasing the lifetime of the catalysts. Cleaning occurs because amorphous carbon deposits are less strongly bound than carbon atoms in the nanotube sp^2 network, so the reverse reactions will predominantly etch these away.

If carbon precursor decomposition and the growth of CNTs occur on catalyst particles embedded in a surface, the process is called surface supported or substrate CVD [34]. The best catalysts are transition metals (Fe, Ni, Co, but also bimetallic compounds such as CoMo), although recently synthesis has been reported possible also on noble metals [37] or even SiO_2 [38, 39]. The process can take place either in high pressure, atmospheric pressure, or in a partial vacuum. The chemical reaction rates of the precursors can be enhanced by the use of plasma, enabling deposition at lower temperatures. In aerosol–assisted CVD, precursors are transported into a heated furnace by means of a liquid/gas aerosol, and growth happens on catalyst particles deposited on a substrate, or carried into the reactor walls. If the whole process takes place in the gas phase, this is called floating catalyst (or aerosol-unsupported) CVD [40].

Despite the many successes of CVD in CNT production, many open questions and challenges remain, particularly in controlling the chirality of as-grown CNTs. For nitrogen-doped SWCNTs, reliable synthesis remains an issue to this day.

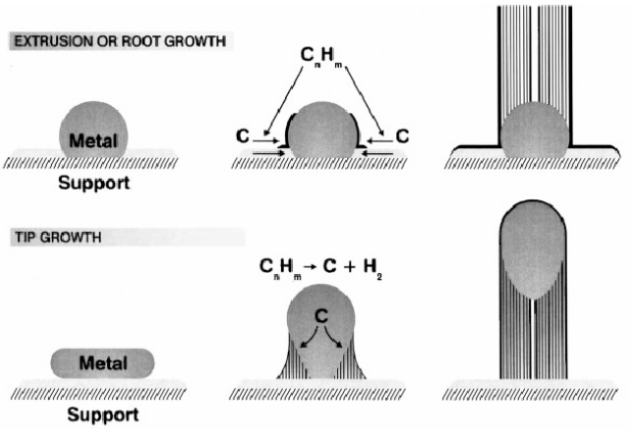

Figure 1.8 Visualization of possible MWCNT growth mechanisms. Reproduced with permission from [41].

1.1.4. Growth mechanism

In supported CVD, there is a broad consensus on the growth mechanism of MWCNTs. First, the catalyst particles are formed (and often reduced), and the process temperature raised to the desired level. To initiate the growth of nanotubes, two gases are fed into the reactor: a process gas (such as nitrogen, hydrogen, ammonia, etc.) and a carbon-containing gas (such as acetylene, methane, carbon monoxide, ethanol, etc.) Nanotubes grow at the sites of the metal catalyst; the carbon-containing gas is broken apart at the surface of the catalyst particle, and carbon is transported to the edges of the particle where it starts forming the tube. For supported metals, filaments can form either by 'extrusion' (base growth), in which the nanotube grows upwards from the metal particles that remain attached to the substrate, or the particles can detach and move at the head of the growing nanotube, which is called 'tip-growth'. See Figure 1.8 for a visualization of the two mechanisms. The mechanism at any particular synthesis conditions depends on the adhesion between the catalyst particle and the substrate.

For SWCNT growth, the vapor–liquid–solid model [42] has been the most popular mechanism proposed (Figure 1.9). In this model, carbon atoms liberated from the precursor molecules by reactions catalyzed by the metal particle dissolve into the particle itself. This results in a supersaturation of the metal particle with carbon due to the continuous reactions. The excess carbon then precipitates onto the surface of the particle, initiating the formation of an sp^2 carbon cap nucleus on the metal surface. If the temperature is sufficiently – but not excessively – high, the cap can lift off the surface and form the beginning of a SWCNT. It then grows by continuous addition of carbon atoms at the open edge attached to the metal nanoparticle.

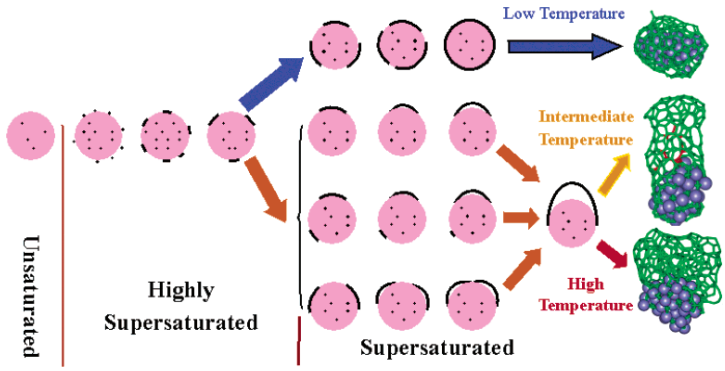

Figure 1.9 Vapor–liquid–solid model of SWCNT growth at different temperatures. Reproduced with permission from [43], Copyright © 2004, American Chemical Society.

The VLS mechanism assumes that carbon diffuses through a liquid metal particle, driven by either a temperature or a concentration gradient. For very small catalyst particles, even though no temperature gradient likely exists [44], a carbon concentration gradient could provide a sufficient driving force for diffusion. Depending on temperature, there can be too slow or too fast carbon diffusion, neither of which will lead to CNT production. However, the validity of the VLS model has been recently called into question by Raty et al. [45]. By modeling CVD growth of SWCNTs on Fe nanoparticles using *ab initio* molecular dynamics, they found that carbon atoms do not dissolve into a 1 nm Fe particle, but instead diffuse only on the surface (Figure 1.10). In this mechanism as well, the carbon atoms form an sp^2 network and a nanotube cap. This viewpoint is also supported by recent SWCNT production from noble metals including Au and Ag [37], which is difficult to explain in terms of classic VLS theory, since these metals have very limited ability to dissolve C. Thus the growth mechanism of even normal, undoped SWCNTs remains controversial.

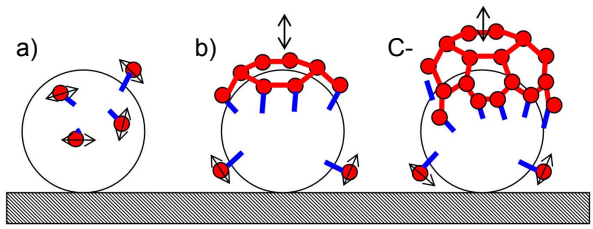

Figure 1.10 Schematic representation of the basic steps of SWCNT growth on a Fe catalyst. a) Diffusion of single C atoms (red spheres) on the surface of the catalyst. b) Formation of an sp^2 graphene sheet floating on the catalyst surface with edge atoms covalently bonded to the metal. c) Root incorporation of diffusing single C atoms (or dimers). Reproduced with permission from [45]. Copyright 2005 by The American Physical Society.

1.2. Nitrogen-doped nanotubes

To harness the full potential of carbon nanotubes for applications, the electronic properties of an ensemble of CNTs must be controlled. Much effort has been directed to affect the chirality of produced nanotubes during synthesis, to some extent successfully [46-52]. Another possible way to control the electronic properties of nanotubes is by substitutional doping with foreign chemical elements. The two practical candidates are the nearest neighbors to carbon in the periodic table, boron and nitrogen. Nitrogen in particular has attracted much attention [53-58] due to its suitable atomic size and additional electron compared to carbon. Along with nitrogen-doped carbon nanotubes (N-CNTs), N-doped graphene (e.g. [59, 60]) and graphene nanoribbons [61] have also been recently studied.

The electrical doping of semiconducting SWCNTs by charge transfer from the nitrogen dopant atoms mentioned above is one of the most commonly envisioned motivations for doping CNTs with nitrogen. For this, it would be vital that the charge transfer is of a uniform electrical nature, e.g. n-type, and sufficiently large for a significant effect to be achieved. Another significant motivation is the introduction of reactive sites on the otherwise inert walls of CNTs. This is expected for example to enhance their bonding in composites, and to enhance their reactivity with adsorbed molecules for e.g. sensor applications. Additional details can be found in [62, 63].

Substitutional doping is distinct from other methods of donating charge to the nanotubes, such as from adsorbed species (chemical doping) or electrochemical charging. Doping during synthesis is also distinct from post-synthesis techniques for introducing heteroatoms into the lattice such as thermochemical substitution reactions [64, 65] (see also [56]) and ion implantation [66, 67].

1.2.1. Local configuration of nitrogen dopants

Since nitrogen has one extra electron compared to carbon, introducing nitrogen heteroatoms into the nanotube lattice could be expected to contribute to n-type doping of the host. Indeed, many theoretical works have shown that a direct substitution of a carbon atom by nitrogen, the so-called graphitic substitution (also called quaternary nitrogen, Figure 1.11a), will result in localized states above the Fermi level [55, 68, 69] (Figure 1.12), with practically no geometric changes in the lattice [58, 69]. This is because the N atom uses three electrons in σ bonds and one in π, like carbon, but the remaining fifth valence electron is forced to occupy the π* donor state. Substitutions on neighboring carbon atoms are highly unfavorable [70, 71], although next nearest neighbors are a possibility [71, 72], and have even been recently proposed to explain STM measurements of N-graphene [73].

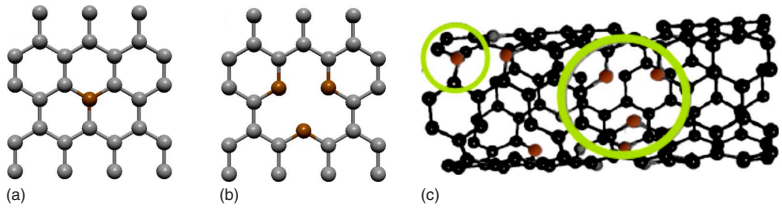

Figure 1.11 Possible configurations for N are (a) direct substitution or (b) a triple N pyridinic site in the (c) SWCNT wall. Reprinted with permission from [56], copyright 2010 by The American Physical Society.

Since the atomic size of nitrogen is slightly smaller (atomic radius 71 pm [74]) than carbon (76 pm), N can also create a defect in the lattice. The most accepted such configuration is the so-called triple N pyridinic–vacancy (3NV) configuration, where 3 N atoms form sp^2 bonds to two carbon atoms each around a single carbon vacancy [75, 76] (Figure 1.11b). This is energetically favorable since it presents no dangling bonds. This type of site is not necessarily n-type, but it can also be p-type [68, 75] depending on the geometry, due to the missing p_z orbital of the vacancy. Therefore the actual effect nitrogen doping has the electronic structure of SWCNTs depends on the relative amounts of the different dopant configurations in the nanotube walls [77]. It should be noted no compelling local measurements have identified this configuration in nitrogen-doped single-walled carbon nanotubes (N-SWCNTs) [56].

On the contrary, scanning tunneling microscopy (STM) measurements have shown extended perturbations of the SWCNT electronic structure [78], which do not seem to correspond to either a substitution or a 3NV pyridinic configuration [68]. To complicate matters further, at least in small diameter nanotubes, the formation energy of a four N pyridinic–divacancy (4ND) configuration was calculated to have the lowest formation energy [71]. However, partly motivated by kinetic considerations (the feasibility of introducing 3, let alone 4 N atoms at the same time to the growing edge of a nanotube), unsaturated pyridinic sites (one or two N atoms around a single vacancy) have also been proposed [70, 79]. Pyrrolic nitrogen (nitrogen in a 5-membered carbon ring) has been suggested to be responsible for the characteristic bamboo-shape of nitrogen-doped multiwalled carbon nanotubes (N-MWCNTs) [80], and is believed to be present in N-graphene (e.g. [81]). It is not clear if it has a role in N-SWCNTs.

What does seems clear, however, is that even though X-ray photoelectron spectroscopy demonstrates the presence of several nitrogen binding energies (e.g. [82, 83]), further studies with locally resolved techniques such as STM/STS or state-of-the-art atomic resolution electron microscopy [84] are needed for conclusive identifications to be made of the nitrogen dopant configurations in SWCNTs.

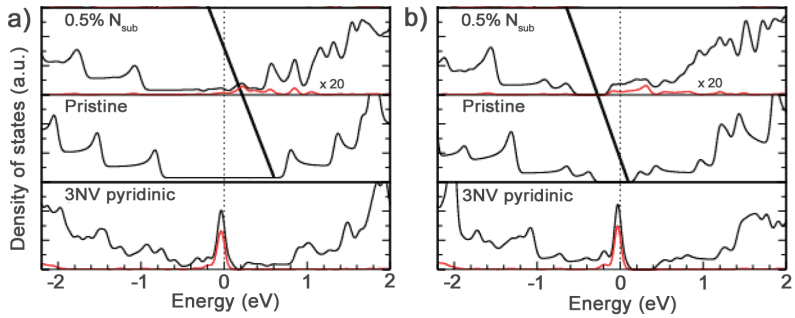

Figure 1.12 DOS (black line total, red on N atom) of pristine, N-substituted, and pyridinic-doped a) metallic (10,10) and b) semiconducting (17,0) SWCNT. Adapted from [68], Copyright © 2010, American Chemical Society.

1.2.2. Modification of nanotube properties

In normal pristine SWCNTs, conduction occurs via the delocalized π–electron system. At room temperature, both metallic and semiconducting SWCNTs are ballistic conductors along the tube axis. As stated above, nitrogen heteroatoms can cause either n- or p-type doping of the electronic structure of SWCNTs, depending on the bonding configuration of nitrogen in the wall. However, even if predominantly one type of doping was achieved and the Fermi level significantly shifted, a decrease in conductance could still result from increased electron backscattering from the dopant states. This applies even if the sites are substitutional [55], but especially if they are pyridinic, since those likely have a permanent electric dipole moment [77].

A single site only induces a dip in the conductance at the resonant energy (Figure 1.13a). For a realistic random distribution of such sites, the effect on transport is severe (Figure 1.13b). Latil and coworkers have theoretically shown that the mean free path decreases linearly with substitutional dopant concentration at low (<0.5%) doping levels [85]. Only few studies have tried to experimentally address the issue of the conductivity of N-SWCNTs [77, 86, 87], but the results thus far are neither conclusive nor comprehensive, and clearly more work is needed on a single tube transport level.

As for the optical properties of N-SWCNTs, little is known due to a lack of samples until recently [56]. Gerber et al. [72] predicted theoretically that nitrogen substitution at a 1.6% level (1 N in a 64 atom unit cell) would increase the E_{11} transition energy by 0.05 eV, while decreasing the E_{22} energy by 0.09 eV. They also found that doping would induce a downshift of the Raman RBM frequency in the order 5 cm^{-1} at a 3.1% doping level. However, we note that the nanotube they considered had a very small

diameter (<0.7 nm), and both these effects would be much weaker – and experimentally very likely undetectable – in real larger-diameter tubes, particularly in a bulk measurement. Indeed, e.g. Villalpando-Paez et al. [86] have noted no changes in the RBM frequencies in their samples.

On the other hand, it has been consistently observed [88-90] that there is an increase in the Raman D to G intensity ratio, attributed to increased disorder in the walls caused by the nitrogen dopants. At the same time, a decrease in the diameters of the produced N-SWCNTs with increasing N precursor amount has been seen, though the mechanism for this finding is unclear. A softening (downshift) of the G band phonon has been reported for N-MWCNTs [91, 92], but not for N-SWCNTs [82, 88-90, 93]. Interestingly, it has been proposed [94] that the G' (2D) band would be sensitive to charged dopants, leading to a hardening of the K point phonon and a change in the G' lineshape and position, though further work is needed to corroborate this effect.

Nitrogen doping has a detrimental effect on the mechanical strength of CNTs [95] since C–N bonds are weaker than C–C bonds. N-CNTs also oxidize at lower temperatures [96]. Furthermore, N-SWCNTs are less stable under the electron beam in TEM [97], likely due to lower knock-on thresholds for certain atoms at the dopant sites. Early theoretical studies attributed the damage mechanism to the displacement of the nitrogen atoms [98], but later developments have proven the tight-binding methodology used there to be insufficient for describing the mechanism correctly in BN [99], and most likely in N-SWCNTs as well. Further studies on the topic are needed to address this issue.

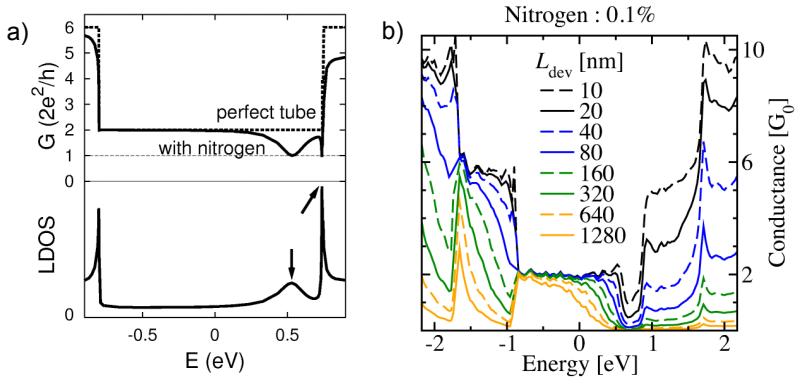

Figure 1.13 a) Effects of substitutional N on the conductance and LDOS of a (10,10) SWCNT. Adapted with permission from [55], Copyright © 2000 by The American Physical Society. b) Calculated quantum conductance of a (10,10) SWCNT containing 0.1% of randomly placed substitutional N impurities, plotted for different lengths of the device. A decrease of the conductance is observed near at the donor energies and near the vHs. Adapted with permission from [85], Copyright © 2004 by The American Physical Society.

1.2.3. Synthesis

Nitrogen doping of carbon nanotubes was proposed theoretically already in 1993 by Yi and Bernholc [58]. After pioneering work by Stephan et al. on BN co-doping via arc-discharge [53] in 1994, there are a few reports in the literature from 1995–1996 that mention N-CNTs [100-102] as byproducts of other processes. However, the first reliable reports on the CVD synthesis of nitrogen-doped multiwalled carbon nanotubes (N-MWCNTs) are from 1997 by Yudasaka et al. [103] and Sen et al. [104] , and from 1999 by Terrones et al. [105]. Figure 1.14 shows the number of papers published annually on N-CNTs, N-SWCNTs specifically, and N-doped graphene, according to a keyword search in the ISI Web of Knowledge [106]. As can be inferred from the number of publications, since 1999, a variety of methods have been reported for the synthesis of N-MWCNTs. For more information, the reader is referred to several excellent recent reviews [70, 107, 108].

For the N-SWCNT case at hand here, we note that although the literature search with the keywords used [106] shows two papers from 1999 and 2000 by Golberg et al. [64, 65], these were concerned with B– or BN–co-doping via thermochemical substitution reactions, while the paper from 2003 was a theoretical work. Thus the first experimental work on N-SWCNT synthesis was by Glerup et al. in 2004 using arc discharge [97]. Successful synthesis was later achieved also by laser ablation [78, 109]. However, there are only a handful of reports on N-SWCNTs synthesis using chemical vapor

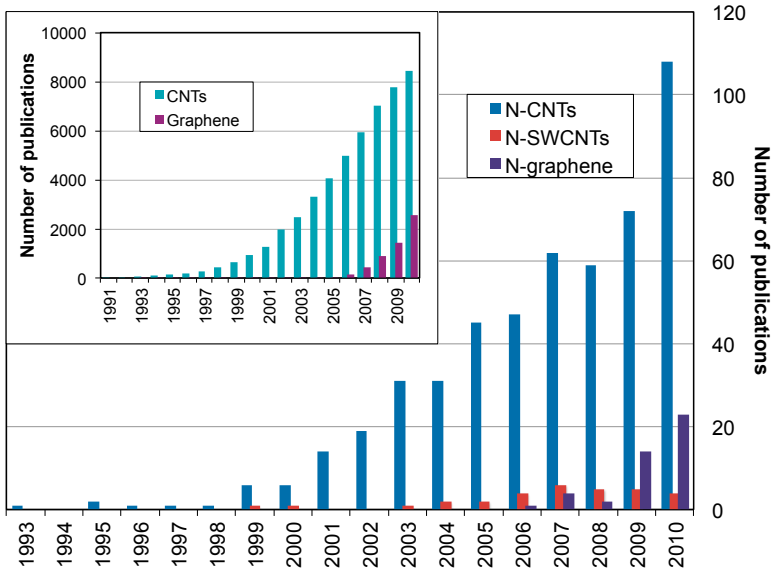

Figure 1.14 Trends in the number of papers on N-doped carbon nanotubes, N-doped single-walled carbon nanotubes, and N-doped graphene published annually from 1993 to 2010. The inset shows the number of papers on carbon nanotubes and graphene for comparison. Data from the ISI Web of Knowledge.

deposition [82, 86, 88, 89, 93, 110], and the number of publications has not increased in the same manner as those for N-CNTs or even N-graphene. Successful nitrogen precursors for CVD synthesis of N-SWCNTs have been benzylamine [82, 86], acetonitrile [89, 93], while pyridine and NH_3 have been used for making N-doped double-walled carbon nanotubes (N-DWCNTs). Ammonia has also been used for N-SWCNT synthesis by plasma-enhanced supported CVD [88]. None of these studies utilized carbon monoxide as the carbon precursor gas, and only the work of Min et al. [88] used separate carbon and nitrogen sources.

1.2.4. Growth mechanism

Despite the great number of works on N-MWCNTs, synthesis of N-SWCNTs has struggled to overcome difficulties foreign to the synthesis of pristine material, which is nowadays produced clean in gram quantities. Efforts to master the synthesis of N-SWCNTs have been hindered by an acute lack of knowledge about the chemistry involved and the growth mechanism [56, 111, 112]. Though admittedly as noted above, despite intensive studies the mechanism of even pristine CNT growth is still controversial.

Although N-MWCNTs have been widely studied, the correlation between their morphology, crystallinity and properties is not completely understood. The base growth mechanism is commonly proposed to be responsible for the characteristic compartmentalized (bamboo-shaped) structure [105, 113]. This model assumes that the catalyst particles dissociate reactant molecules into N and C atoms, whose incorporation into or onto the catalyst nanoparticle results in the walls being pushed away to form a tubular structure. However, no studies have directly addressed the mechanism by which the precursors decompose [111]. The role of nitrogen in N-MWCNTs formation is suggested to be related to the generation of pentagons along with hexagons [80], as it is believed that the presence of N in the carbon deposit causes surface strain, leading to a ‘pulsed’ effect in which the C/N surface atoms detach from the metal particle intermittently, forming the compartmentalized structure observed [114].

To our knowledge, there is only one tentative model proposed for the growth mechanism of N-SWCNT [115], which further does not discuss the very first stages of growth. Addressing the mechanism of chemical reactions that yield atomic carbon and nitrogen on the catalytic particle [116] is a crucial first step towards understanding the CVD synthesis of N-SWCNTs. However, only small precursor molecules can be treated at a high level of accuracy and detail. Unfortunately, as noted by Ewels et al. [111], most N-CNT synthesis methods use complex molecules as their carbon and nitrogen feedstocks. This probably explains why the chemical reactions have not been explicitly addressed until now.

1.3. Nanotube films

Apart from their individual electrical character, the positions, lengths, bundling and orientations of nanotubes in typical samples show considerable variability. This makes reliable and cheap fabrication of devices with reproducible electrical behavior difficult. Therefore random carbon nanotube networks (CNTNs) have attracted considerable interest as the first viable technological avenue for CNT applications. In this context, many promising applications have been demonstrated such as optically transparent and conducting films [117, 118], transparent transistors [119-121], organic light emitting diodes [122] and chemical sensors [123].

In particular, the use of CNTs as transparent conducting electrodes (TCEs) to replace indium tin oxide coatings [124] has attracted much attention as an attractive early application for CNTs, since this requires very little control over the morphology of the film. CNT films have the additional advantages that they can be deposited at ambient temperature and onto polymer substrates, that they can possess a wide range of conductivities and optical transparencies simply depending on their thickness [125], and that they are very flexible. Single-walled CNTs are preferable due to their ballistic conductance and small optical cross section. However, for TCE applications, semiconducting SWCNTs, which constitute 2/3 of typical samples, are not as useful due to their band gap. A widely used technique for enhancing the performance of such mixed films is treating them with an acid, which induces p-type charge transfer via molecular adsorbates (chemical doping) [126]. This can lower the Fermi level by as much as 0.6 eV, which transforms most semiconducting SWCNTs into degenerately doped hole-conducting semiconductors, with properties much like those of one-dimensional metals. Molecular doping by acids also drastically lowers the bundle–bundle transport barriers [127]. The drawback is that since the bonding between most molecular dopants and SWCNTs is weak, desorption and thus stability of the doping is a significant problem.

Therefore it has been expected that nitrogen doping might enhance the optoelectronic performance of nanotube films in an intrinsic and more stable way. Indeed, there are some reports on N-MWCNT films where slight enhancement has been observed [128], attributed to an increased density of states at the Fermi level and an increased number of charge carriers. The case of N-SWCNTs has been much less known until now.

A further promising possible application for N-SWCNTs is in sensors, where it is expected that the nitrogen sites would enhance either selectivity or sensitivity for various gases [71, 129]. Another recently demonstrated application for N-MWCNTs is in electrocatalysis [62, 130], but it is not clear at this stage whether N-SWCNTs would be equally suitable.

2. Methods

The purpose of this section is to provide brief yet adequate descriptions of the various research methods used, with compact background theory and references. The methods described in this chapter were developed previous to the thesis research unless otherwise stated. The aim is to enable a non-specialist reader to understand the main ideas and findings of the thesis. Details can be found in the individual publications and references therein.

2.1. Floating catalyst CVD

The method employed in this thesis for synthesizing N-SWCNTs relies on two previously developed floating catalyst ([131-133]; see also [40]) CVD reactors. These are the so-called ferrocene (FC) reactor [134] and the hot wire generator (HWG) reactor [116]. By 'floating catalyst' we mean that the growth of nanotubes happens on catalyst particles in the gas phase, and the product is collected downstream of the reactor directly from the gas phase [40]. In these reactors, chemical reactions do happen on the reactor walls, but since that material is not collected, it is not discussed in any of the publications. The selectivity for SWCNTs in the collected material is extremely high. Though the method is similar to the well-known HiPco process [33], it is distinct in that these reactors operate at ambient pressure with a laminar gas flow. This helps to grow SWCNTs with larger diameters, smaller bundles and longer lengths, though at lower yield.

In both reactors, carbon monoxide (CO) is the carbon precursor, carbon dioxide (CO_2) is used to control the process and enhance the quality of the product, and ammonia (NH_3) is used as the nitrogen precursor. The role of NH_3 is dual, as it acts as the nitrogen dopant source [135] as well as an etching agent [136], while CO_2 acts only as an etching agent [36, 137]. Each reactor consists of a ceramic reactor tube inserted into a heated furnace. The alumina ceramic tubes used for the experiments contain SiO_2 (0.25%), Ca (0.02%), Fe (0.02%), and Cd (0.09%) as impurities, and have 22 mm internal diameters.

The main difference between the two reactor types is the method of producing the floating catalyst particles. While some of the gas flows are also slightly different, the basic chemistry and mechanisms are very similar.

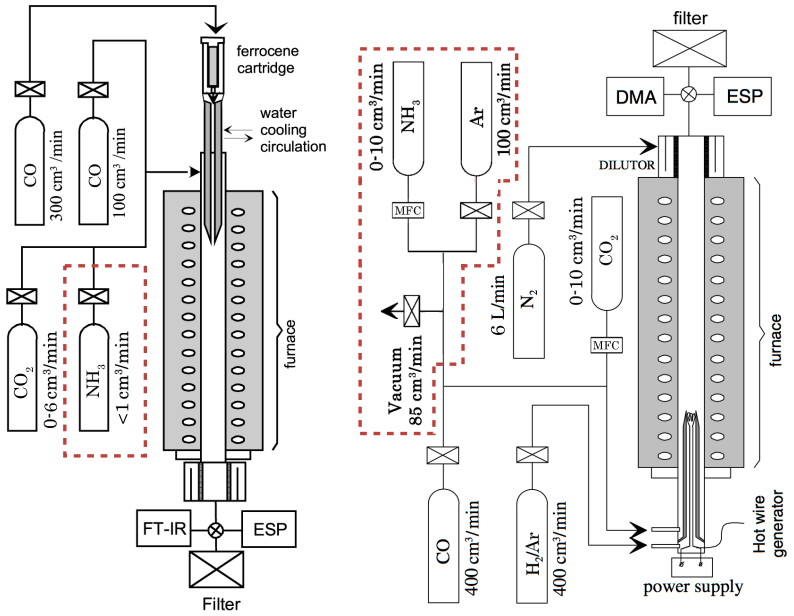

Figure 2.1 Schematic illustrations of the ferrocene reactor (left) and the hot wire generator reactor (right). The modifications made by the author for introducing ammonia (Section 3.1.1) are marked with dotted red lines.

2.1.1. Ferrocene reactor

In the ferrocene reactor (Figure 2.1), iron particles are derived from ferrocene ($FeCp_2$) molecules [134]. These are introduced into the reactor as vapor, with a constant partial pressure of 0.7 Pa. To vaporize the ferrocene, a flow of CO (300 cm^3/min) was continuously directed through a cartridge containing the precursor powder mixed with SiO_2 powder at ambient temperature. A stainless steel water-cooled injector probe, held constantly at 24°C, was used to feed the precursors to the furnace. The location of the injector probe was optimized previously [138], and kept constant in all the experiments described here. The temperature to which the precursor was introduced was determined by the furnace wall temperature. The large temperature gradient at the tip of the cooled probe with respect to the heated furnace causes a rapid decomposition of the ferrocene molecules. An additional CO flow of 100 cm^3/min was introduced outside of the water-cooled probe, along with CO_2 and NH_3 (see Section 3.1.1.1).

Previous work on the ferrocene reactor has established a tentative growth model [40, 134, 138, 139] (Figure 2.2). In the floating catalyst environment, tip and base growth are of course equivalent. Decomposition of $FeCp_2$ vapor results in catalyst particle formation by collision processes, and subsequent decomposition of ferrocene on the catalyst particles and further collisions enlarge their size. Depending on their size, the particles either nucleate the

growth of SWCNTs or become inactive by growing too large. Based on the Kelvin equation, catalyst particles of around 4.5 nm diameters are thought to be solid at synthesis temperatures around 900 °C [138]. Iron on the reactor walls contributes to the formation of CO_2, which plays an important role in CNT growth [36] by etching amorphous carbon from catalyst particle and CNT surfaces, preventing particle deactivation as well as cleaning the tubes and perhaps even healing defects [140, 141].

The nucleation of SWCNTs is thought to occur from a graphitic layer on the surface of a solid iron catalyst particle supersaturated by carbon [40]. Carbon released on the surface forms a graphitic cap, which detaches and the CNT starts to grow by a continuous feeding of carbon into the hexagonal CNT network at the edge attached to the particle. This leads to a carbon concentration gradient in the particle, which provides a continuous flux of carbon atoms through the catalyst particles from the surface to the region of CNT growth. Although as noted in Section 1.1.4, this model should only be taken as working hypothesis. On the basis of the SWCNT length, temperature, and residence time in the reactor, the average growth rate of the SWCNTs was calculated to be around 1 μm/s [138].

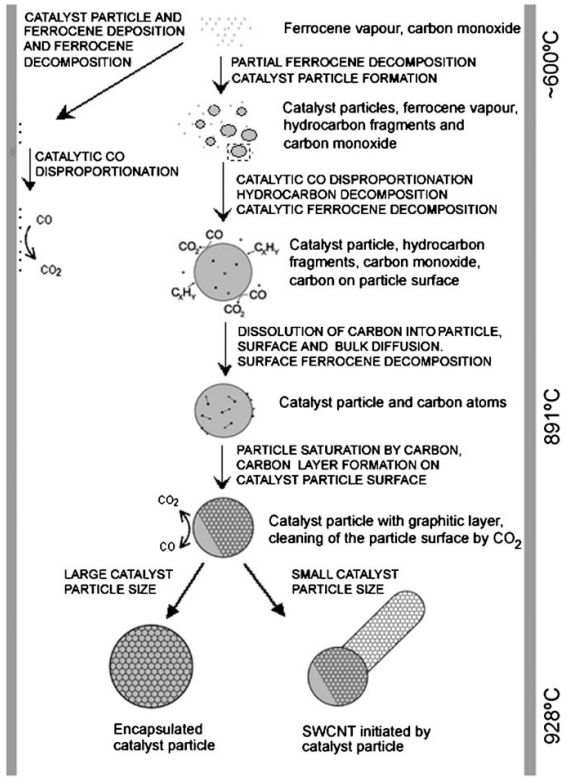

Figure 2.2 Schematic representation of the SWCNT formation mechanism in the ferrocene reactor with CO as the carbon precursor at a temperature of 1000°C. Reproduced with permission from [134], Copyright © 2006, Elsevier.

2.1.2. Hot wire generator reactor

The hot wire generator (HWG) reactor (Figure 2.1) was originally described in [116]. In this method, catalyst particles are grown *in situ* by physical nucleation from iron vapor evaporated from a resistively heated iron wire of 0.25 mm diameter, inserted into an ambient pressure laminar flow reactor in a ceramic inner tube (external diameter 13 mm, internal 9 mm). The wire is protected by a 400 cm^3/min H_2/Ar flow (7/93%). An additional outer flow of 400 cm^3/min CO provides the carbon source, along with CO_2 and NH_3 (see Section 3.1.1.2). The outlet flow is mixed with 3000 cm^3/min N_2 flow using a porous tube dilutor to reduce aerosol losses and cool the gas.

In the case of the HWG, the difference in the process compared to the ferrocene reactor is only in that the catalyst particles are physically nucleated in the reducing H_2/Ar flow before being exposed to the carbon source (Figure 2.3). This means that the chemistry on the forming catalysts is slightly simpler (e.g. no hydrocarbon fragments from the cyclopentadienyl rings in ferrocene), and also that they are slightly smaller. The presence of more H_2 will also increase the CO hydrogenation and water–gas shift reactions [36], though the addition of NH_3 to both reactors will likely render the differences less significant. The HWG reactor is also slightly longer, and the total gas flow larger (Figure 2.3).

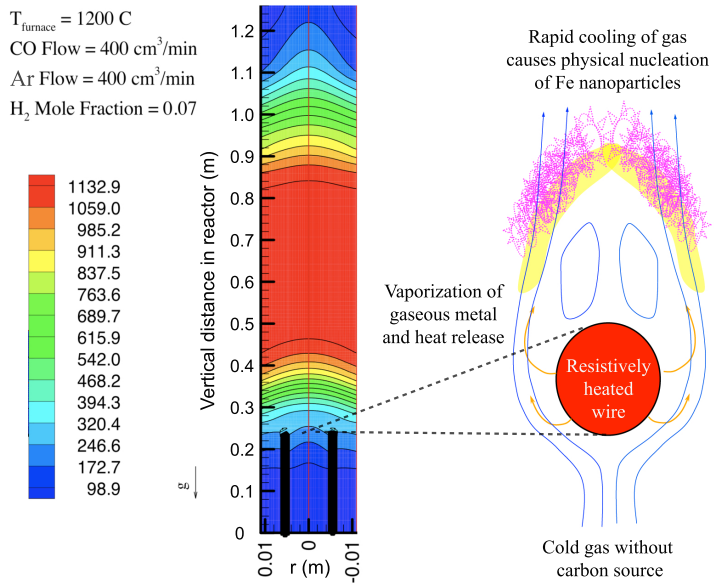

Figure 2.3 (Left) Computational fluid dynamics calculations for the temperature contours in the HWG reactor, calculated for a set temperature of 1200 °C. Adapted with permission from [116], Copyright © 2005, Elsevier. (Right) Schematic mechanism for the physical nucleation of iron nanoparticles in the HWG. Courtesy of David Brown.

2.1.3. Sample collection

A great advantage of these reactors is that the synthesis process is continuous and samples can be collected, or gas and aerosol measurements made, without disturbing the reactor atmosphere. The material is dry-deposited directly from the reactor as films on various substrates, and no solution processing, sonication or centrifugation is applied. This ensures that the intrinsic properties of the material are preserved. As-grown SWCNTs are carried downstream of the furnace by the gas flow, where they are collected directly at the reactor outlet either by filtering onto microporous membrane filter papers (Figure 2.4), or by using an electrostatic collector [120] (EC, Figure 2.5).

Collection by electrical field is possible if the SWCNTs are charged, which can be done either by a radioactive bipolar charger, or by a corona charger. However, it had been previously observed that SWCNT bundles synthesized in both the ferrocene and HWG systems are naturally charged, with up to 5 elementary charges, both positive and negative [142]. Moreover, it was found that the higher the concentration of SWCNTs, the higher the charging. Carbon-containing ions were found to be responsible for the negative charging of the CNTs, while positive charging occurs because of electron emission. A bundle can become charged due to the emission of electrons and ions, which dissipate the van der Waals energy released during CNT bundling. This energy can be significant since the individual tubes are typically at least hundreds of nm long.

The fact that the SWCNT bundles in the aerosol are charged means that the EC can be used to collect nanotube networks [120] on many different substrates such as SiO_2 (for SEM measurements) or Au(111) (for STM/STS measurements) without any processing or dispersion. The EC is a cylindrical chamber with an inner horizontally positioned metal electrode, where a substrate is placed, as shown schematically in Figure 2.5. A constant negative potential is applied to this electrode, resulting in an electric field between the electrode, surrounded by an electrical shielding (teflon), and the cover of the precipitator, which guides positively charged [142] SWCNT bundles towards the substrate surface. Alternatively, a positive potential can be used to attract negatively charged SWCNT bundles. Using an electric field of 6 kV/cm with a 300 cm^3/min collector flow, ultrasparse submonolayer networks could be collected in few tens of seconds.

Similarly, samples could be collected directly onto TEM grids using an electrostatic precipitator (ESP) corona charger, which ensures that individual tubes are collected efficiently as well. Collection times for the TEM grids were 5–10 minutes using a 300 cm^3/min collector flow.

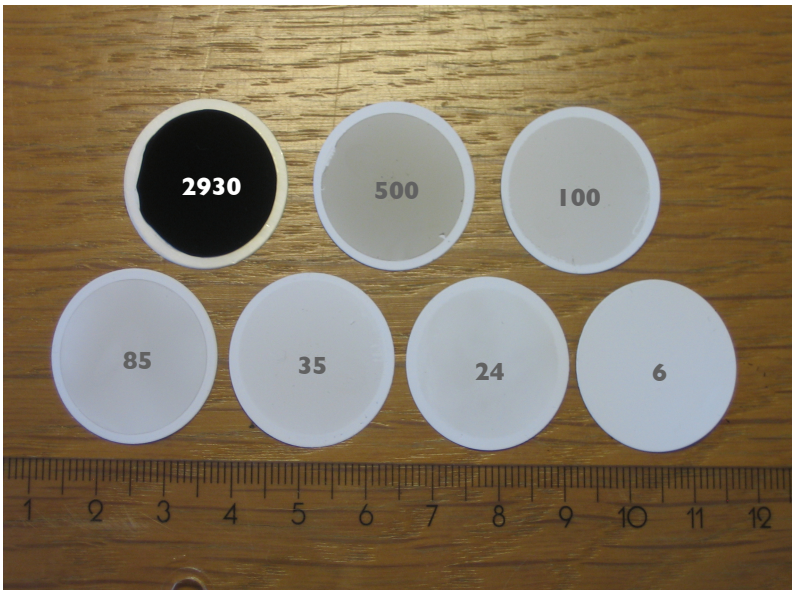

Figure 2.4 SWCNT films of various thicknesses (estimated by SEM, shown in nm) could be collected by filtering simply by varying the collection time. Reproduced with permission from [143], Copyright © 2008, Elsevier.

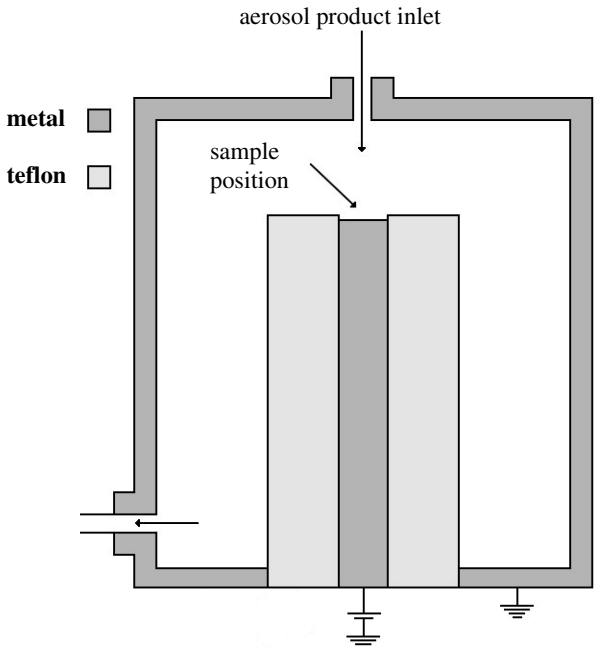

Figure 2.5 Schematic of the electrostatic collector (EC) used for SWCNT deposition onto practically any substrate at room temperature directly from the floating catalyst reactors. Reproduced with permission from [120], Copyright © 2009 IOP Publishing Ltd.

2.2. Characterization

2.2.1. Electron microscopy

2.2.1.1. Scanning electron microscopy

In a scanning electron microscope (SEM, Figure 2.6), an electron beam is produced by either field or thermionic emission, with primary electron energies of typically 1–10 keV. The beam is focused by an electromagnetic electron lens system into a spot 1–10 nm in diameter on a sample surface [144]. The focused beam is scanned in a raster across the surface by a deflection coil system in sync with an electron beam of a video tube, which is used as an optical display. Both beams are controlled by the same scan generator and the magnification given by the size ratio of the display and scanned area on sample. A two-dimensional map of the signal yields a SEM image. Usually systems have a separate detector-processing system, which is used for capturing images with a slower scan rate for better image quality. Most systems also feature several different imaging methods.

The main application of SEM is the visualization of sample surface topology (such as CNT network morphology), although elemental analysis is also possible. The secondary electrons (SE) with energies of a few eVs are collected by a directional detector. Due to the angular dependence of the SE yield and a shadowing effect, the SE image shows the surface topography. With modern SEMs, accelerator voltages of around 1 kV yield resolutions of 2–3 nm, while the best 15 kV devices can achieve 1 nm resolution.

SEM measurements were made by the co-authors with a Leo Gemini 982 at 2 kV (Publication II) and a Jeol JSM-7500F at 1 kV (Publication IV).

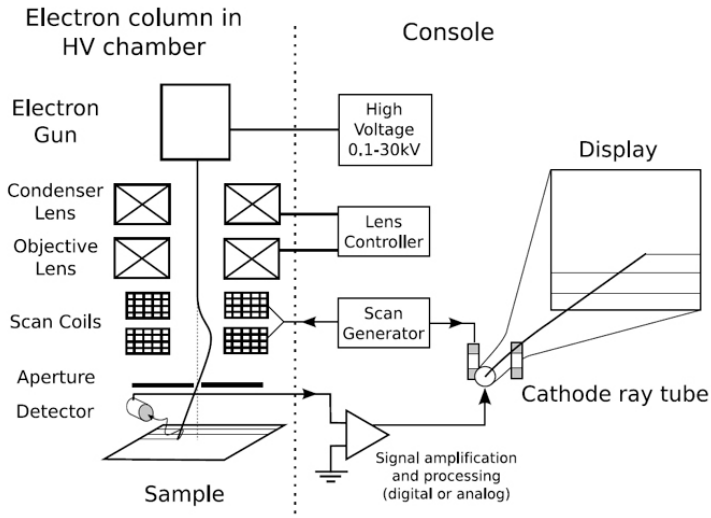

Figure 2.6 Schematic drawing of a scanning electron microscope. HV denotes high vacuum. Reproduced with permission from [145].

2.2.1.2. Transmission electron microscopy

In a transmission electron microscope (TEM, Figure 2.7), a parallel beam of electrons emitted by an electron gun is focused by a condenser lens onto the sample. The electron beam travels through the specimen, and some of the electrons are scattered. The transmitted portion is focused by an objective lens to project a magnified image onto a screen. In basic TEM, the whole image area is illuminated with electrons. Alternatively, in scanning TEM, a very narrow electron beam is scanned in a raster over the sample.

Due to a limited penetration depth and multiple scattering of electrons in solids, the samples should be very thin (the larger the atomic number of the material, the greater the scattering and thinner the sample must be). The diffraction limit for TEM resolution can be estimated from $\Delta = 0.5\lambda/\sin\alpha$, where λ is the electron wavelength and α equals one-half the angular aperture. For a 100 keV voltage ($\lambda = 0.037$ Å), diaphragm radius of 20 μm, and focal length of 2 mm, this yields $\Delta \approx 2$ Å [144]. In practice, the resolution is usually worse due to non-ideality of the electron lenses.

When passing through a sample, the electron flux loses a part of its intensity due to scattering. This part is greater for thicker regions, or regions with species of higher atomic number. If the objective aperture effectively cuts off the scattered electrons, the thicker regions and the high atomic number regions appear dark. This is called bright field imaging. Smaller aperture enhances contrast, but also leads to the loss of resolution. In diffraction contrast TEM instruments, crystal structure can also be investigated by high resolution transmission electron microscopy (HRTEM). This is also known as phase contrast imaging since information is coded in the interference pattern of the electron waves. With modern spherical aberration-corrected electron optics, resolutions below 0.5 Å have been achieved [146], along with elemental identification of single atoms [84, 147].

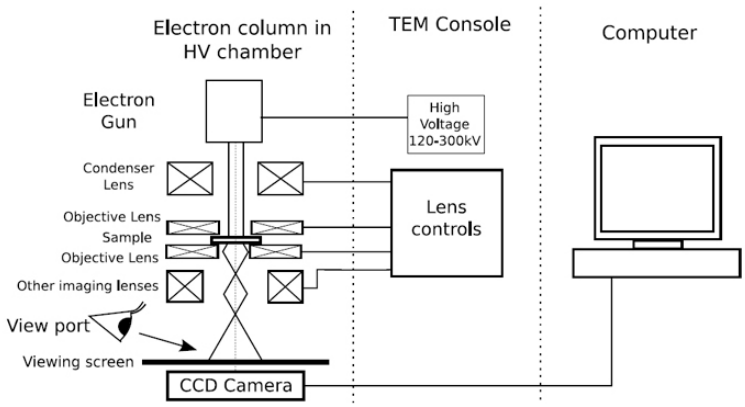

Figure 2.7 Schematic drawing of a transmission electron microscope. Reproduced with permission from [145].

Electron diffraction (ED) is a technique used to study matter by firing electrons at a sample and observing the resulting interference pattern arising from the wavelike nature of electrons. The periodic structure of a crystalline solid acts as a diffraction grating in scattering electrons. Analysis of the observed diffraction pattern allows in some cases to deduce the structure of the crystal producing the diffraction pattern.

As an additional TEM technique, ED was the first method to be used to identify the SWCNT crystalline structure [1], and has remained one of the most powerful means for their structural analysis. By manipulating the electromagnetic lenses of the TEM, a diffraction pattern may be observed instead of the image. Since nanotube properties are so sensitive to chirality (for instance, a (13,1) tube is metallic while a (14,1) tube is semiconducting, even though they are geometrically very similar to each other), accurately determining the chiral indices (n,m) is extremely important.

Recently, a method of analyzing TEM nanobeam electron diffraction patterns of SWCNTs was developed by Jiang and coworkers [148] based on a concept of 'intrinsic layer-line spacing'. The diffraction pattern of an individual SWCNT is composed of many separate layer-lines parallel to each other but perpendicular to the tube axis. There are three principal layer lines above and below the equatorial line due to the principal reflections of graphene (Figure 2.8). Jiang et al. developed an efficient, unambiguous, and calibration-free method for direct determination of (n,m) chiral indices of SWCNTs from their EDPs. The tilt angle of the carbon nanotube with respect to the incident electron beam – a problem in previous analysis methods [149] – is simultaneously evaluated, and the effect of the tube inclination totally compensated.

TEM and ED observations were carried out by the co-authors with a Philips CM200 microscope (Publications I–V) and a JEOL-2200FS double aberration-corrected microscope (Publication II), both operated at 80 kV.

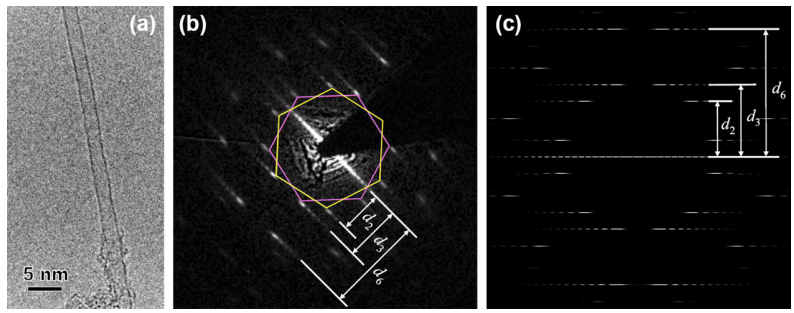

Figure 2.8 (a) A high-resolution TEM image of an individual SWCNT; (b) the corresponding experimental EDP and (c) a simulated EDP of a (23, 10) SWCNT at a tilt angle 10°. The d_i (i=1...3) denote the three layer lines used in the analysis. Reproduced with permission from [148], Copyright © 2007, Elsevier.

2.2.2. Optical probing of nanotube properties

2.2.2.1. Optical absorption spectroscopy

In optical absorption spectroscopy, the absorption of light as a function of frequency or wavelength is measured (Figure 2.9). The sample absorbs photons from the incident light, and the intensity of the absorption varies as a function of frequency. In the case of carbon nanotubes, the most interesting features in the optical absorption spectra (OAS) are the peaks corresponding to the first optical transitions of the semiconducting and metallic tubes, typically with energies in the range of 0.5 to 2.5 eV (wavelengths from 500 to 2500 nm in the visible and near infrared ranges).

Optical absorption spectra can be used to evaluate the diameter distributions of SWCNTs, since all types of nanotubes have transitions in the UV–Vis–NIR region [150]. Recently, a new method for quantifying the diameter distributions of SWCNTs was developed by Tian et al. [151]. To fit the measured optical spectra, it was assumed that a spectrum is a linear combination of background absorption (due to graphitic carbon, catalyst particle scattering, and the π–plasmon peak) and contributions from the SWCNT material. After background subtraction [151], the remaining spectrum is further assumed to be a linear combination of different nanotubes' interband electronic transitions. These are calculated according to a Kataura plot [152] based on an extended tight-binding model (Figure 2.10), taking into account orbital rehybridization due to curvature effects [153], and many-body corrections including both exciton and self-energy corrections applied using empirical corrections [154, 155]. The method has been validated for undoped SWCNT films [151].

In this work, absorption spectra of thin film samples were measured using a double line UV–Vis–NIR spectrophotometer (Perkin-Elmer lambda 900) from films transferred onto quartz glass.

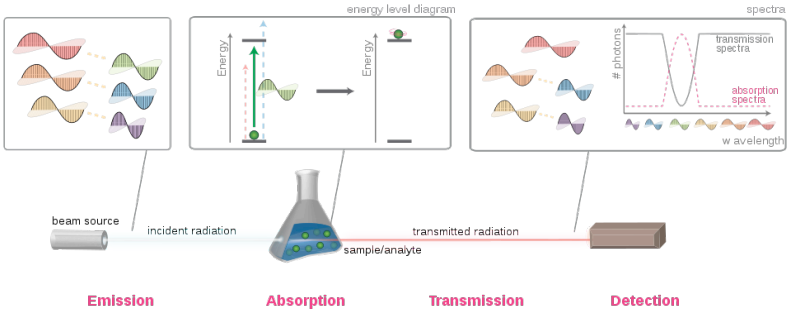

Figure 2.9 A white beam source is focused on a partially transparent sample. Upon striking the sample, photons that match the energy gap of the molecules present are absorbed and excite the molecules. By comparing the attenuation of the transmitted light with the incident, an absorption spectrum is obtained. Reproduced from [156] under the CC BY–SA 3.0 license.

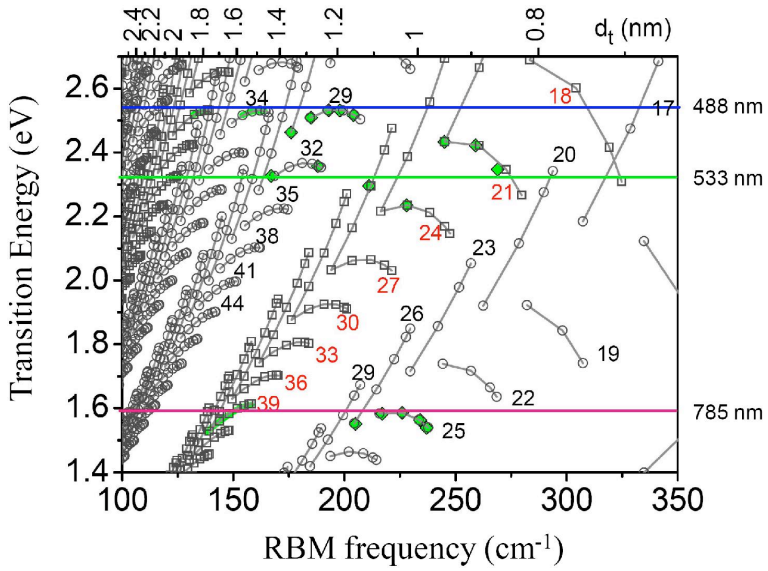

Figure 2.10 Optical transition energy E_{ii} calculated by an ETB/MB model [151] as a function of the RBM frequency (nanotube diameter). The open circles and the open squares are semiconducting and metallic SWNTs, respectively, divided into $2n + m$ = const families joined by solid lines. Reproduced with permission from the supporting information of [151].

2.2.2.2. Raman spectroscopy

The principles of Raman spectroscopy of SWCNTs were discussed in Section 1.1.2 and the expected changes induced to the spectra by nitrogen doping in Section 1.2.2. In the context of this work, we concentrated our attention on the RBM, D and G, and the G' bands. The measurements were done on thick film samples collected on the membrane filters or transferred onto glass, in each case ensuring that substrate effects did not affect the measurements. However, we note that most of the nanotubes in the samples were in relatively small bundles. The laser spot sizes were in the order of a micrometer.

In Publications I and IV, Raman spectra were measured using a single 632.81 nm HeNe laser (Jobin Yvon Labram 300, Stigmatic 300 spectrograph). In Publication III, multi-frequency Raman was performed by the co-authors by recording spectra with a Dilor xy triple monochromator spectrometer for the 488, 514, 568, and 632 nm excitation wavelengths. Additionally, a Bruker Fourier transform (FT)–Raman spectrometer operating in ambient conditions with a 1064 nm excitation was used. We did not attempt to analyze the SWCNT diameter distribution in the samples from the Raman spectra since the OAS method is more appropriate for a bulk sample with a range of diameters. The G/D ratio in Raman was also used to assess the quality of the SWCNTs in Publication I.

2.2.3. Detection of nitrogen

2.2.3.1. Electron energy loss spectroscopy

In electron energy loss spectroscopy (EELS), a material is exposed to a beam of electrons with a narrow range of kinetic energies. Some of the electrons undergo elastic scattering, and others scatter inelastically, losing energy and having their paths slightly randomly deflected. The amount of energy lost can be measured with an electron spectrometer and interpreted for the cause of the energy loss. Inelastic interactions can be either high or low loss, and include phonon excitations, inter and intra band transitions, plasmon excitations, and inner shell ionizations. The inner shell ionizations are particularly useful for detecting different elements in the sample.

EELS in a TEM makes possible the chemical and electronic investigation of a material at a nanometer spatial resolution. In particular, electron energy loss near edge structure (ELNES), arising from the energy distribution of the empty electronic states above the Fermi level, can provide information on the local density of empty states, bonding, and local coordination. Elemental mapping can be accomplished either by energy-filtered TEM (EFTEM) or by EELS using spectrum-imaging (SI) acquisition mode in a scanning TEM (STEM). In the SI mode [157], one EEL spectrum is recorded for each position of a small probe scanned over the sample. The clear advantage of the SI technique is the high degree of both spatial and energy resolution, ideal for studying CNTs [109, 158].

In the case of SWCNTs, the ELNES of the carbon K (C–K) edge consists of a π^* peak at ~285 eV and a σ^* band starting at ~292 eV, signatures typical for the sp^2 hybridization of the C atoms in a graphitic network (Figure 2.11). If nitrogen is present, the total nitrogen concentration can be calculated [70, 97, 158] from the N–K edge signal. The drawback of the method is that despite the reasonably good energy resolution, only relatively short integration times are possible due to electron beam damage considerations and sample stability. The background from the C–K edge and the high noise level makes it challenging to record good enough spectra so that reliable spectral deconvolution could be made to identify different nitrogen contributions, which are quite close in energy.

In the specific measurements discussed in Publications III and IV, EELS spectra were recorded by the co-authors using a VG-HB501 scanning transmission electron microscope (STEM) equipped with a cold field emission gun (FEG), operated at 100 keV with an energy resolution close to 0.7–0.8 eV in the core-loss region. Convergence angle on the sample and collection angle of the spectrometer were 15 and 24 mrad, respectively. The spectroscopic information was obtained using the spectrum-imaging (SPIM) acquisition mode [157, 158]. For the spectra acquisition, a slightly defocused electron probe was scanned in a small area of a few nm^2.

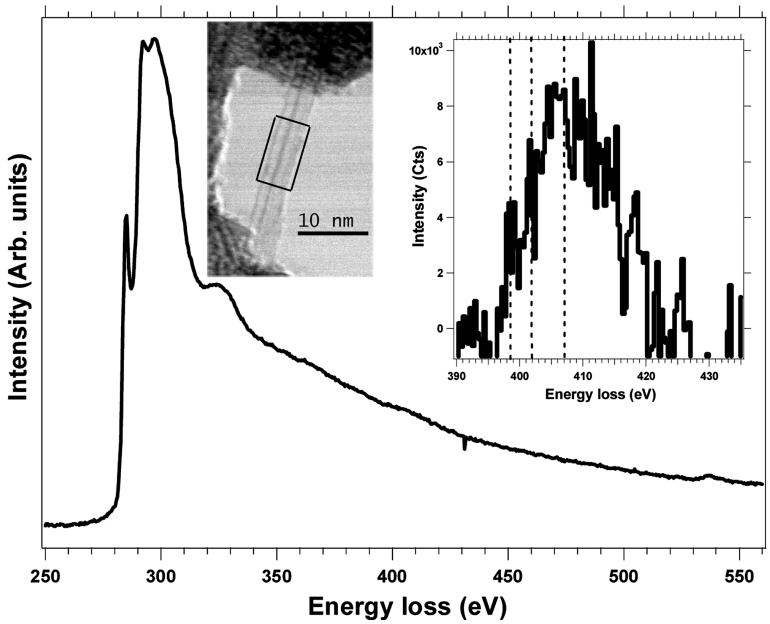

Figure 2.11 EEL spectrum recorded on a N-SWCNT bundle synthesized with laser ablation (inset). The spectrum displays the C– and N–K edges, with a magnification of the N–K edge in the inset. Reproduced with permission from [109], Copyright © 2009 American Chemical Society.

2.2.3.2. Scanning tunneling microscopy

Scanning tunneling microscopy (STM) is based on the concept of quantum tunneling. When a conducting tip is brought so close to a sample surface that the wave functions of the sample and tip atoms overlap, and a voltage bias applied between the two, electrons can tunnel through the vacuum between the tip and the sample. The resulting tunneling current is a function of tip position, applied voltage, and the local density of states (LDOS) of the sample. A topographical image is formed by recording the current as the tip position scans across the surface. Alternatively, the LDOS as a function of energy at a specific location in the sample can be obtained by recording the current as a function of bias voltage. This is called scanning tunneling spectroscopy (STS).

STM and STS are powerful techniques for investigating the atomic and electronic structures since atomically resolved images of nanotubes can be achieved along with local spectroscopy [159, 160]. The visualization of a single nitrogen atom in the carbon network is thus possible, and the change in local density of states induced by the dopant can then be investigated by STS and compared to simulations [68]. The technique has been recently applied to N-SWCNTs synthesized with laser ablation [78], though no conclusive identification of specific nitrogen sites could be made.

2.2.3.3. X-ray photoelectron spectroscopy

X-ray photoelectron spectroscopy (XPS) is a quantitative spectroscopic technique that measures the elemental composition and chemical and electronic state of elements within a material. XPS spectra are obtained by irradiating a material with a beam of X-rays while simultaneously measuring the kinetic energy and number of electrons that escape from the top 1 to 10 nm of the material where the X-rays penetrate (Figure 2.12). XPS requires ultra high vacuum.

Because the energy of an X-ray with a particular wavelength is known, the binding energy E_{bind} of each of the emitted electrons is determined as

$$E_{bind} = E_{X\text{-}ray} - (E_{kinetic} - \varphi) , \qquad (2.1)$$

where $E_{X\text{-}ray}$ is the energy of the X-ray photons being used, $E_{kinetic}$ is the kinetic energy of the electron as measured by the instrument, and φ is the work function of the spectrometer. The binding energy of a core electron depends not only upon the level from which photoemission is occurring, but also upon the oxidation state of the atom and the local chemical and physical environment. These give rise to small shifts in the peak positions in the spectrum, the so-called chemical shifts. Such shifts are readily observable and interpretable in XPS spectra by comparison to known values or computer simulations.

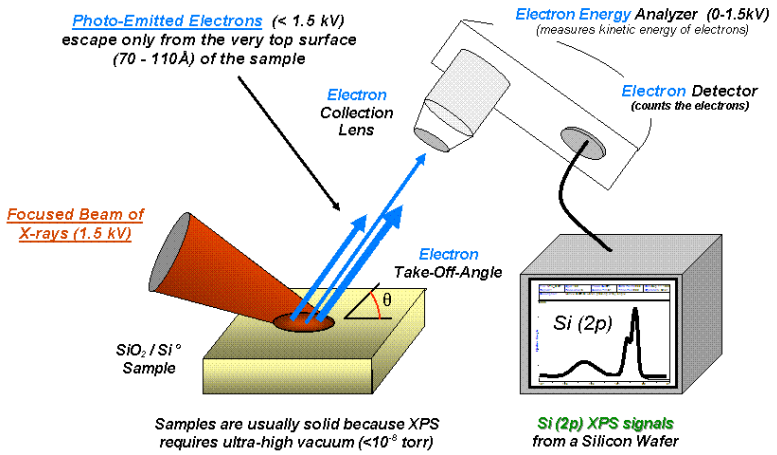

Figure 2.12 A schematic depicting the photoelectric effect and XPS, illustrated for the case of the Si 2p state. From the public domain.

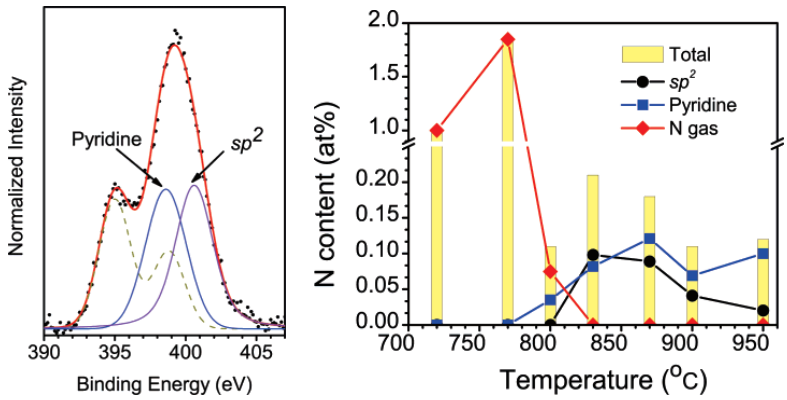

Figure 2.13 The N1s core signal corresponding to N-SWCNTs synthesized with benzylamine. The deconvolution shows the presence of pyridinic and substitutional nitrogen. These appear in roughly equal proportions depending on the synthesis temperature, along with N_2 gas. Adapted with permission from [82], Copyright © 2007, American Chemical Society.

The advantages of XPS compared to EELS are better energy resolution and longer integration times made possible by the use of X-rays instead of electrons as the probe beam. When inspecting spectra from N-SWCNTs, the recorded spectra are analyzed taking into account the atomic cross sections of the C and N species to give an adequate estimate of the atomic concentrations based on the relative peak intensities. Also, the C1s signal should be inspected as a prerequisite for any further measurement of the nitrogen heteroatoms.

By analyzing the N1s response, XPS can be used to detect heteroatom percentages as low as 0.2 at. %. However, it is important to note that N_2 and other nitrogen-containing gaseous byproducts can be trapped in the samples [82]. If the tools employed and the interpretation of results are not adequate, these can be mistakenly considered as wall dopants. Thus a sufficiently high energy resolution and a careful deconvolution of the N1s response are the essential for the correct use of XPS for analyzing doping. If the material consists of sufficiently pure SWCNTs, the spectral deconvolution of the N1s line can be reliably made and the bonding configurations in the sample resolved. XPS studies have shown that the binding energies of the pyridinic (~398.6 eV) and substitutional (~400.5 eV) nitrogen can appear in roughly equal proportions in N-SWCNTs (Figure 2.13) in optimal synthesis conditions [82].

In publication IV, the co-authors employed XPS to estimate the overall N concentration in the unpurified N-SWCNT samples using a PHI 5600 spectrometer equipped with a monochromatic Al Kα source (1486.6 eV) at a base pressure of 10^{-9} mbar and an overall spectral resolution of 0.5 eV.

2.2.4. Sheet resistance

The optical and electrical characteristics of SWCNT films thicker than a few separate monolayers can be described by bulk material conductivity laws [118]. The quality of transparent conducting thin films is usually stated as their sheet resistance (R_s) versus optical transmittance (T) at a reference wavelength (550 nm). By starting from the Beer-Lambert law for the absorbance $A(\lambda)$ a film of thickness L

$$A(\lambda) = -\ln T(\lambda) = \varepsilon(\lambda)\, \mathrm{d}L \tag{2.2}$$

for the wavelength λ, and the definition of sheet resistance R_s (or sheet conductance, σ_s)

$$R_s = 1/\sigma_s = \varrho_e\, a/aL = \varrho_e/L = 1/\sigma L, \tag{2.3}$$

where a is the sheet area, σ is the electrical DC conductance and ϱ_e the electrical resistivity, we can relate the two measures to each other by

$$R_s = -\varepsilon\varrho/(\sigma \ln T) = -1/(K \ln T), \tag{2.4}$$

where ε is the Beer-Lambert extinction coefficient and ϱ is the film density, which is not generally known. Nevertheless, we can sidestep this by calculating the ratio

$$K = \sigma/\varepsilon\varrho \tag{2.5}$$

from Equation 2.4 using experimentally measurable resistance and transmittance values for use as a figure of merit for the optoelectronic performance of the films. This relation clearly shows that for structurally similar films with similar values of ε and ϱ, the R_s/T ratio is controlled by the conductance σ, which further depends on factors such as the morphology of the random network comprising a SWCNT film [161]. The electrical conductivity of a SWCNT network is limited by highly resistive junctions between SWCNT bundles [127]. Therefore, increasing the length of the SWCNT bundles is known to decrease the network resistivity because of a smaller number of contacts in series.

The sheet resistances of SWCNT thin films can be easily measured using a four-point linear probe. The key advantage of four-terminal sensing is that the separation of current and voltage electrodes eliminates the impedance contribution of the wiring and contact resistances, yielding a value for the sheet resistance after a known geometric correction factor is applied (that depends only on the probe geometry). The measurements in Publication IV were made using an Agilent 34410A multimeter and a Jandel Engineering, Ltd. four-point probe.

2.3. Gas analysis

2.3.1. Fourier transform infrared spectroscopy

Molecular bonds in compounds vibrate at various frequencies depending on the elements and the types of bonds. For any given bond, there are several specific frequencies at which it can vibrate. According to quantum mechanics, these frequencies correspond to the ground state and several excited states. A way to cause the frequency of a molecular vibration to increase is to excite the bond by having it absorb energy from a photon. For any given transition between two states, the energy (determined by the wavelength) must exactly equal the difference in the energy between the two states. These are usually the ground state E_0 and the first excited state E_1, having an energy difference of

$$E_1 - E_0 = hc/\lambda, \tag{2.6}$$

where h is the Planck constant, c is the speed of light, and λ is the wavelength. The energy corresponding to these transitions between molecular vibrational states generally falls on the infrared portion of the electromagnetic spectrum.

Fourier transform infrared spectroscopy (FTIR, Figure 2.14) is a technique where spectra are collected based on measurements of the temporal coherence of an infrared (IR) radiative source, using time-domain measurements. The IR radiation is passed through a sample of gaseous molecules. Some of this radiation is transmitted through while the rest is absorbed by the sample, producing an infrared spectrum. In order for a vibrational mode in a molecule to be IR active, it must be associated with changes in the permanent dipole. Simple diatomic molecules have only one bond and thus only one vibrational band. If the molecule is symmetrical, e.g. N_2, the band is not observed in the IR spectrum. Non-symmetrical diatomic molecules, e.g. CO, do absorb in the infrared and can be identified by FTIR (Figure 2.14).

By interpreting an IR absorption spectrum, the chemical bonds in a molecule can be determined. Spectra of pure compounds are generally unique molecular ‘fingerprints’. While organic compounds have very rich, detailed spectra, inorganic compounds are usually much simpler. For most common materials, an unknown spectrum can be identified by comparison to a library of known compounds.

This technique was applied in Publications I and IV–VII using a GASMET DX4000 device to measure the concentrations of CO, CO_2, H_2O and HCN gases, determined by comparison to reference spectra. To identify less common materials, or symmetric molecules without IR absorption, FTIR needs to be combined with other techniques, such as mass spectrometry.

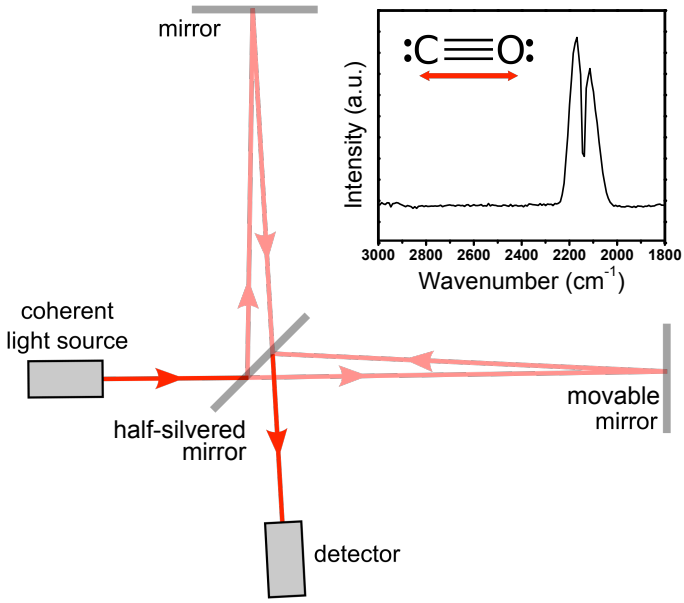

Figure 2.14 The FTIR spectrometer is a Michelson interferometer, where one of the two mirrors is movable and fully reflecting, allowing a variable travel-time delay in one of the beams. The sample would be placed between the half-silvered mirror and the detector. Adapted from [162] under the Creative Commons BY-SA 3.0 license. The inset shows an FTIR spectrum for carbon monoxide (CO), and the vibrational mode responsible for the IR absorption.

2.3.2. Residual gas analysis

Residual gas analysis refers to an analytical technique used for identifying gases present in vacuum environments, although implementations exist for sampling from atmospheric pressures as well. A residual gas analyzer (RGA) is a small and usually rugged mass spectrometer. The molecules of the gas being analyzed are turned into ions by impact ionization. The ionizing electron beam is generated by a hot emission filament and extracted by an electric field. As the hot filament is easily destroyed by reactive gases like oxygen, the analysis chamber needs to be kept in vacuum even when the gas being sampled is at atmospheric pressure.

The ions from the analyte gas are distinguished from each other in terms of their masses by the mass analyzer of the RGA. There exist various techniques for mass separation, but quadrupole mass spectrometers are widely used for many atmospheric pressure gas analysis requirements. Gas composition can be monitored over a wide dynamic range from parts per billion to percentage levels.

RGA was applied in Publication VII using a MKS Cirrus RGA device to complement FTIR measurements by measuring the concentrations of H_2 and N_2 in the reactor outlet gases.

2.4. Computational

2.4.1. Network resistance modeling

Measurements of the resistance of SWCNT bundles [163] and bundle–bundle contact resistances [127] have shown that resistance along SWCNT bundles is low compared to the junctions. This means that the network can be described by an analogous network of resistors representing the contact resistances, ideally connected by the bundles.

The dependence of the network conductivity on its morphology was studied using a random resistor network model developed with the co-authors in Publication IV. The network is represented as an equivalent circuit in which the nodes represent CNT bundles, and resistors between them represent bundle–bundle contacts. The circuit is created by randomly and isotropically generating line segments with an experimentally motivated lognormal length distribution in a square area, registering intersections between the segments and mapping each segment as a node and each intersection as a resistor. Finally, intersections with the upper and lower edges of the square are registered. The resistance is calculated by elementary circuit analysis, using one horizontal edge of the square as the ground and calculating the node voltage at the opposing edge by solving the linear system $G\upsilon = i$, where υ is the node voltage vector and i is a source vector, and where $i(1) = 1$ and 0 otherwise.

We studied the dependence of the conductance and network connectivity, defined as the average number of intersections per bundle, on the average bundle length by generating networks with varying length distributions, averaging over 100 individual simulations per distribution. In all simulations, a fixed density of (total segment length)/(square area) was used and set high enough to make the networks nearly or completely connected. Thus they were far above the percolation threshold, where only few conducting pathways exist through the network. To ensure the non-singularity of G, stray segments not connected by any path to the ground and reference nodes were eliminated. Additionally, the dependence of the network connectivity on average bundle diameter was studied by generating networks where the bundles were represented by tilted rectangles instead of simple line segments. Since we concentrated in obtaining the general forms of scaling between the mentioned parameters, the contact resistances in the simulations were normalized to 1 Ω in all cases. It is worth noting that contact resistances have been experimentally shown to change dramatically with large changes in the diameters of the connected bundles [127]. As in our simulation the bundle diameters are thought to be fixed and small compared to the lengths, and orientations are perfectly isotropic, these variations average out.

2.4.2. Density-functional theory

A metal catalyst nanoparticle is essential for SWCNT growth. Thus it is very important to understand the carbon chemistry taking place on nanometer size particles. Real nanoclusters have several unique active sites like facets and vertices between the facets, which can have catalytic properties that differ drastically from the ones on almost all other surfaces. Gas measurements can give information about the overall chemistry taking place in a reactor, but cannot yield local information about the mechanism of the reactions. For this reason the computational approach, where precise sites can be studied, is very attractive.

While a decade ago most theoretical studies tried to describe surfaces either on a qualitative level using empirical parameters or invoked rather severe approximate models, there is now a large class of surface systems that can be addressed quantitatively based on first principles electronic structure calculation methods. This progress is mainly due to advances in computer power and the development of efficient algorithms, incorporated into advanced code packages, each with their own strengths. Most of these rely on some form of density-functional theory (DFT).

DFT is a quantum mechanical method used to investigate the electronic structure of many-body systems. The main idea is to describe an interacting system of fermions via its density and not via its many-body wave function. For N electrons in a solid, which obey the Pauli principle and repulse each other via the Coulomb potential, this means that the basic variable of the system depends only on three – the spatial coordinates x, y, and z – rather than 3N coupled degrees of freedom (or 4N including spin). Thus the unsolvable many-body problem of interacting electrons in a static external potential is reduced to a tractable problem of non-interacting electrons moving in an effective potential. The effective potential includes the external potential and the effects of the Coulomb interactions between the electrons, the so-called exchange and correlation interactions.

The major problem with DFT is that the exact functionals for exchange and correlation are only known for the free electron gas. However, approximations exist which permit the calculation of many physical quantities accurately. In physics, a widely used approximation is the local-density approximation (LDA), where the functional depends only on the density at the coordinate where the functional is evaluated. Generalized gradient approximations (GGA) are still local, but also take into account the gradient of the density at the same coordinate. Using GGA, good results for molecular geometries and ground-state energies have been achieved.

For further details, we refer the reader to the excellent Nobel Lecture of Walter Kohn, one of the original developers of DFT [164].

2.4.2.1. Projector-augmented waves

The remaining one-electron Schrödinger equation still poses substantial numerical difficulties since the wave functions in the core and valence regions behave very differently. The projector-augmented wave (PAW) method [165] overcomes these difficulties by linking the physical wave functions to auxiliary wave functions that can be treated well numerically. Kinks and strong oscillations near the nucleus are augmented, i.e. attached to a numerically smooth auxiliary wave function, which is expanded into plane waves that can be effectively treated in the valence regions.

2.4.2.2. GPAW code

GPAW is a recently developed DFT code [166] based on the PAW method. It uses real-space uniform grids and multigrid methods. Two kinds of grids are involved: a coarse grid used for the wave functions and a fine grid used for densities and potentials. Since GPAW uses real-space grids (and not plane waves as e.g. VASP [167]) it scales very efficiently to a huge number of processors, allowing systems with a large number of electrons to be studied.

The use of the PAW method allows disregarding of the core electrons and working with soft pseudo valence wave functions. This is important for the efficiency of calculations of transition metals such as iron. Even so, iron remains a difficult metal to study, since it has a large magnetic moment and in a cluster geometry, the spin orientation is determined by subtle effects. Therefore, the effects of spin polarization and non-collinear magnetic moments need to be fully incorporated [168, 169] in the calculations if accurate reaction barriers are to be obtained.

In the calculations performed by the co-authors in Publications VI & VII, the adequacy of the functional form, used bands and spacing of the grid were tested against calculation of the cluster geometry. The GGA functional was RPBE [170].

2.4.2.3. Nudged elastic band algorithm

Reaction barriers are more demanding to study and special transition state search algorithms, like climbing-image nudged elastic band (CI-NEB) [171], need to be used for their determination. In this algorithm, a set of 3N-dimensional images of an adsorbate system is generated between the endpoint configurations corresponding to optimal absorption sites for the reactants. A harmonic interaction between adjacent images is added to ensure the continuity of the path, thus mimicking an elastic band. An optimization of the band, involving the minimization of the forces acting on the images, brings the band to the minimum energy path. This yields the energy barrier for the reaction. However, since the NEB method does not consider entropic effects, a direct comparison to experiments is not strictly possible.

3. Results

We will not aim to reiterate here all the results of the publications contained in this thesis. Instead, we will aim to highlight the major results and significant effects we observed. Details can be found in the respective publications and references therein.

3.1. Material

3.1.1. Synthesis

3.1.1.1. Ferrocene reactor

In the ferrocene reactor, experiments were conducted at two temperatures: 1060 °C and 880 °C, corresponding to the maximum wall temperature. These were chosen based on previous work at the group for achieving either the highest yield or the longest bundles [118], respectively. Note that the temperatures given in Publications I and III were the set point temperatures of the reactor, which are about 60 °C lower than the maximum wall temperatures considered here. In addition to CO, small amounts of NH_3 (0 to 1000 ppm) and CO_2 (0 to 5000 ppm) were added with the side flow using mass flow controllers (MFCs). At 880 °C, CO_2 is introduced into the reactor for the optimal production of SWCNTs. When 500 ppm of NH_3 was also introduced, there was a decrease in synthesis yield. Almost no nanotubes were produced with 1000 ppm of NH_3 and above. Table 3.1 lists results for the characterized samples.

We must point out here that we only had the opportunity to do EELS measurements on the 1060 °C, 625 ppm NH_3 ferrocene reactor sample discussed in Publication III. Therefore we do not have conclusive proof of the doping in the lower temperature samples (in Publications I and II).

3.1.1.2. HWG reactor

All experimental results from the HWG reactor are from Publication IV. The reactor maximum wall temperature was 890 °C, which had been found [118] to be the optimal temperature to obtain long and high quality pristine nanotubes with 1500 ppm of added CO_2. During the initial experiments with the ferrocene reactor, it was noticed that even very small amounts of

introduced NH_3 have a severe effect on nanotube production (Publication I). Thus, to accurately introduce very small amounts of ammonia, a dilution system was used in the HWG experiments. Set flow rates (0 to 2.0 cm^3/min) of ammonia were diluted with 80 cm^3/min of Ar. Before introducing the mixed flow into the reactor, 65 cm^3/min was diverted into vacuum. The resulting inlet flow rates of ammonia were validated by FTIR and good control was achieved in the 0–500 ppm range.

Collection times for the TEM grids were 5–10 minutes using a 300 cm^3/min flow through the collector. Optically opaque films could be collected on 13 mm diameter filters in about 1 hour using a 1500 cm^3/min collector flow. Typical collection times were 30 minutes, and the characterization results for a representative set of samples are shown in Table 3.2.

Table 3.1. List of samples collected from the ferrocene reactor. The columns show: synthesis temperature, introduced CO_2 and NH_3 flows in ppm by volume of the inlet gas flow, G/D ratios estimated from Raman spectra measured using a 632.81 nm excitation, SWCNT mean diameters estimated from OAS, and the average N content determined by EELS.

Temp. (°C)	NH_3 (ppm)	CO_2 (ppm)	Raman G/D ratio	Mean diam. (nm)	Average N content (at. %)
1060	0	0	9.6	1,5	-
1060	250	0	14.4	1.6	n/a
1060	625	0	4.2	1.4	1.7
880	0	5000	15.6	1.3	-
880	500	5000	46.6	1.8	n/a
880	500	2500	14.0	1.4	n/a

Table 3.2. Properties of CNT films synthesized in the HWG at 890 °C with 1500 ppm CO_2 and 0, 100, 200 and 300 ppm NH_3, collected for 30 min. The columns show: ammonia concentration, average nitrogen content determined by EELS and XPS, mean nanotube diameters determined from OAS, transmittance of 550 nm light, mean bundle lengths determined by SEM (geometric mean ± lognormal distribution scale parameter, see Equation 3.2), sheet resistances of the films measured by 4-probe measurement, and optoelectronic figures of merit K (Section 2.2.4) for the films.

NH_3 (ppm)	Average N content (at. %)		Mean d ± var. (nm)	T @ 550 nm (%)	Bundle length (μm)	4-point R (kΩ / □)	K (□/kΩ)
	EELS	XPS					
0	-	-	1.4±0.3	43	3.0±1.1	0.2	5.20
100	1.2	0.2	1.2±0.3	45	2.1±0.9	2.3	0.52
200	1.7	0.7	1.1±0.2	72	1.2±0.7	12.3	0.24
300	n/a	1.1	1.1±0.2	78	0.5±0.4	29.6	0.12

3.1.2. Microscopy

3.1.2.1. Ferrocene reactor

In Publication I, SEM measurements of the SWCNTs deposited on TEM grids by ESP showed typical random network morphology. Increasing the amount of introduced NH_3 beyond 500 ppm decreased both the number and the lengths of the tubes dramatically. With 250 ppm of NH_3 at 1060 °C and 500 ppm at 880 °C, there remained a significant amount of product.

TEM observations showed that the tubes produced without NH_3 were typical for the ferrocene system, with small bundles of SWCNTs about 300 nm in length at 1060 °C and few μm at 880 °C. Shown in Figure 3.1a is an overview TEM image with two individual SWCNTs from the sample synthesized at 880 °C with 5000 ppm CO_2 and 500 ppm NH_3. A high-resolution TEM image of one of the tubes is shown in Figure 3.1b. The corresponding electron diffraction pattern (EDP) for this and another tube are shown in Figure 3.1c and d. From these the chiral indices of the tubes were indexed [148] as (15,13) and (15,11). In general, the nanotubes were well crystallized. Imaging and electron diffraction were conducted on 152 individual nanotubes or small nanotube bundles, and only SWCNTs were found, indicative of the excellent selectivity for SWCNT production. The yield of nanotubes was lower and the nanotubes bundles smaller in the 500 ppm NH_3 sample.

In Publication III, electron diffraction was conducted on 46 individual nanotubes on a TEM grid sample synthesized with 250 ppm NH_3 at 1060 °C, and their chiral angles determined [148]. It was found that the chiral angle distribution was slightly skewed towards armchair tubes.

The chirality distribution of the lower temperature samples was more striking (Publication II). Based on ED analysis of 108 individual SWCNTs in the 880 °C 500 ppm NH_3 sample, and 95 nanotubes in the 0 ppm NH_3 sample, (n,m) maps were obtained for both samples (Figure 3.2). In the 500 ppm NH_3 sample, in total 37 different chiral structures were identified, of which the three main chiralities (13,12), (12,11) and (13,11) with abundances of 13, 8 and 8, respectively, constitute nearly 30% of the investigated nanotubes. The chiralities of the SWCNTs are seen to be intensively clustered into a narrow region around the semiconducting (13,12) nanotube. By contrast, in the 0 ppm NH_3 sample, the chiralities are more broadly distributed, and a total number of 52 different chiral configurations are recognized, none of which essentially stands out as a principal chirality. We note that the fractions of semiconducting tubes in the above two samples, 65% for the non–NH_3 sample and 74% for the NH_3–enhanced sample, show insubstantial difference from each other, nor from their inherent population of about 67%.

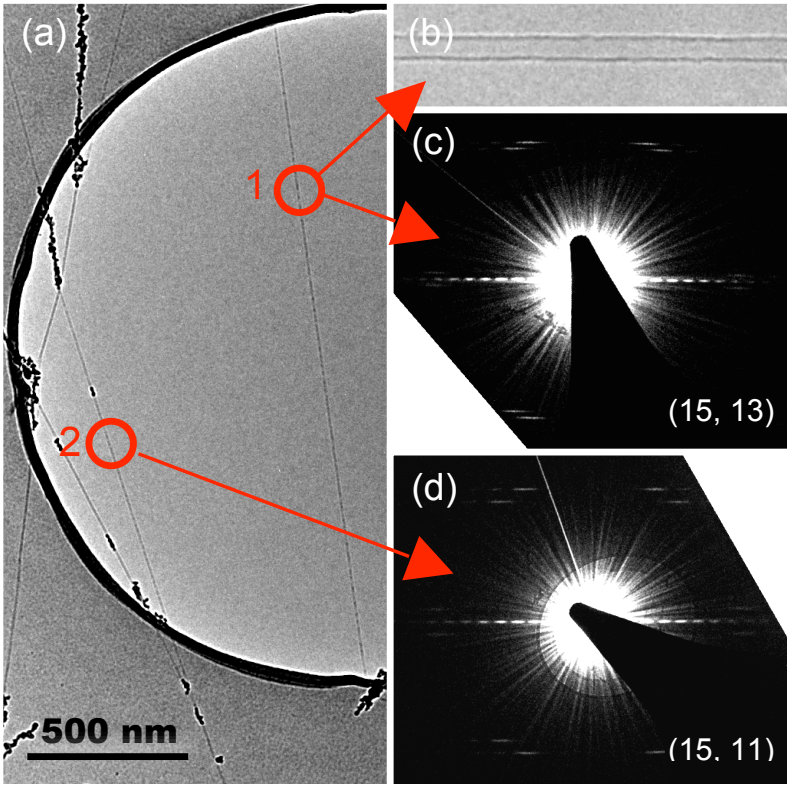

Figure 3.1 a) A TEM micrograph of individual SWCNTs crossing a TEM grid, along with some iron catalyst aggregates that appear dark in the image. The tubes are straight and long (over 2 μm). Both the high-resolution TEM image (b) and ED patterns (c and d) indicate the high quality structure of the nanotubes. Using intrinsic layer line distance analysis [148], the diffraction patterns (c and d) were indexed as (c) (15, 13) and (d) (15, 11), with tube diameters of 1.90 nm and 1.77 nm, respectively.

In general, the nanotube diameters in both samples discussed in Publication II were similar. The average diameter is 1.60 nm for the 0 ppm NH_3 tubes and 1.67 nm, slightly increasing, for the 500 ppm NH_3 tubes. Please note that the 0 ppm NH_3 sample in Publication II is not the same one measured by optical absorption in Publication I (Figure 3.6, Table 3.1), since no original TEM samples were later available from that condition. Therefore we collected the non–NH_3 sample of Publication II later from similar reactor conditions. However, the most important 500 ppm NH_3 sample is the same one discussed in Publication I. For that sample, the mean diameter determined from OAS (1.8 nm) and the diameter from TEM (~1.7 nm) agree quite well considering the limited statistics available.

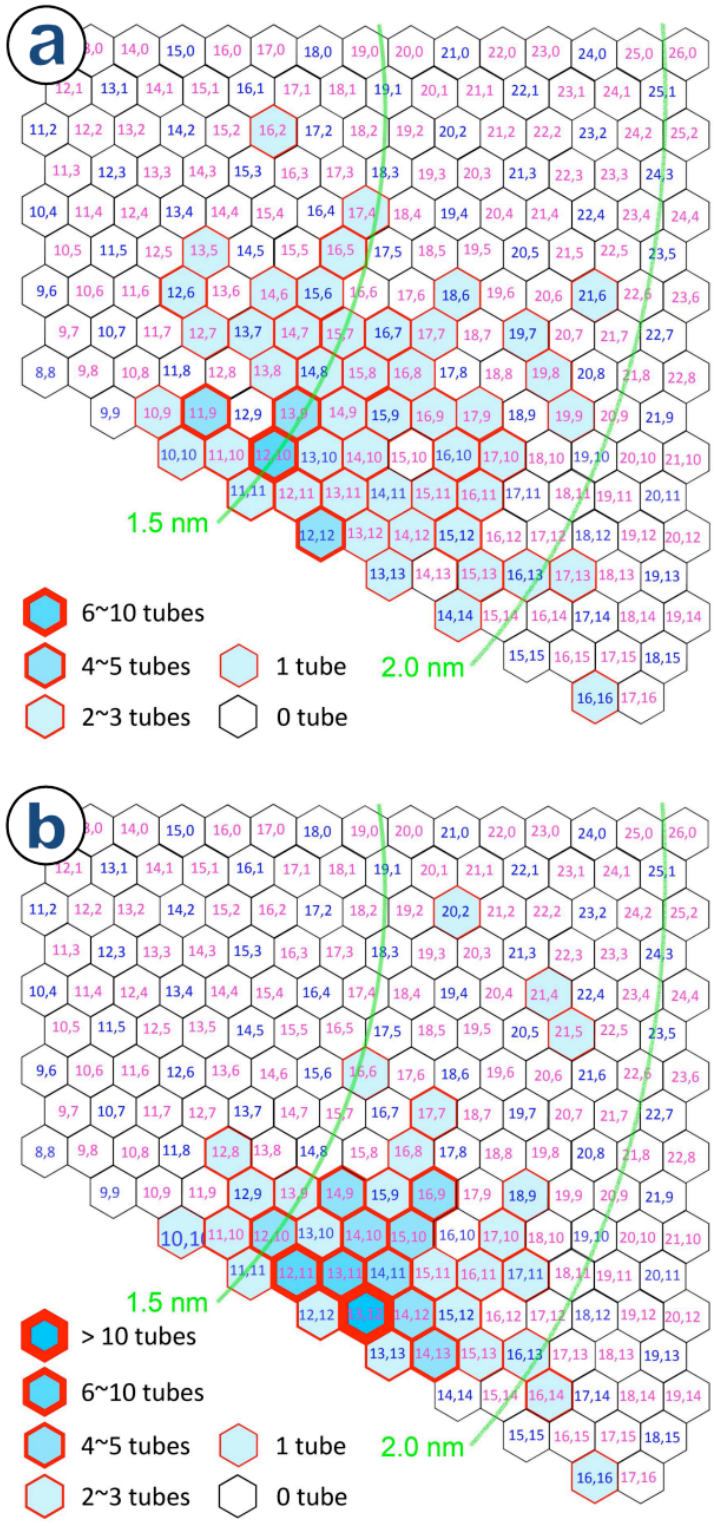

Figure 3.2 (*n*,*m*) maps for samples produced by the ferrocene reactor at 880 °C with 5000 ppm CO_2 and (a) 0 ppm NH_3, and (b) 500 ppm NH_3.

The prominence of the biased chirality distribution in the NH_3–enhanced sample is more effectively displayed in Figure 3.3 (red bars), which illustrates the ratio R_x/R_2 as a function of chiral angle. Here, R_x (x = 1–3) indicates the proportion of nanotubes with chiral angles in the ranges 0–10°, 10–20° and 20–30°, respectively, with R_2/R_2 being of course unity.

Our statistical data show that the 500 ppm NH_3 sample has more than 90% of SWCNTs with large chiral angles in the range 20–30°, and about 50% in the range 27–29°. For the purpose of comparison, Figure 3.3 includes also the R_x/R_2 ratio for the 0 ppm NH_3 sample (blue bars), a CoMoCAT sample [48] (green bars) and a hypothetical ratio calculated based on the theoretical model proposed by Ding et al. [172] (orange bars). It is apparent that the NH_3–enhanced sample stands out, giving an extremely high ratio of R_3/R_2, which demonstrates the high promotion for growing SWCNTs with a narrow chirality distribution by introducing a certain amount of NH_3 into the CVD reaction. It is worth remarking that electron diffraction evaluation of SWCNT bundles leads to the same conclusion.

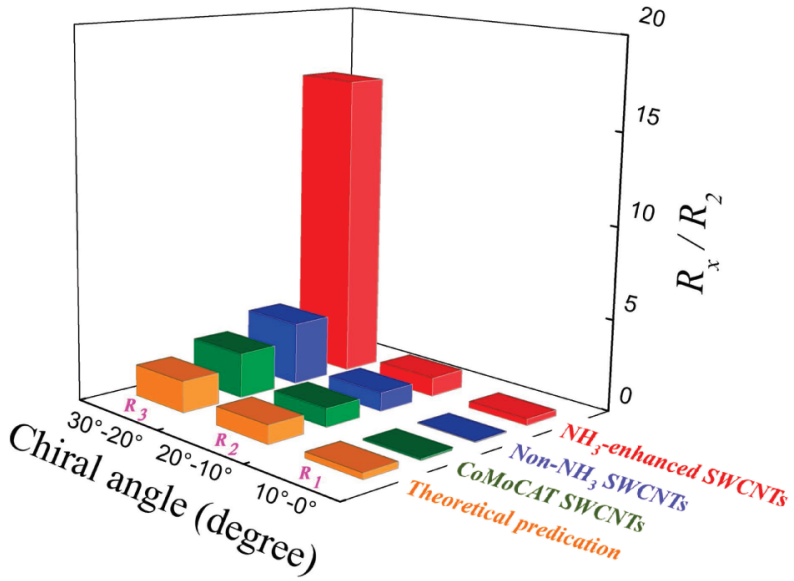

Figure 3.3 Chiral angle distribution in term of the ratio R_x/R_2 as a function of chiral angle. Here, R_x (x = 1–3) represents the proportion of nanotubes with chiral angles in the ranges 0–10°, 10–20° and 20–30°, respectively. The data for CoMoCAT sample is from Ref. [48] (measured using photoluminescence) and the theoretical data from Ref. [172].

3.1.2.2. HWG reactor

Representative scanning and transmission electron microscopy images of the 0 and 200 ppm NH_3 HWG samples are shown in Figure 3.4. The SEM images were recorded directly on samples deposited on membrane filters. The optical, spectroscopic and sheet resistance measurements in Publication IV and the text below were performed on the filter samples. It should be again noted that the material has not been treated or purified in any way, and even so, the optoelectronic properties of the undoped films are excellent (Section 3.1.5.2).

The tubes were typically found in small bundles, with diameters determined by TEM to be 6.1±3.0 nm for the 0 ppm NH_3 sample and slightly smaller, 3.7±1.7 nm for the 200 ppm NH_3 one (50 bundle statistics each). Individual nanotubes could also be quite easily found (Figure 3.5). There seems to be slightly more visible impurities on the undoped bundles, while the doped samples exhibited somewhat larger inactive catalyst particles, as well as shorter bundles. The other doped samples appear similar to the 200 ppm NH_3 one.

Practically no nanotubes were produced with more than 300 ppm NH_3. To understand the sudden disruption of production with higher concentrations, we studied the bundle length distributions by measuring bundle lengths by SEM (50 bundle statistics each) from sparse submonolayer networks deposited by EC onto SiO_2. We found that with increasing NH_3, the bundles became progressively shorter (Table 3.2), decreasing from 3.0 μm in the 0 ppm NH_3 sample to 0.5 μm in the 300 ppm NH_3 sample.

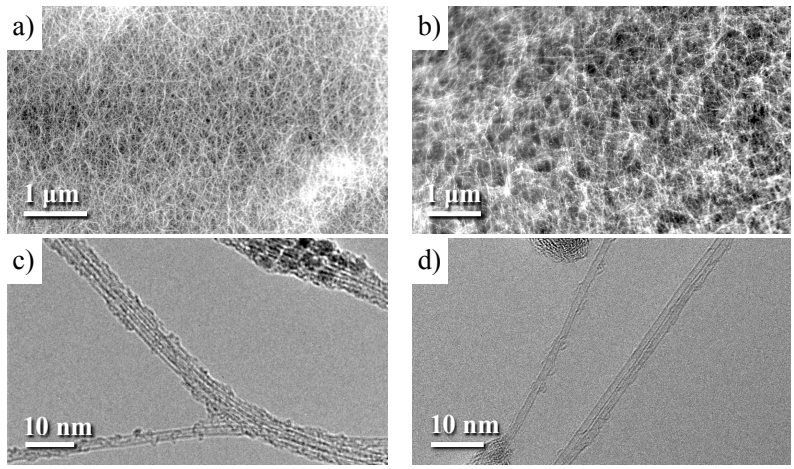

Figure 3.4 Scanning (a–b) and transmission (c–d) electron microscope images of nanotube bundles in samples synthesized in the HWG reactor with a) & c) no NH_3 and b) & d) 200 ppm NH_3.

TEM was also used to determine the diameter distribution of N-SWCNTs synthesized with 200 ppm NH_3. The mean diameter is given as

$$\bar{d} = b \pm c\,, \tag{3.1}$$

where b is the position of the center of a Gaussian peak fitted to the histogram of the diameters (expected value, see Figure 3.9) and c parametrizes its width (square root of the variance). This is related to the full width at half maximum (FWHM) by

$$\mathrm{FWHM} = 2\sqrt{2\ln 2}c \approx 2.355c\,. \tag{3.2}$$

The same convention is used also for the OAS fitting below.

Only individual tubes were used for the determination of their diameter distribution to avoid misidentification of the diameter due to lattice fringes in bundles. The diameters were measured for 56 individual SWCNTs from the distances of the intensity minima in the line profiles of the TEM micrographs (Figure 3.5). Although this might lead to slight inaccuracies in any single diameter, statistically the differences should be insignificant. The mean diameter was found to be 1.1±0.2 nm.

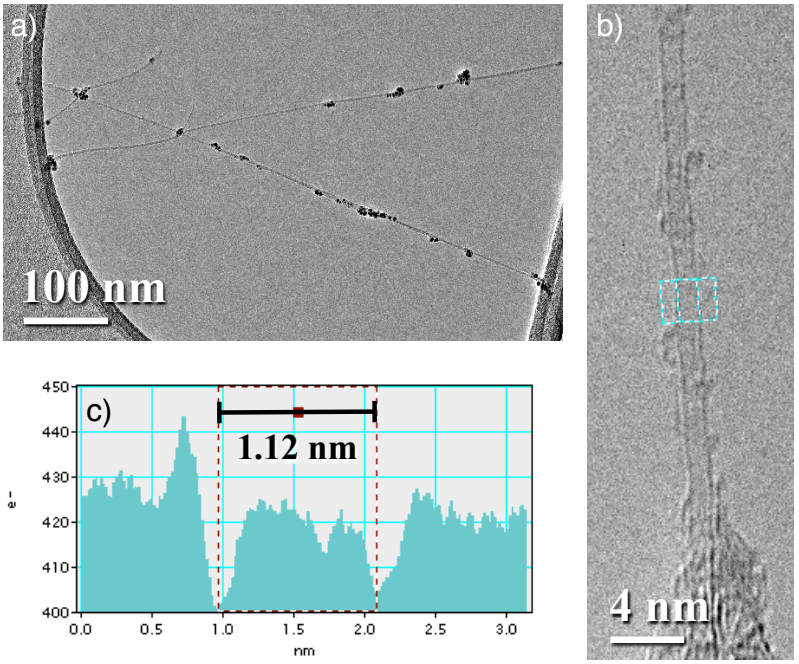

Figure 3.5 TEM micrographs of SWCNTs synthesized in the HWG reactor with 200 ppm NH_3. a) An overview image showing several bundles and some catalyst particles; b) a high-resolution image showing an individual SWCNT; c) a line profile of the marked area in b), used to determine the diameter.

3.1.3. Optical properties

3.1.3.1. Ferrocene reactor

In Publication I, properties of the produced SWCNTs were assessed by Raman measurements of samples collected on Millipore filters, and optical absorption measurements of samples transferred onto glass plates. The optical absorption measurements for three samples synthesized at 880 °C with slightly different amounts of introduced CO_2 and NH_3 are shown in Figure 3.6. From the optical absorption spectra, the mean diameters of the produced tubes could be estimated to be 1.3, 1.8, and 1.4 nm for the 5000 ppm CO_2, 0 ppm NH_3; the 5000 CO_2, 500 ppm NH_3; and the 2500 ppm CO_2, 500 ppm NH_3 samples, respectively. Similar absorption measurements were also conducted for samples synthesized at 1060 °C, and the diameters of the nanotubes determined in the 0, 250 and 650 ppm NH_3 samples to be 1.5±0.2, 1.6±0.3 and 1.4±0.2 nm, respectively (Table 3.2). We note that the diameter of the 1060 °C, 0 ppm NH_3 was incorrect in Publication I, but corrected in Publication III and Table 3.2.

Table 3.1 shows the G/D ratios estimated from the Raman spectra by a rough peak height estimation after subtracting the backgrounds. At 1060 °C, there is a slight increase of the ratio with 250 ppm of NH_3; note however that synthesis yield is much lower than without added ammonia. At 880 °C, although the yield of synthesis is lower with 500 ppm of NH_3, the quality of the produced material is higher, as shown by the increased G/D ratio with 5000 ppm of CO_2. Note also that the combination of good yield and highest G/D ratio is obtained with added NH_3; even though the yield with just 5000 ppm of CO_2 is higher, the quality of the product is significantly lower.

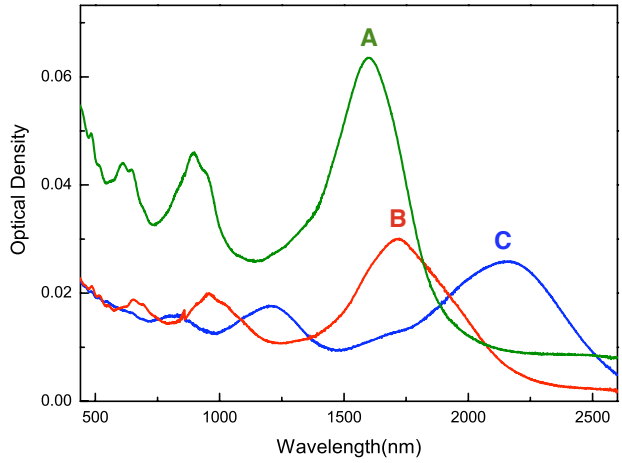

Figure 3.6 OAS of samples synthesized in the ferrocene reactor at 880 °C with **A** 5000 ppm of CO_2 and no NH_3; **B** 2500 ppm CO_2 and 500 ppm of NH_3; and **C** 5000 ppm CO_2 and 500 ppm NH_3. The indicated peaks correspond to the E_{11} transition.

In Publication III, multi-frequency Raman spectra were recorded for samples synthesized at 1060 °C with 0, 250 and 650 ppm NH_3. Figure 3.7 contains the most representative features that serve as a fingerprint of SWCNTs [18]. Figure 3.7a shows the disorder-induced Raman peak (D) and the G band, features which are observed in various carbon systems, but which are specifically related to SWCNTs here.

Regardless the excitation wavelength, the D to G intensity ratio increases only slightly with the increase of the amount of ammonia used during the synthesis process. The radial breathing modes (RBMs) were thoroughly recorded with various laser lines (c and d). The peak positions and intensities in the RBM region provide an idea of the diameters corresponding to nanotubes in resonance with the specific excitation used. These are in general agreement with the OAS results.

The G' band recorded with the 488 nm excitation is shown in Figure 3.7b. Changes of the G' band have been suggested as a signature of doping in SWCNTs [94]. We observe in Figure 3.7b a downshift of 1.4 cm^{-1} at the center of the maximum of the G´ from the first sample synthesized with ammonia with respect to the pristine material. The additional shift of ~2 cm^{-1} in the upper spectrum could be related to a higher doping level. However, given the slightly different morphology and changing diameter distribution of the nanotube material, we cannot attribute the additional G´ shift nor the differences in the RBMs of the samples to an increasing doping level.

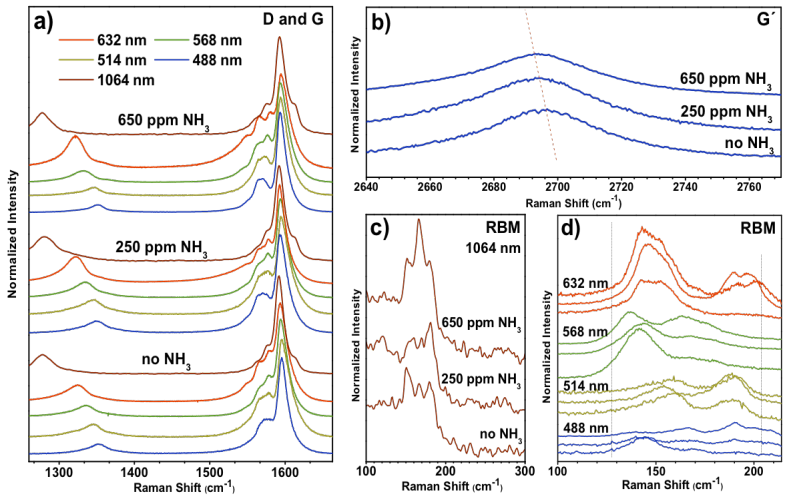

Figure 3.7 Raman spectra recorded with a Dilor xy triple monochromator spectrometer for the 488, 514, 568 and 632 nm excitation wavelengths and a Bruker Fourier transform (FT)–Raman spectrometer for the 1064 nm excitation, measured for samples synthesized in the ferrocene reactor at 1000 °C with 0, 250, and 650 ppm NH_3.

3.1.3.2. HWG reactor

As shown in Figure 3.8, the absorption peaks of the HWG samples shift to higher energy when N precursor is introduced, implying a decrease in the diameter of the SWCNTs. The OAS of samples synthesized with 200 and 300 ppm NH_3 present quite similar profiles, showing narrower peak widths than the one collected with 100 ppm NH_3. Following the OAS analysis method [151], we evaluated the mean diameters (Equation 3.1) of the nanotubes in the 0, 100, 200 and 300 ppm NH_3 samples to be 1.4±0.3, 1.2±0.3, 1.1±0.2 and 1.1±0.2 nm, respectively. Similar findings of a decrease in diameter with increasing N precursor amount have been reported before [88-90]. Practically no tubes were produced with more than 300 ppm NH_3. Note that the films collected with 200 and 300 ppm NH_3 were significantly thinner, as can be seen from their transparency values (Table 3.2).

Since the OAS method has been validated only for undoped tubes [151], we compared the diameter distribution of the 200 ppm NH_3 sample to the diameters of 56 individual SWCNTs in the 200 ppm NH_3 sample measured by HR-TEM (Figure 3.5). The diameter distributions obtained by OAS and TEM are shown in Figure 3.9. Not only are the mean diameters and variances equal, even the shape of the distribution matches remarkably well. The contribution of diameters around 2.5 nm in the OAS distribution (Fig. 3.9a) is a known artifact of the fitting procedure (due to optical transitions of large diameter metallic tubes overlapping around 1.2 eV with those of smaller diameter semiconducting ones abundant in the sample) and is not physically relevant.

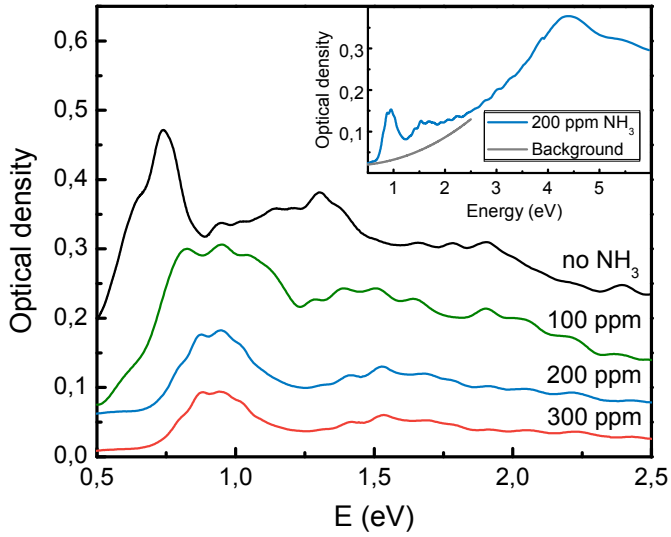

Figure 3.8 OAS of HWG samples synthesized with 0, 100, 200 and 300 ppm NH_3. The backgrounds have been subtracted (following Ref. [151]) and the spectra offset for clarity. The inset shows the raw spectrum for the 200 ppm NH_3 sample in the range of 0.5 to 6 eV, along with the background.

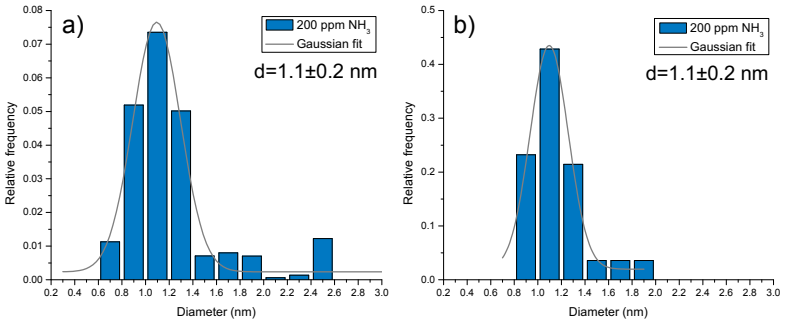

Figure 3.9 Diameter distributions of SWCNTs synthesized in the HWG reactor with 200 ppm NH_3, determined independently by a) analysis of the optical absorption spectrum recorded from a thin film sample (Figure 3.8) and b) TEM observations of 56 individual tubes (Figure 3.5).

Raman spectra were recorded for samples synthesized with 0, 100, 200 and 300 ppm NH_3 using a 632.81 nm (1.96 eV) excitation. Figure 3.10 contains the features characteristic of SWCNTs [18]. The left panel (3.10a) shows the radial breathing modes (RBM). The lowering of the left side peak supports the conclusion of decreasing nanotube diameter with increasing NH_3 already demonstrated by OAS and TEM analysis. The middle panel (3.10b) shows the disorder-induced Raman peak (D) and the G band. Interestingly, there is no increase of the D band intensity with increasing nitrogen precursor amount.

The G' (2D) band is shown in Fig. 3.10c. Although further studies are required on this topic, we note that there is a downshift of the main peak of the G' band of $\Delta\omega_{G'} \approx$ -15 cm^{-1} compared to the undoped material in all samples synthesized with NH_3. However, some shift would also be expected with changing nanotube diameter. To roughly estimate this effect for the single excitation used, we can use the relation [173]

$$\omega_{G'} = C_1 - C_2 / d \qquad (3.3)$$

with [27] C_1 = 2642.8 cm^{-1} (for the 1.96 eV laser used) and C_2 = 35.4 cm^{-1} nm. Inspection of the identical RBM features of the 0 and 100 ppm NH_3 samples, with a G' shift of almost -15 cm^{-1}, suggests that changes Raman resonant nanotubes' diameters cannot explain the changes in the G' band.

However, since the resonance window of the G' is broader than that of the RBM, it is more relevant to look at changes in the entire diameter distribution. Using the mean diameters determined from the OAS and Equation 3.3, a shift of only about 6 cm^{-1} would be expected with a decrease in diameter from 1.4 to 1.1 nm. This is not enough to explain the observed shift. Additional spectroscopic studies are required to make conclusions about using the G' signal for inspecting bulk samples of doped nanotubes.

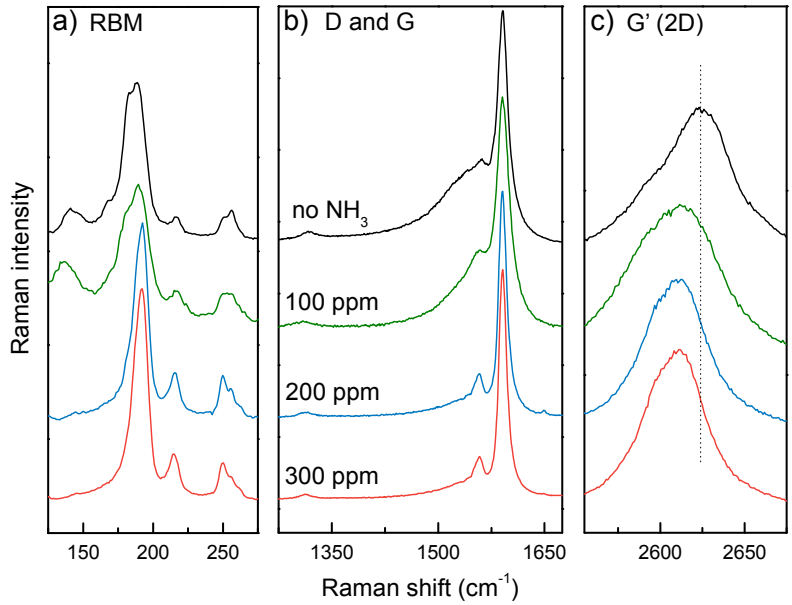

Figure 3.10 Raman spectra recorded with a 632.81 nm excitation from samples synthesized in the HWG reactor with 0, 100, 200 and 300 ppm NH_3. From left to right the RBM, D and G, and G' regions of the Raman response are shown.

3.1.4. Nitrogen incorporation

3.1.4.1. Ferrocene reactor

Figure 3.14b displays an EEL spectrum (C– and N–K edges), which is a sum of five EEL spectra with an acquisition time of 20 s each, recorded on the marked area shown in the bright field micrograph (Figure 3.14a) of a bundle of N-SWCNTs synthesized in the ferrocene reactor at 1000 °C with 625 ppm NH_3. The energy loss near-edge feature (ELNES) of the C–K edge consists of a π* peak at ~285 eV and a σ* band starting at ~292 eV. These signatures are typical for the sp^2 hybridization of the C atoms in a graphitic network, and indicate that the SWCNTs are well crystallized.

Concerning the N–K edge shown as inset of Figure 3.14b, we observe a peak at ~398 eV that could be assigned to pyridine-like configuration, and in some cases, also a peak at ~ 401 eV, which is assigned to a graphitic environment [56, 70, 97, 109, 158]. Furthermore, the incorporation of nitrogen into the carbon network was found to be inhomogeneous, ranging from 0 to ~3 at. % in different spots and different bundles. The mean nitrogen content is estimated to lie around ~1.7 at. %. This value is close to the one found on N-SWCNTs synthesized via the laser vaporization technique [109].

We must note here that since the samples were not purified, the N–K edge signal in EELS can contain some contribution from nitrogen that is not bonded to the SWCNT walls. This means that the nitrogen content measured by EELS should be taken as a fairly good approximation, keeping in mind that other nitrogen compounds can be present within the bundles or inside the tubes.

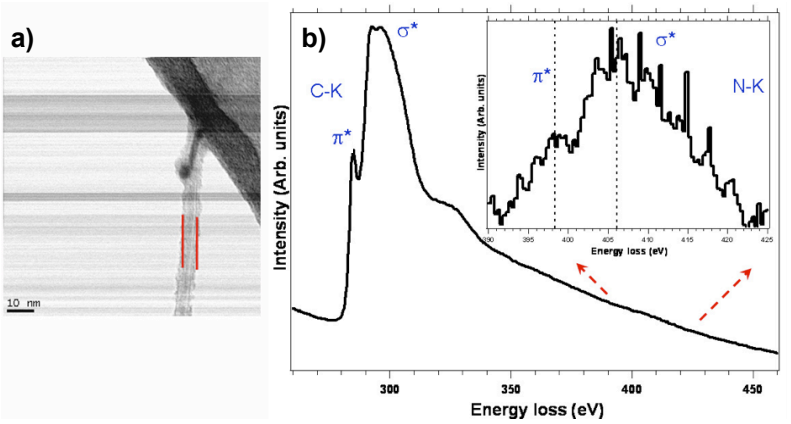

Figure 3.14 a) A bright field micrograph of a bundle of N-SWCNTs synthesized in the ferrocene reactor at 1000 °C with 650 ppm NH_3 b) a sum of 5 EEL spectra (C– and N–K edges) with an acquisition time of 20 s each recorded from the marked area in a). The inset of a) shows a magnification of the N–K edge after background subtraction.

3.1.4.2. HWG

Figure 3.15 displays an EEL spectrum (C– and N–K edges), which is a sum of four EEL spectra with an acquisition time of 2 s each, recorded on the marked area of the high angle annular dark field micrograph (Figure 3.15b) of a bundle of N-SWCNTs synthesized in the HWG reactor at 890 °C with 200 ppm NH_3. As in the ferrocene reactor sample (Figure 3.14), the energy loss near-edge feature (ELNES) of the C–K edge consists of a π* peak at ~285 eV and a prominent σ* band starting at ~292 eV. These signatures are typical for the sp^2 hybridization of the C atoms in a graphitic network; however, the lineshape seems to be less ideal in the HWG samples.

From the N–K edge, we calculated that the total nitrogen concentration in different bundles of the 100 ppm NH_3 sample ranged from 0.3 to 2.0 at. %, with an average of about 1.2 at. %. A similar analysis for the 200 ppm NH_3 sample gave an estimate of 1.7 at. % (Figure 3.15a inset). The 300 ppm NH_3 sample was not stable enough under the 100 kV STEM electron beam to measure EELS.

The HWG film samples were also measured by XPS. The spectral deconvolution for the nitrogen core level signal (N1s) contained approximately equal contributions of 398.6 and 400.5 eV binding energies, as has been described previously [82, 83]. The total nitrogen concentration in the films was determined to be 0.2 at. % in the 100 ppm NH_3 sample, 0.7 at. % in the 200 ppm NH_3 sample, and 1.1 at. % in the 300 ppm NH_3 sample. Only in the case of the 300 ppm NH_3 sample, a slight upshift was detected in the C1s line, suggesting the formation of significant numbers of defective sites, as reported in other studies related to N-SWCNTs [82, 83]. This would explain the observed instability of this sample in EELS.

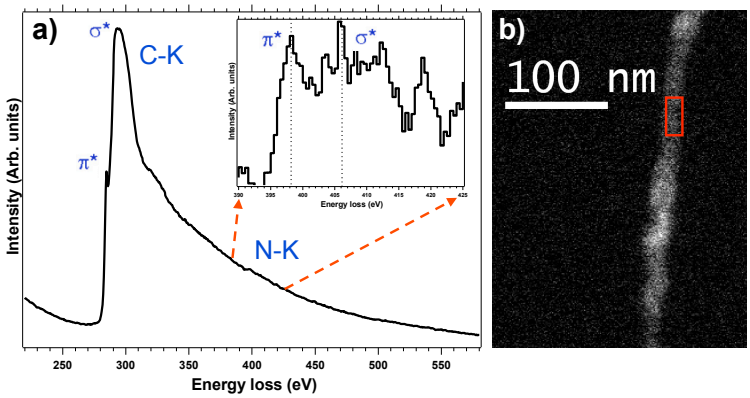

Figure 3.15 a) A sum of 4 EEL spectra (C– and N–K edges) with an acquisition time of 2 s each, recorded on the marked area shown in the b) high angle annular dark field micrograph of a bundle of N-SWCNTs synthesized in the HWG reactor at with 200 ppm NH_3. The inset of a) shows a magnification of the N–K edge after background subtraction.

3.1.4.3. STM/STS measurements

The doped HWG samples were also studied by STM/STS measurements[1]. In contrast with previous samples of undoped tubes, several 'defects' were observed that could be the signatures of topological defects, but also could be the signature of nitrogen atoms or defective areas including nitrogen. An example of the unpublished experimental results is shown in Figure 3.16. The atomic resolution images and local spectra evidence the appearance of a specific donor state at the defect site. In this particular case, a good match is obtained with the (unpublished) calculated[2] local density of states of an N substituted (10,4) nanotube. This finding represents the first clear local identification of a substitutional – or indeed any – nitrogen site in N-SWCNTs. However, we note that as in previous N-SWCNT samples from laser ablation [78], in most cases the observed defect sites show extended perturbations of the electronic structure, and do not seem to correspond to any simple, easily identifiable configuration.

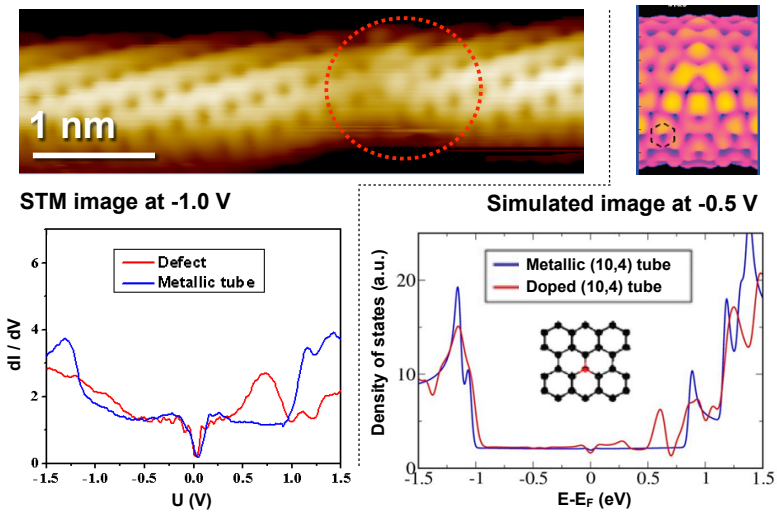

Figure 3.16 Unpublished data. (Left) STM scan and local spectra measured by STS on a defective metallic tube synthesized in the HWG reactor with 300 ppm NH_3. The blue spectrum measured far from the defect displays the well-known characteristics of a metallic tube (van Hove singularities around +1 V and -1 V and a pseudo-gap around 0 V). The red spectrum measured on the defect shows a specific peak around 0.7 V. Measurements courtesy of Jerôme Lagoute. (Right) Simulated STM image (from [68]) and density of states of a (10,4) tube with a substitutional N atom, presenting a similar signature as in the experiments. Simulations courtesy of Luc Henrard.

[1] By the STM team of Jerôme Lagoute at the Laboratoire Matériaux et Phénomènes Quantiques, Université Paris Diderot and CNRS in Paris, France.

[2] By Luc Henrard at the Laboratoire de Physique du Solide, Facultés Universitaires Notre-Dame de la Paix in Namur, Belgium.

3.1.5. Sheet resistances

3.1.5.1. Network simulations

Figure 3.11 shows an example of a line segment network generated by our resistor network code (Section 2.4.1). The network conductance σ exhibits a linear dependence on the average line segment length ⟨l⟩ over the experimentally relevant range of 1 to 4 μm. Random lognormal length distributions

$$f(x;\mu,s) = \frac{1}{xs\sqrt{2\pi}} e^{-(\ln x-\mu)^2/2s^2}, \quad x > 0, \tag{3.2}$$

were used for the line segments, where μ (the location parameter) and s (the scale parameter) are the mean and standard deviation of the natural logarithm of the dimensionless length x, respectively. The values for the standard deviations were calculated from the experimental bundle length distributions (Table 3.2). The nonzero intercept of the x-axis is to be expected based on percolation arguments. The network connectivity, defined as the average amount of contacts per line segment, was likewise found to depend on ⟨l⟩ linearly, suggesting that network conductance is directly determined by the connectivity.

In addition to line segments, we also ran simulations with rectangles of finite widths at fixed length. Even a decrease of aspect ratio from 1000 to 100 resulted in an increase of connectivity of only 3.5%. Thus a decrease of bundle diameter from 6.1 to 3.7 nm should not cause discernible changes in the connectivity itself.

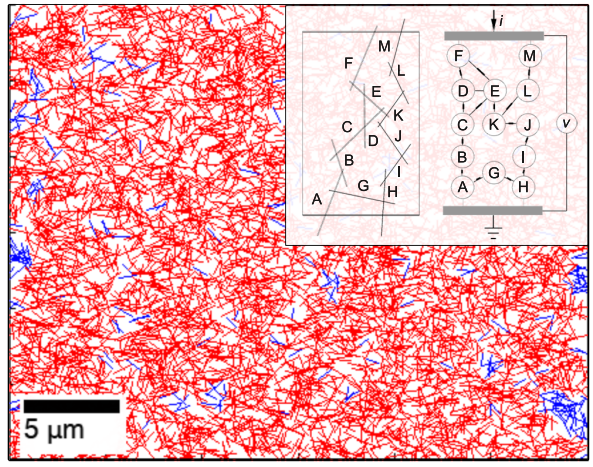

Figure 3.11 A simulated bundle network consisting of randomly oriented line segments. The red and blue colors denote segments that form conducting pathways and segments that do not, respectively. The inset displays how the resistor network is formed out of line segments and their intersections.

3.1.5.2. Sheet resistance analysis

The sheet resistance and transmittance values for undoped SWCNT films (Table 3.3) were compared to the doped SWCNT films synthesized with 100–300 ppm NH_3 (Table 3.2). As the undoped reference films, two sets of samples were used. The first were films of varying thickness synthesized previously with the ferrocene reactor (FC) [118], with bundle length distributions of 1.3±0.8 μm (upwards blue triangles in Figure 3.12) as well as 3.3±1.4 μm (downwards dark blue triangles), and bundle diameter distributions of 8.3±3.5 nm and 7.8±2.7 nm, respectively. Additionally, 4 undoped films synthesized with the HWG reactor were used (purple circles), corresponding to the 0 ppm NH_3 sample.

The figures of merit of the undoped sample sets calculated from fits of Equation 2.4 to the data in Figure 3.12 are plotted in Figure 3.13, along with the values for each doped sample (Table 3.2). Thus the undoped sample data points (blue diamonds and purple circles) are derived from several films (Figure 3.12 and Table 3.3), while the doped data points correspond simply to the samples in Table 3.2. Figure 3.13 shows that the figures of merit of the doped samples are lower compared to those of undoped sample sets with similar length distributions collected from the ferrocene reactor (blue dotted line) with a deficit of 68% for the 100 and 200 ppm samples. Furthermore, if we compare the values of the doped films to the undoped HWG data (dotted purple line), the deficit is 85–86%. For both kinds of films, the intercept of the x-axis is around 0.5 μm, which might indicate the onset of the percolation threshold, in agreement with the simulations.

Table 3.3. Properties of undoped SWCNT films synthesized with the HWG (this work, HWG 3.1 μm long bundles) and the ferrocene (FC, 1.3 and 3.3 μm bundles [118]) reactors. The columns show: sample name, 4-point sheet resistance, and transmittance of 550 nm light.

Sample	4-point R (kΩ/□)	T @ 550 nm (%)
FC 1.3 μm	0,384	6
FC 1.3 μm	2,26	53
FC 1.3 μm	2,94	74
FC 1.3 μm	9,94	86
FC 1.3 μm	40,7	96
FC 3.3 μm	0,203	16
FC 3.3 μm	0,52	59
FC 3.3 μm	0,628	65
FC 3.3 μm	1,31	82
FC 3.3 μm	2,44	88
FC 3.3 μm	3,16	93
FC 3.3 μm	7,68	97

Sample	4-point R (kΩ/□)	T @ 550 nm (%)
HWG 3.1 μm	0,2	43
HWG 3.1 μm	0,208	46,4
HWG 3.1 μm	1,58	86,4
HWG 3.1 μm	1,8	71,8
HWG 3.1 μm	4,52	95

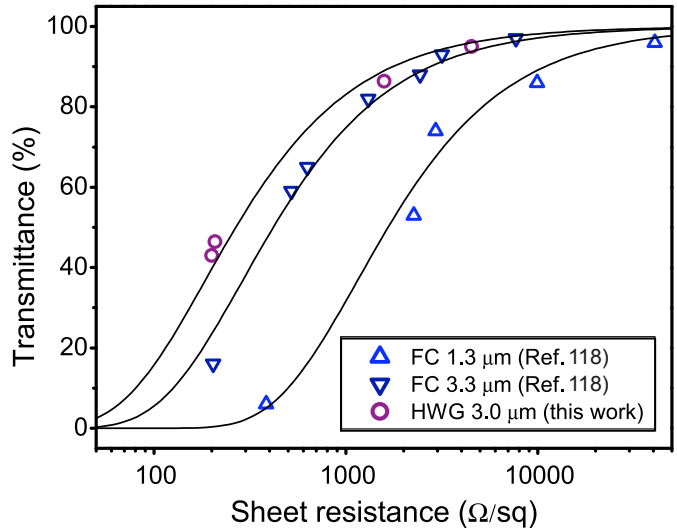

Figure 3.12 Sheet resistance versus transmittance at 550 nm for undoped sample sets from the ferrocene reactor with two bundle length distributions (FC, Ref. [118]) and the hot wire generator reactor (HWG, this work). Solid lines show fits based on Equation 2.4, with figure of merit K as the fitting parameter.

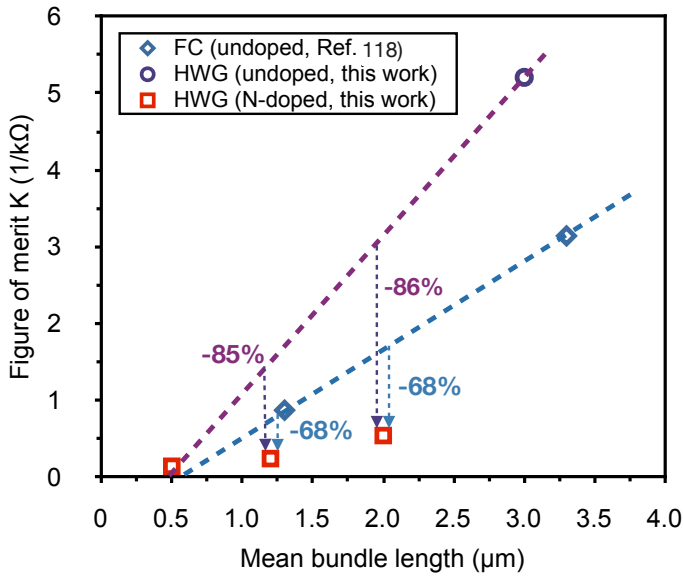

Figure 3.13 Figures of merit versus mean bundle lengths for undoped sample sets (Figure 3.12 and Table 3.3) from the ferrocene (blue diamonds, Ref. [118]) and HWG (purple circles) reactors, and nitrogen-doped films from the HWG reactor (red squares, Table 3.2). The purple thick dotted line is a linear fit to the undoped and 300 ppm NH_3 doped HWG sample, while the blue thick dotted line is a linear fit to the undoped ferrocene samples. The vertical dotted lines represent the deficits of the figures of merit of the doped films compared to the ferrocene data (blue) and the undoped HWG data (purple).

3.2. Growth mechanism

3.2.1. Gas measurements

In the temperatures relevant for SWCNT synthesis using CO, CO_2 and H_2, several reactions are important. The main source of carbon for CNT growth is the Boudouard reaction (Equation 1.4). Because H_2 is present in the reactor (either from the H_2/Ar gas in the HWG, or from ferrocene and/or NH_3 decomposition), another reaction, CO hydrogenation, leading to the carbon release could occur:

$$CO\,(g) + H_2\,(g) \rightleftharpoons C\,(s) + H_2O\,(g). \tag{3.4}$$

The water gas-shift reaction can also play a role in the balance of gaseous products. When ammonia is present in the reactor and reacts catalytically on the iron nanoparticles, atomic nitrogen and hydrogen can be released. From these H_2 and N_2 can form, and since carbon is most likely already present, a possible further reaction is the formation of hydrogen cyanide ($H-C\equiv N$),

$$CN\,(ads.) + H\,(ads.) \rightleftharpoons HCN\,(g). \tag{3.5}$$

FTIR can be used to measure the amounts of CO, CO_2, H_2O, HCN and NH_3 by analyzing the spectra using a library of known analytes. Figure 3.14 shows an example FTIR spectrum from Publication V; note that CH_4 or any other hydrocarbons were not observed in any of the other publications.

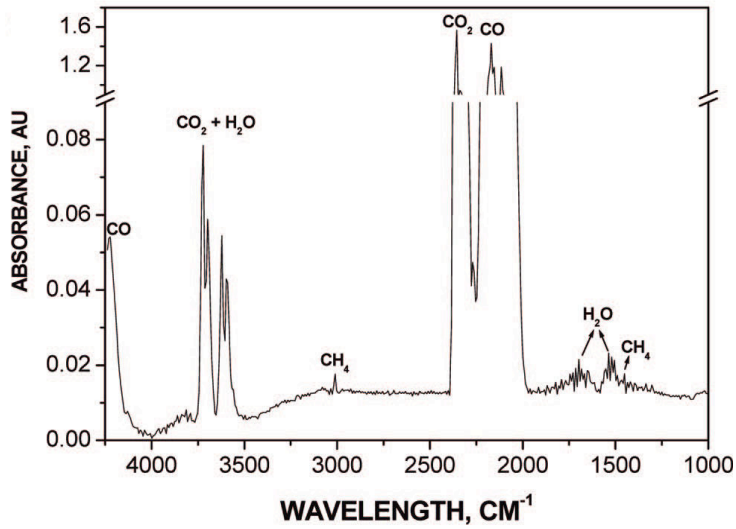

Figure 3.14 FTIR spectrum of the gas mix present in the reactor in Publication V. The characteristic peaks for the main analytes are indicated.

3.2.1.1. Carbon chemistry

In Publication VI, the CO disproportionation reaction was investigated in a horizontal quartz tube at a heating rate of 5 °C/min. A silica substrate with 2.8±0.6 nm sized iron particles deposited from the HWG reactor was placed inside the tube. The CO flow rate was maintained at 8.3 cm^3/min. The concentration of the gaseous product (CO_2) was monitored on-line by FTIR. The region of CO_2 concentration increase from about 350 °C to about 580 °C is the kinetic region, where the rate of the CO disproportionation reaction is significant. At temperatures above 600 °C, the reaction is limited thermodynamically. Since the disproportionation rate is proportional to the concentration of CO_2, we assume that the activation energy of the reaction can be found using an Arrhenius dependence

$$X(CO_2)=k_0 \exp(-E_a/RT), \quad (3.6)$$

where $X(CO_2)$ is the carbon dioxide mole fraction, k_0 the kinetic prefactor, R the gas constant, and T the temperature in Kelvin. Plotting the kinetic region in the coordinates of ln $X(CO_2)$ versus 1/T, one gets a remarkably low activation energy of E_a = 31.6 kJ/mol = 0.33 eV as the barrier for the CO disproportionation reaction (Figure 3.17) on these very small iron nanoparticles.

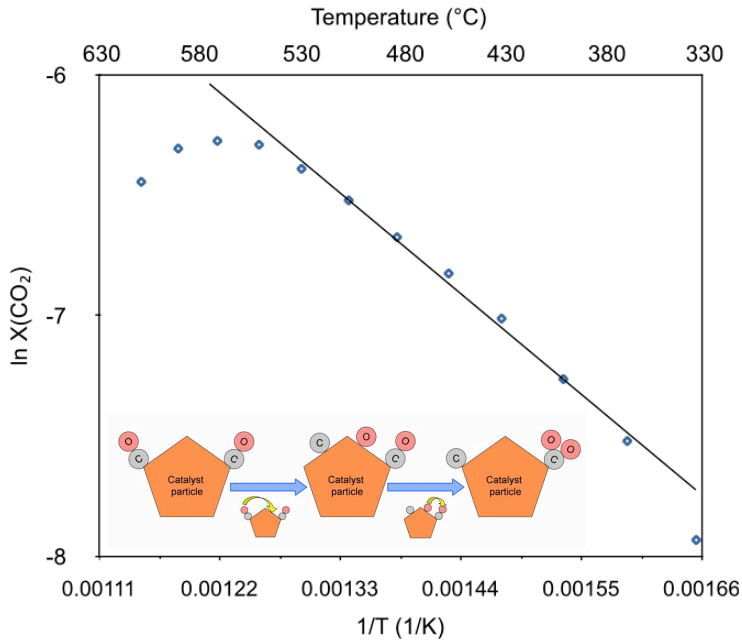

Figure 3.17 Kinetic region of CO disproportionation reaction fitted with a line (Arrhenius plot). The inset shows a schematic mechanism for the reaction.

3.2.1.2. Nitrogen chemistry

In Publication I, the ferrocene reactor outlet gases were measured by FTIR to investigate the chemistry taking place inside the reactor. Introducing 625 ppm of NH_3 at 1060 °C increased the measured amount of CO_2 from 290 to 410 ppm. Note that some CO_2 is always produced on the reactor walls. Furthermore, 220 ppm of hydrogen cyanide (HCN) was detected when NH_3 was introduced into the reactor. At 880 °C, the effect of NH_3 was less pronounced, but the analyzable compounds remained the same.

In Publication VII, the experimental reaction barrier for NH_3 decomposition was measured using FTIR and mass spectroscopy in tandem. Gas-phase thermal decomposition of NH_3 over iron nanoparticles deposited on the walls of the HWG reactor used for N-SWCNT synthesis was investigated in the temperature range of 590–1090 °C. Concentrations of ammonia and water as a function of reactor maximum wall temperature were measured using FTIR, and hydrogen and nitrogen using RGA. The inlet gas consisted of 800 cm^3/min of Ar along with 500 ppm of NH_3.

RGA mass spectra must be interpreted properly since they can be ambiguous in certain cases, such as when two different molecules exhibit the same mass. Knowledge of how different molecules with the same mass would dissociate into smaller fragments of different mass-to-charge ratios allows absolute identification of any gas. However for the simple molecules H_2 (atomic mass 2) and N_2 (atomic mass 28, but also a peak at 14 by atomic N^+ and doubly ionized N_2^+), direct identification is quite easy.

Three regions for NH_3 decomposition can be discerned in Figure 3.18: (I) a low temperature region (590–740 °C), where NH_3 decomposition is fast and H_2O is the main product. Oxygen concentration in the reactor from the Ar carrier gas impurities and environmental leakage was measured to be about 150 ppm; (II) an intermediate region (740–940 °C), where any additional decomposition of NH_3 is into N_2 and H_2. We believe this corresponds to the catalytic decomposition of NH_3 modeled in the simulations; (III) a high temperature region (990–1090 °C), possibly relevant for NH_3 self-decomposition in the gas phase. The mole fraction of NH_3 can be plotted in an Arrhenius plot, showing the same regions (Figure 3.19). Linear least squares fits yield slopes of 28867±241 K, 4978±190 K and 1932±134 K, for the high, middle and low temperature region. These correspond to energies of -2.49±0.02 eV, -0.43±0.02 eV and -0.17±0.01 eV. Note that because the decrease of the NH_3 mole fraction is relevant for the decomposition reaction, the actual barriers come out with the signs reversed.

Measurements for HCN formation were performed using 500 ppm of NH_3 in a flow of 400 cm^3/min CO. Analysis of the corresponding Arrhenius plot yields an activation energy of 1.35 eV.

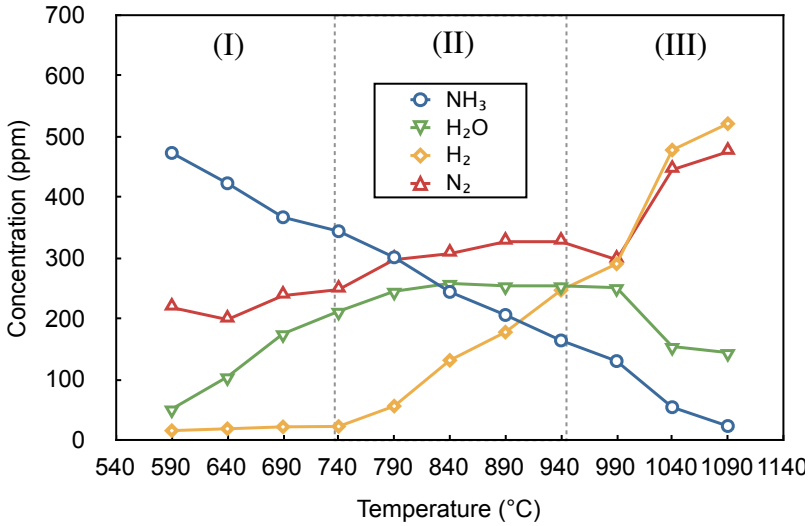

Figure 3.18 Concentrations of ammonia and water measured using FTIR, and hydrogen and nitrogen measured using mass spectrometry, as a function of reactor maximum wall temperature.

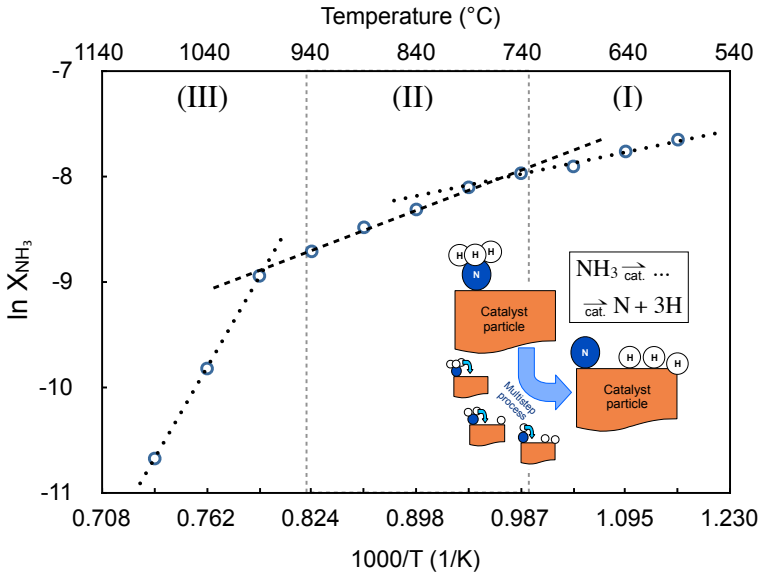

Figure 3.19 Arrhenius plot of the mole fraction of NH_3, showing three distinct temperature regions. The dashed and dotted lines are linear fits to the data. The inset shows a schematic illustration of the multi-step reaction mechanism.

3.2.2. Computational studies

As shown above, the synthesis of N-SWCNTs is feasible using CO and NH_3, with iron as catalyst. This combination of two small precursor molecules, each with only a single C or N atom, presents the simplest possible chemistry. Furthermore, since the particles interact with precursor molecules in the gas phase, both the tip and base growth mechanisms are equivalent. To further study the mechanism of N-SWCNT growth in the HWG, first principles calculations were performed in order to understand the chemistry of the precursor reactions on a model Fe_{55} catalyst cluster in Publications VI and VII. The carbon calculations (Publication VI) were based on earlier work by Lanzani et al. [168, 169], but were performed with the GPAW code [166] instead of VASP.

As a first step, we obtained information about the stability of CO, NH_3 and their fragments on the Fe_{55} cluster (comparable to earlier VASP results [167, 168]). Thus as the second step of the study we considered the reaction barriers on the surface. Climbing-image nudged elastic band (CI-NEB) [171, 174] method was used for the determination of the reaction barriers.

We believe that the adsorbed CO and NH_3 first dissociate into surface atomic C and N,

$$CO_{ads} \rightarrow C_{ads} + O_{ads} \tag{3.7}$$

and

$$NH_{3ads} \rightarrow N_{ads} + 3H_{ads}\,. \tag{3.8}$$

Since there is always more carbon than nitrogen available, in a simplistic picture, the more numerous carbon atoms then react with each other and the nitrogen atoms to form the hexagonal carbon lattice with nitrogen dopants,

$$C_{ads} + C_{ads} \rightarrow C\text{-}C_{ads} \tag{3.9}$$

and

$$C_{ads} + N_{ads} \rightarrow C\text{-}N_{ads}\,, \tag{3.10}$$

while the remaining O atom reacts with additional CO to form CO_2 according to the well-known Boudouard reaction [36, 169]. The reactions above seem simple, but in reality the catalyst surface has a high coverage of the molecular precursors and their fragments, so there are complicated atom–atom interactions. By necessity, we concentrated our attention on the simplest CO and NH_3 reactivity.

3.2.2.1. Carbon chemistry

In Publication VI, DFT calculations were used to study CO and atomic C adsorption on the icosahedral Fe_{55} cluster. The geometry optimization was started from the high symmetry adsorption sites of one the 20 triangular face of the cluster. The high symmetry adsorption sites are the top site, octahedral hollow site and tetrahedral bridge sites. The bridge and top site can be in-plane on the cluster face or on its edge/vertices. For CO, interaction geometries presenting the molecular bond either coplanar (=) or perpendicular (≟) to the cluster surface were considered. When the CO molecule is placed flat on the cluster, during the geometry optimizations oxygen atoms are not bonding to the surface and the molecule flips up.

Perpendicular adsorption is not favorable when oxygen is toward the surface (≟ OC). During the relaxations with the molecule adsorbed through the carbon (≟ CO), it spontaneously moves, migrating to the bridge and hollow sites of the surface (see supporting information of Publication VII for details). To describe the energetics of the adsorbed species on the surface, the interaction energy term (I.E.) is defined as

$$\text{I.E.} = E_{Fe_{55}/CO} - (E_{Fe_{55}} + E_{CO}), \quad (1)$$

where $E_{Fe55/CO}$ is the total energy of the adsorbate-substrate system, E_{Fe55} of the Fe_{55} cluster, and E_{CO} of the free CO molecule. The I.E. term thus describes the strength of the adsorbate-substrate interaction.

Based on CO adsorption and C + O co-adsorption data, a dissociation path for CO was mapped out with NEB [174]. The smallest activation energy (0.50 eV) was obtained starting from the optimal adsorption geometry with the CO molecule perpendicular to the cluster (≟ CO). The reaction is exothermic by 0.12 eV (Figure 3.20). Note that this value for the CO barrier in Publication VII differs from the value in Publication VI (0.63 eV) due to the use of a different geometry optimizer ('Fire' [175], instead of 'LBFGS'). The lower value should be considered to be more correct.

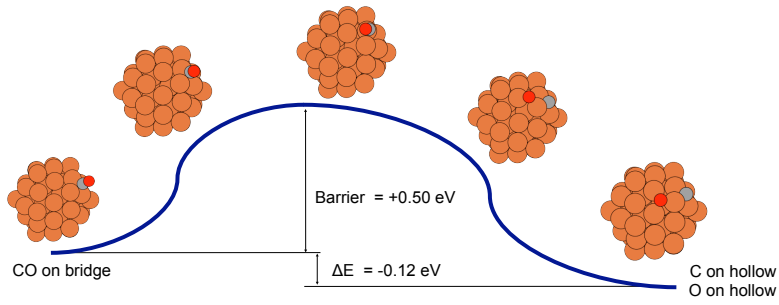

Figure 3.20 Calculated minimum energy paths for CO dissociation on a step of the Fe_{55} model cluster (Fe, brown; C, grey; O, red).

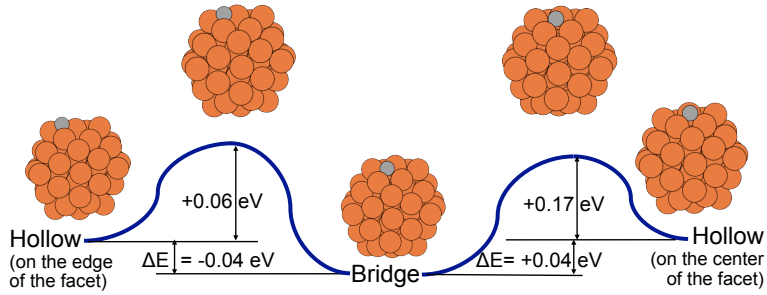

Figure 3.21 Proposed reaction paths for the mobility of atomic C on the Fe_{55} model cluster. The atomic C has a possible metastable state.

Once atomic carbon is present on the cluster, it is vital to study its mobility as a preliminary stage of nanotube nucleation. To examine the role of this step in the overall process, the adsorption geometry of atomic carbon was studied. The most stable geometry on and below the surface together with the calculated energetic path connecting them is depicted in Figure 3.21. The NEB method was used to study the mobility of carbon, and a barrier of 0.17 eV was found.

This behavior changes when possible reaction paths for the inclusion of atomic carbon under the surface of the Fe_{55} model cluster are considered. The obtained formation energy for a carbide-like structure is -0.50 eV with an elementary rearrangement of atoms and molecules on the surface. Further inclusion of the atomic carbon in the cluster (ΔE = +0.43 eV) requires overcoming a barrier of 0.51 eV.

The mechanism for CO oxidation involves a reaction of the CO molecule and an adsorbed oxygen atom. The structures of all transition states and intermediates are depicted in Figure 3.22 together with the energy profile. The obtained formation energy is +0.62 eV with a barrier of +1.04 eV. Considering that the particle morphology and reaction conditions are different, the calculated data are in reasonable agreement with experimental results of Li et al. [176] and the authors [169].

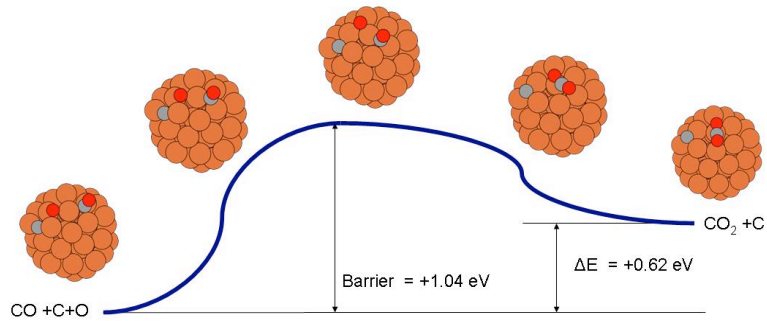

Figure 3.22 Calculated minimum energy paths for CO_2 formation of the Fe_{55} model cluster (Fe, brown; C, grey; O, red).

3.2.2.2. Nitrogen chemistry

Nitrogen chemistry was studied in Publication VII. The stability of NH_3 on the cluster was first considered. The molecule was set on the vertices, on the edge and on the centre of the icosahedral face of the cluster. For every adsorption site, the possible effect of the orientation was considered, though only the interaction N–Fe was favorable, and only the top sites were stable (-0.73 eV < B.E.(NH_3) < -0.60 eV).

In order to study NH_3 dissociation with the CI-NEB method, we needed to know the preferred adsorption sites for NH_2, NH and N on the cluster. During relaxation, the NH_2 molecule spontaneously moves, migrating to the bridge sites on the facet of the surface (-3.10 eV < B.E.(NH_2) < -2.52 eV). The arrangement presenting the nitrogen tetrahedrally coordinated to two hydrogens and two irons atoms is clearly preferred. Similar behavior was observed considering the interaction of NH at the high symmetry adsorption site (-4.64 eV < B.E.(NH) < -3.18 eV). During geometry optimization, the fragment rearranges, moving to the hollow site, where N can easily interact with three metal atoms. Atomic nitrogen presents a similar behavior to carbon: the hollow sites on and below the surface are most stable.

Correspondingly, based on the NH_{3-x} + xH (x=0,1,2,3) co-adsorption data, a possible dissociation path for NH_3 was calculated with the NEB method. The obtained reaction energy is -0.32 eV/molecule with an overall barrier of 1.00 eV (Figure 3.23). The complete dissociation to atomic nitrogen and hydrogen involves three steps: (1) $NH_3 \rightarrow NH_2 + H$; (2) $NH_2 + H \rightarrow NH + 2H$; (3) $NH + 2H \rightarrow N + 3H$. The dissociation of the last hydrogen presents a significantly higher barrier than the first two steps.

The mobility of nitrogen of the cluster and the C–C/C–N bond forming reactions were studied as well. The mobility barrier for N is quite small (0.44 eV, Figure 3.24), but what is more remarkable, both the C–C and the C–N bond formation reactions were found to be barrierless and exothermic.

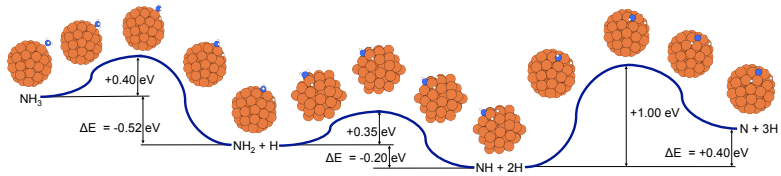

Figure 3.23 Calculated activation barriers and reaction energies for each step of NH_3 decomposition ($NH_3 \rightarrow NH_2 + H \rightarrow NH + 2H \rightarrow N + 3H$). Fe atoms are orange, N – blue, and H – white.

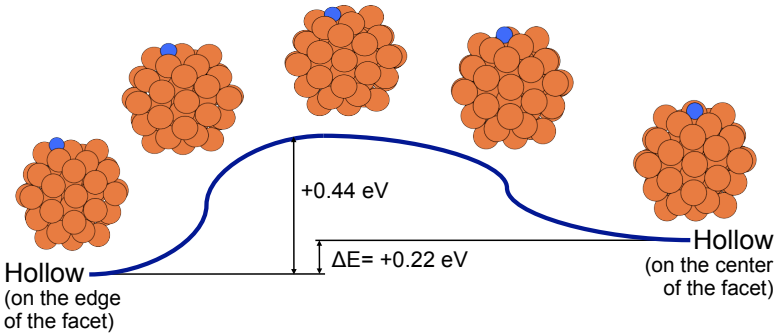

Figure 3.24 Proposed reaction paths for the mobility of atomic N on the Fe_{55} model cluster.

Since there is hydrogen present in the system from NH_3, the simplest possible further reaction for the adsorbed CN fragment is the formation of hydrogen cyanide (HCN). In the present context this is a parasite reaction, since the HCN molecule would take away one nitrogen atom otherwise available for doping the carbon network. Based on CN and H co-adsorption data, a possible formation path for HCN was calculated with the NEB method (Figure 3.25). The obtained reaction barrier is 1.65 eV, consistent with the measured barrier of 1.35 eV.

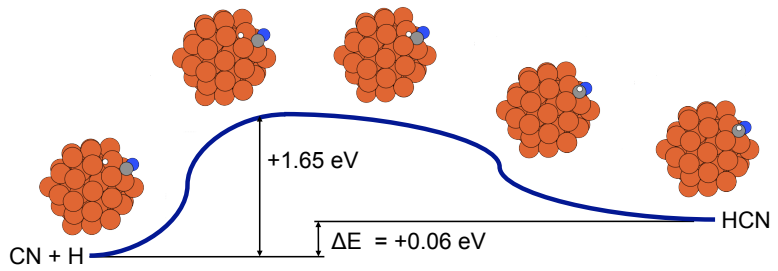

Figure 3.25 Proposed reaction path for HCN formation reaction on the Fe_{55} model cluster.

4. Discussion

4.1. Comparison of reactors

The introduction of NH_3 into either reactor enabled the synthesis of nitrogen-doped SWCNTs in a simple process. Ammonia is a volatile gas and likely breaks down catalytically on the iron clusters along with CO, providing free atomic nitrogen, which is incorporated into the growing nanotube structure. The uniformity and level of nitrogen doping seems to be somewhat variable according to EELS. We originally thought that this was due to the very low flow rate of NH_3 needed for successful synthesis, which was the minimum possible for the mass flow controller we used in the original experiments (Publications I and III). It was hoped that using a dilution system for NH_3 would improve the uniformity of the doping, but in light of the later HWG samples (Publication IV) there is little evidence for this. The reason for the non-uniformity remains unclear.

The introduction of NH_3 into the ferrocene reactor offers a possibility to shift the diameter distribution of the produced SWCNTs, as evidenced by the optical absorption measurements. As the diameters of SWCNTs synthesized by CVD are determined at the nucleation stage, and depend on the catalyst particle sizes, the shift in the diameter distribution to larger diameters may be due to the catalyst particle sizes at nucleation being correspondingly larger. The reactive NH_3 species might delay the nucleation until the catalyst particles have grown slightly larger than they would have without it. Another possibility that cannot be ruled out with the present experimental setup is the selective etching of small diameter SWCNTs, whose carbon network is more reactive.

Furthermore, considering the data in Table 3.1 we conclude that very small amounts of ammonia can be beneficial for producing high quality SWCNTs in the ferrocene system, particularly at lower temperatures. Even though there is a decrease in yield, at 880 °C the three-fold gain in the G/D ratio, which is thought to signal a significant increase in the quality of the produced SWCNTs. The effect appears similar to the role played by CO_2 in etching the produced tubes of amorphous carbon and defects. At 1060 °C ammonia may be too reactive, which can be understood to be due to the thermodynamics of the CO disproportionation reaction. The lower the temperature, the more etching agents can be added.

Considering the later HWG reactor samples, we do not observe an increase in the G/D ratio as in the lower temperature ferrocene reactor samples. Remarkably, nor do we observe a decrease, as would had been expected from the literature. However, it must be noted that co-products (amorphous carbon, encapsulated catalyst particles, etc) can contribute to these differences. Future experiments on purified samples will be helpful in addressing these issues.

Also, the effect ammonia has on the mean diameters of the SWCNTs produced seems to differ between the reactors. In the HWG samples (Publication IV), increasing amounts of NH_3 induce a decrease in the mean diameters of the produced N-SWCNTs. As stated above, this has been observed before in the literature [64, 65, 83]. This stands in contrast with the ferrocene reactor samples (Publications I and III), where there first seems to be an increase in the mean diameter, and only when the amount is increased further, a decrease. This might have something to do with the slightly different chemistry in the ferrocene reactor (catalyst particle formation method, lack of added H_2 in the system). The role of CO_2 seems to be important as well, as might be the fact that no dilution system was used for the early experiments in the ferrocene reactor. However, we do note that similar behavior has been observed in very recent unpublished samples from the ferrocene reactor using the dilution system.

Considering the optical absorption and Raman spectra of the HWG reactor 100 ppm NH_3 sample, they seem to be intermediate between the 0 and 200 ppm NH_3 spectra. By contrast, there is little change from the 200 to the 300 ppm NH_3 spectra, even though the bundles are getting shorter still (Table 3.2). Thus it seems that full modification of nanotube properties can be achieved already with 200 ppm, while 300 ppm affects the growth excessively. This is also seen in the EELS measurements, where the 300 ppm sample was unstable under the electron beam in EELS. It is remarkable how small amounts of ammonia have such a drastic effect on the synthesis. This may be a feature of the floating catalyst reactors, or the specific chemistry of CO and NH_3 on the very small iron nanoparticles.

4.2. Chirality-selective growth

It seems that the introduced NH_3 shifts not only the diameter distribution of the produced nanotubes, but also the chiral angle distribution. High chiral angle nanotubes are enriched compared to the pristine material (Publications II and III). It is an open question to discuss the role of NH_3 in growing SWCNTs with a narrow chirality distribution. However, as the yield in our process is also significantly lower when NH_3 is used, we can speculate that ammonia could act as a powerful etching agent, similar to CO_2 [36, 137], attacking the weaker C–C bonds of small chiral angle tubes [177, 178]. In the literature, chirality-enriched synthesis has often been reported to be related to the shape of supported catalyst particles [48, 50]. It is doubtful the same mechanism would apply to floating iron particles at this high temperatures. It is also worth noting that the opposite trend has been tentatively observed in single-walled boron nitride nanotubes, where zigzag and near to zigzag configurations seem to be preponderant [179].

The same etching effect could apply to nanotubes of smaller diameters due to their higher curvature [178], which would explain the slightly enlarged average nanotube diameter as NH_3 is introduced. Since the effect seems to be different in the HWG and ferrocene reactors, perhaps this is again related to slightly different catalyst particle formation mechanism and composition. The NH_3 etching action may take effect on the catalyst clusters already during nucleation, suppressing the growth of smaller chiral angle tubes that have a relatively larger number of dangling bonds on the growing edge of the hexagonal network. Etching effects could well elucidate the decreased yield and the decreased bundling of nanotubes observed with added NH_3. Firm conclusions, however, remain elusive.

Excessive amounts of NH_3 lead to a termination of nanotube synthesis. On the other hand, fine-tuning of the NH_3 concentration could conceivably enhance chiral angle selectivity. Furthermore, recently it was reported that the diameters of carbon nanotubes could be effectively tuned in a similar floating catalyst CVD process by introducing controlled amounts of CO_2 [151]. Therefore, in future work, we anticipate tunable selective growth of SWCNTs with preferred chiral structure by simultaneously regulating the amounts of NH_3 and CO_2 introduced into the reactor.

It further remains uncertain if nitrogen doping itself could be the cause of the changes in both the diameter and chiral angle distributions. We must note that theoretical calculations of N-SWCNTs have implied that nitrogen could destabilize armchair tubes [76] (see, however, also [56]). Also, it has been predicted that substitutional nitrogen dopants should favor zigzag configurations [180], perhaps supporting the observation of pyridinic N dopants in our samples by EELS. Despite these theoretical suggestions, as of now, the mechanism for the observed selectivity remains unknown.

4.3. Prospects for N-SWCNT electrodes

Our theoretical network model suggests that in a dense network (far from the percolation threshold, i.e. the minimum density where conducting paths are formed) of CNT bundles or similar conductors, in which the bundle–bundle contact resistances dominate, the network conductance scales linearly with the average bundle length. This result is in line with previous theoretical work and electronic measurements of CNT networks far above the percolation threshold [181], as well as data obtained from our undoped samples [118]. Further development of the theoretical model should endeavor to explicitly incorporate also the optical absorption and the effects of nanotube and bundle diameters, among other things.

Perhaps the clearest effect that the introduction of nitrogen precursor into the reactors has is the shortening of the produced bundles (and thus also individual tubes). This should not be surprising, since any compounds which do not directly contribute to the growth of the carbon network will not only compete for absorption sites on the iron clusters, but at least in the case of ammonia, likely etch away carbon as well. Thus either a reduction in growth rate or an earlier termination of growth will undoubtedly lead to shorter bundles, which is detrimental for TCE performance. Although the effect seems to be correlated with the amount of nitrogen precursor, some reduction in bundle lengths seems inevitable.

Our analysis indicates that shortening bundle lengths alone were not enough to explain the drastically increasing sheet resistances in the HWG samples with increasing levels of ammonia. Based on our network simulations and the undoped samples with different bundle lengths, we could estimate that the figures of merit K of the 100 and 200 ppm NH_3 films were between 68% to 86% smaller than would be expected based on their measured average bundle lengths. Thus the measured resistances of the 100 and 200 ppm NH_3 films were 5 to 10 times larger than expected. The 300 ppm NH_3 bundles were already so short that they likely do not form a proper percolating network and the analysis is no longer applicable.

If we assume that the N dopants do not increase the junction resistances (rather, they could even decrease them [182]), it seems clear the conductivities of the bundles themselves decrease with doping. This can perhaps be attributed to an increasing number of randomly distributed scattering centers in the doped nanotubes, which decrease the mean free paths of the carriers [54, 55, 183, 184]. Another major question is the contribution of different local nitrogen bonding configurations to the scattering effect and the possible charge transfer to the nanotubes. Perhaps the negative effects observed here could be at least partially mitigated by controlling the balance of n- and p-type dopant configurations, but this appears experimentally quite challenging.

Whether the effect observed here is due to an increased number of defects not related to nitrogen or the actual dopant sites themselves is a topic for further research, though the non-increasing intensity of the Raman D band would suggest that the defect density is not significantly increased. However, we note that the bundles of doped tubes do seem to show fewer impurities on their surfaces, which could affect the measurements. Single tube transport or network transistor measurements would likely help elucidate the microscopic mechanism for the effect observed here for macroscopic films.

Remarkably, the undoped HWG films show even better optoelectronic properties than the previously reported ferrocene reactor films [118]. The higher performance of the undoped HWG samples compared to the ferrocene samples (with similar ~3 μm bundle length) can likely be explained by the smaller bundle diameters in the HWG samples, and thus smaller contact resistances between the bundles. Since the figure of merit K scales inversely with the contact resistance, we see that the undoped HWG samples would agree with the ferrocene data if we assumed that the contact resistances were 50% lower for the smaller HWG bundles. Nirmalraj et al. estimated [127] the resistance drop to be roughly 70% for the bundle diameters measured here (7.8 and 6.1 nm for the ferrocene and HWG samples, respectively); though we note that our largest bundles are at the lower end of their largest diameter category. Most importantly in the context of this work, we note that should the bundles of doped nanotubes with even smaller bundle diameters exhibit smaller contact resistances than the undoped ones, this would only further increase the deficit observed in the optoelectronic figures of merit of the films.

Based on these arguments, we do not envision that nitrogen-doped single-walled carbon nanotubes will be competitive in the race for the lowest resistance transparent coating. This is compounded by the fact that all of the best performance nanotube TCEs use some sort of acid treatments for achieving extremely large charge transfers onto their semiconducting tubes [118]. It is doubtful whether this large charge transfers would be possible with nitrogen doping even if the local doping configurations could be totally controlled. However, there are emerging applications in e.g. haptic displays where controlled higher resistances at a high transparency might actually be required, and these materials could find use there.

Thus we feel that the most promising avenues of research for N-SWCNTs lie in applications where – assuming this can be experimentally achieved – a stable, intrinsic n-type behavior is needed, such as transistors, or, alternatively, in applications where the inherent reactivity of the nitrogen sites is the crucial property of the N-SWCNT material, such as in sensors or in electrocatalysis.

4.4. Growth mechanism

In all cases where reaction barriers were extracted from the experimental Arrhenius plots, we had to assume that the reactions were first order. In practice, this means we considered reactions between adsorbed precursors (or their fragments), and not direct collisions of gas phase molecules with adsorbed reactants. Although it is not easy to directly justify this assumption, we feel it is likely true since the reactants quickly decompose on the catalyzer surfaces. Further work should be done to confirm the reaction orders. Also, we assumed that we had correctly identified the main reactions to study. Since these were the simplest possible reactions, and the only ones we could study comprehensively, the assumption was an unavoidable one. We feel that the correspondence between experiments and the theoretical calculations was sufficiently strong that it seems likely we captured to main features of the system. Of course, further studies could be envisaged to address more complex reactions.

The calculated barrier for NH_3 decomposition (1.0 eV) differs significantly from the measured one (0.43 eV). The small cluster used for the simulation presents high symmetry and limited size of the facet on which the reaction is constrained. Furthermore, it is also possible that the rate-limiting barrier for the cleaving of the final hydrogen would be slight lower if the calculation would be performed on a bigger, irregular cluster. Unfortunately the actual computational capability restricts the size of the simulated cluster to the one here used. The nitrogen in NH is tetrahedrally sp^3 coordinated and the final H is pointed away from the surface, making it more difficult to reach the surface. This is an artifact of the model cluster and most likely not relevant for a real particle, where a step or a defect would lower this barrier. In the reactive conditions at high temperature in the reactor, the suspended nanoparticle could also be at least in part melted, which we could not take into account in the simulations directly. Finally, considering that the theoretical and experimental data are not directly comparable because of the inability of the NEB results to incorporate entropy change, the simulations can be said to be consistent with the experiments.

Alternatives to the HCN formation reaction pathway we identified can be considered. The pathway HN + C is not relevant for direct hydrogen cyanide formation [185, 186], since the hydrogen in HCN is bonded to the carbon atom, not to the nitrogen (as in hydrogen isocyanide, HNC). Our FTIR measurements specifically detected the formation of HCN, and not HNC. Furthermore, although a formation path HC + N is common for HCN formation from hydrocarbon sources [185, 186], we do not consider it to be likely since no CH fragments are present in the precursors. Of course, the contribution of some multi-step pathways cannot be ruled out by the present work.

Thermodynamically, HCN could also be formed [187, 188] in a gas phase reaction between CO and NH_3. However, the formation of CH_4, N_2 and H_2O is the most favorable reaction. Although the formation of HCN is possible in the presence of H_2, that reaction should produce CH_4 as well [188], which we do not observe. We also note that the gas phase formation of HCN is typically not observed in non-hydrocarbon (CO + H_2) flames [189]. In any case, in the presence of a good catalyzer (such as the iron nanoparticles), the assisted reaction path can be expected to dominate.

In N-SWCNT synthesis, if the nitrogen feedrate is too large, nanotube growth was found to terminate. This can be either due to a saturation and breakdown of the hexagonal carbon network by nitrogen, or to nitrogen blocking the adsorption sites on the cluster and preventing the sufficient input of further carbon [190], slowing down and eventually stopping the growth. Another possibility is that NH_3 accelerates the production of active gaseous compounds, which compete with sp^2 bond formation (etching effect). If the feedrate is suitable, growth continues in the steady state, with the nanotube being continuously doped with nitrogen until the catalyst particle leaves the active zone of the reactor [138].

Considering these findings, we believe that the precursor decomposition reactions happen on the nanocluster itself, not at the open edge of the growing N-SWCNT (as proposed by Sumpter et al. [115]). At least in the case of carbon monoxide and ammonia [191], the calculated reaction barriers strongly suggest that the precursors do not significantly self-decompose without catalyst at the middle temperature region relevant for nanotube growth. Thus nitrogen is incorporated continuously into the nanotube at the root, not at the leading edge. Cap nucleation and detachment are likely similar to what has been proposed for SWCNTs [192, 193], as are the dynamics of the steady-state growth [40, 138, 194, 195]. Based on our current understanding we have developed a tentative growth model for N-SWCNT synthesis in the HWG reactor (Figure 4.1).

It seems that at least in the case of CO and NH_3 studied here, the chemistry involving C and N is quite similar. Considering further the barrierless C–N bond formation and the large barrier for parasitic HCN formation, there seems to be no fundamental differences in the mechanism of the precursor reactions. As for the sensitivity of SWCNTs to relatively low levels of nitrogen doping in contrast with the multiwalled case, it may be that N-MWCNTs can simply tolerate much larger amounts of N and the defects they entail for the graphitic lattice, while N-SWCNTs are more likely severely disturbed by even relatively small amounts of N during their nucleation and growth. Another contributing factor can be that the nitrogen atoms have more bonding options available in MWCNTs, involving cross-bonding and interstitials, which likely greatly increase the amount of nitrogen allowed while keeping the structure stable.

The next step in the simulations would be the study of the formation of larger fragments, such as C_2N, C_3N, and beyond. However, this would require larger facets than the Fe_{55} cluster permits. A larger cluster would in turn require at least a doubling of the number of iron atoms in the simulations, entailing an enormous increase in the computational resources required. This is currently just beyond our computational resources.

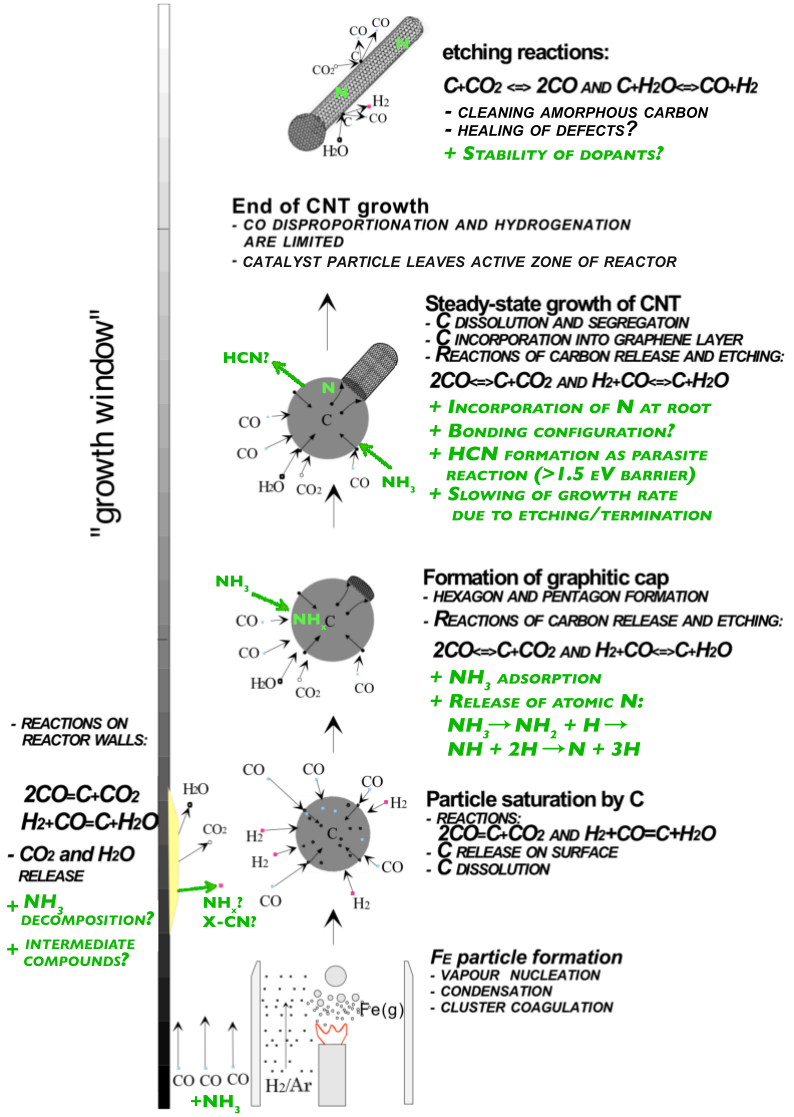

Figure 4.1 Proposed growth model for N-SWCNT synthesis in the HWG reactor. Green text denotes processes related to nitrogen. Adapted with permission from a model developed for pristine SWCNT synthesis [139].

5. Conclusions

Nitrogen-doped single-walled carbon nanotubes were synthesized using a floating catalyst CVD method using carbon monoxide and ammonia as precursors, and deposited from the gas phase as grown directly as films on different substrates. A variety of spectroscopic methods indicate the presence of nitrogen in the nanotubes. Analysis of the optoelectronic properties of the films shows that their sheet resistances are significantly higher than would be expected from their geometrical connectivity. This suggests that the intratube resistances are higher for doped tubes than for undoped ones. This work represents the first experimental report on macroscopic films of N-SWCNT.

Tailoring the chiral angle distribution of SWCNTs by introducing a certain amount of NH_3 into the ferrocene reactor was achieved as well. Unambiguous (*n,m*) determination based on electron diffraction analysis of a statistically significant number of individual SWCNTs demonstrates that the chiral species of SWCNTs, produced in the presence of 500 ppm NH_3, cluster intensively into a narrow region around the major (13,12) nanotube. The mechanism for such selectivity is not known for certain at the moment, although NH_3 etching effects have been preliminarily considered as one possible explanation.

Finally, the mechanism of the initial stages of nitrogen-doped single-walled carbon nanotube growth was studied in a system with the simplest possible experimentally feasible chemistry with the CO and NH_3 precursors. The dissociation reaction of NH_3 to atomic nitrogen and hydrogen was identified, with a reaction barrier comparable to an experimentally determined value measured by tandem infrared and mass spectrometry. It was found that the chemistry involving C and N is rather similar. The formation of a C–N bond between atomic carbon and nitrogen was also found to be barrierless and exothermic, while there is a large barrier for parasitic HCN formation. Thus there seems to be no fundamental differences in the mechanism of the precursor reactions. This work marks the first explicit study of the initial stages of N-SWCNT growth.

6. References

[1] S. Iijima, Nature, **354**, 56 (1991).

[2] U.O. Waterloo. *Hybrid Orbitals in Carbon Compounds*. 2011 [cited 2011 April 1]; Available from: http://www.science.uwaterloo.ca/~cchieh/cact/c120/hybridcarbon.html.

[3] User:Vladsinger. *Image:Benzene Orbitals.Svg*. [cited 2011 April 1]; CC]. Available from: http://commons.wikimedia.org/wiki/File:Benzene_Orbitals.svg.

[4] S. Iijima, and T. Ichihashi, Nature, **363**, 603 (1993).

[5] D.S. Bethune, C.H. Klang, M.S. De Vries, G. Gorman, R. Savoy, J. Vazquez, and R. Beyers, Nature, **363**, 605 (1993).

[6] T. Hayashi, Y.A. Kim, T. Matoba, M. Esaka, K. Nishimura, T. Tsukada, M. Endo, and M.S. Dresselhaus, Nano Lett., **3**, 887 (2003).

[7] N. Wang, Z.K. Tang, G.D. Li, and J.S. Chen, Nature, **408**, 50 (2000).

[8] X. Wang, Q. Li, J. Xie, Z. Jin, J. Wang, Y. Li, K. Jiang, and S. Fan, Nano Lett., **9**, 3137 (2009).

[9] A.K. Geim, and K.S. Novoselov, Nat. Mater, **6**, 183 (2007).

[10] P.R. Wallace, Phys. Rev., **71**, 622 (1947).

[11] K.S. Novoselov, A.K. Geim, S.V. Morozov, D. Jiang, M.I. Katsnelson, I.V. Grigorieva, S.V. Dubonos, and A.A. Firsov, Nature, **438**, 197 (2005).

[12] R. Saito, G. Dresselhaus, and M.S. Dresselhaus, Phys. Rev. B, **61**, 2981 (2000).

[13] N. Hamada, S.-I. Sawada, and A. Oshiyama, Phys. Rev. Lett., **68**, 1579 (1992).

[14] User:Paulo. *Densidade-Estado.Jpg*. 2008 [cited 2011 April 1]; Available from: https://picasaweb.google.com/paulogomestl/Profissional#5414495591158946882.

[15] R.R. Nair, P. Blake, A.N. Grigorenko, K.S. Novoselov, T.J. Booth, T. Stauber, N.M.R. Peres, and A.K. Geim, Science, **320**, 1308 (2008).

[16] M.S. Dresselhaus, G. Dresselhaus, R. Saito, and A. Jorio, Annu. Rev. Phys. Chem., **58**, 719 (2007).

[17] T. Michel, M. Paillet, J.C. Meyer, V.N. Popov, L. Henrard, and J.L. Sauvajol, Phys. Rev. B, **75**, 155432 (2007).

[18] A. Jorio, R. Saito, G. Dresselhaus, and M.S. Dresselhaus, Philos. Trans. R. Soc. London, Ser. A, **362**, 2311 (2004).
[19] C. Thomsen, S. Reich, and J. Maultzsch, Phil. Trans. R. Soc. Lond. A, **362**, 2337 (2004).
[20] S.D.M. Brown, A. Jorio, P. Corio, M.S. Dresselhaus, G. Dresselhaus, R. Saito, and K. Kneipp, Phys. Rev. B, **63**, 155414 (2001).
[21] M. Lucchese, F. Stavale, E. Ferreira, C. Vilani, M. Moutinho, R.B. Capaz, C. Achete, and A. Jorio, Carbon, **48**, 1592 (2010).
[22] I.W. Chiang, B.E. Brinson, A.Y. Huang, P.A. Willis, M.J. Bronikowski, J.L. Margrave, R.E. Smalley, and R.H. Hauge, J. Phys. Chem. B, **105**, 8297 (2001).
[23] Y.-L. Li, L.-H. Zhang, X.-H. Zhong, and A.H. Windle, Nanotechnology, **18**, 225604 (2007).
[24] J.E. Herrera, L. Balzano, F. Pompeo, and D.E. Resasco, J. Nanosci. Nanotechnol., **3**, 133 (2003).
[25] D.N. Futaba, K. Hata, T. Yamada, T. Hiraoka, Y. Hayamizu, Y. Kakudate, O. Tanaike, H. Hatori, M. Yumura, and S. Iijima, Nat. Mater., **5**, 987 (2006).
[26] M. Kalbac, Y.-P. Hsieh, H. Farhat, L. Kavan, M. Hofmann, J. Kong, and M.S. Dresselhaus, Nano Lett., **10**, 4619 (2010).
[27] M. Kalbac, and L. Kavan, Carbon, **48**, 7 (2010).
[28] A. Hartschuh, H.N. Pedrosa, L. Novotny, and T.D. Krauss, Science, **301**, 1354 (2003).
[29] T.W. Ebbesen, and P.M. Ajayan, Nature, **358**, 220 (1992).
[30] T. Guo, P. Nikolaev, A. Thess, D.T. Colbert, and R.E. Smalley, Chem. Phys. Lett., **243**, 49 (1995).
[31] M. Kumar, and Y. Ando, J. Nanosci. Nanotechnol., **10**, 3739 (2010).
[32] Y. Fan, B.R. Goldsmith, and P.G. Collins, Nat. Mater., **4**, 906 (2005).
[33] P. Nikolaev, M.J. Bronikowski, R.K. Bradley, F. Rohmund, D.T. Colbert, K.A. Smith, and R.E. Smalley, Chem. Phys. Lett., **313**, 91 (1999).
[34] H. Dai, A.G. Rinzler, P. Nikolaev, A. Thess, D.T. Colbert, and R.E. Smalley, Chem. Phys. Lett., **260**, 471 (1996).
[35] D.E. Resasco, W.E. Alvarez, F. Pompeo, L. Balzano, J.E. Herrera, B. Kitiyanan, and A. Borgna, J. Nanopart. Res., **4**, 131 (2002).
[36] A.G. Nasibulin, D.P. Brown, P. Queipo, D. Gonzalez, H. Jiang, and E.I. Kauppinen, Chem. Phys. Lett., **417**, 179 (2006).
[37] D. Takagi, Y. Homma, H. Hibino, S. Suzuki, and Y. Kobayashi, Nano Lett., **6**, 2642 (2006).
[38] B. Liu, W. Ren, L. Gao, S. Li, S. Pei, C. Liu, C. Jiang, and H.-M. Cheng, JACS, **131**, 2082 (2009).
[39] S. Huang, Q. Cai, J. Chen, Y. Qian, and L. Zhang, JACS, **131**, 2094 (2009).

[40] A.G. Nasibulin, and S.D. Shandakov, *Aerosol Synthesis of Single-Walled Carbon Nanotubes*. Aerosols - Science and Technology. 2010: Wiley-VCH Verlag GmbH & Co. KGaA. 65.

[41] M. Daenen, R.D. De Fouw, B. Hamers, P.G.A. Janssen, K. Schouteden, and M.a.J. Veld, *The Wondrous World of Carbon Nanotubes: A Review of Current Nanotube Technologies*. 2003.

[42] P.J.F. Harris, Carbon, **45**, 229 (2007).

[43] F. Ding, K. Bolton, and A. Rosén, J. Phys. Chem. B, **108**, 17369 (2004).

[44] F. Ding, K. Bolton, and A. Rosen, Comp. Mat. Sci., **35**, 243 (2006).

[45] J.-Y. Raty, F. Gygi, Ccedil, Ois, and G. Galli, Phys. Rev. Lett., **95**, 096103 (2005).

[46] X. Li, X. Tu, S. Zaric, K. Welsher, W.S. Seo, W. Zhao, and H. Dai, JACS, **129**, 15770 (2007).

[47] L. Ding, A. Tselev, J. Wang, D. Yuan, H. Chu, T.P. Mcnicholas, Y. Li, and J. Liu, Nano Lett., **9**, 800 (2009).

[48] S.M. Bachilo, L. Balzano, J.E. Herrera, F. Pompeo, D.E. Resasco, and R.B. Weisman, JACS, **125**, 11186 (2003).

[49] R. Jasti, and C.R. Bertozzi, Chem. Phys. Lett., **494**, 1 (2010).

[50] A.R. Harutyunyan, G. Chen, T.M. Paronyan, E.M. Pigos, O.A. Kuznetsov, K. Hewaparakrama, S.M. Kim, D. Zakharov, E.A. Stach, and G.U. Sumanasekera, Science, **326**, 116 (2009).

[51] L. Qu, F. Du, and L. Dai, Nano Lett., **8**, 2682 (2008).

[52] Y. Li, D. Mann, M. Rolandi, W. Kim, A. Ural, S. Hung, A. Javey, J. Cao, D. Wang, E. Yenilmez, Q. Wang, J.F. Gibbons, Y. Nishi, and H. Dai, Nano Lett., **4**, 317 (2004).

[53] O. Stephan, P.M. Ajayan, C. Colliex, P. Redlich, J.M. Lambert, P. Bernier, and P. Lefin, Science, **266**, 1683 (1994).

[54] J. Ma, S. Guan, and C.-H. Lai, Phys. Rev. B, **74**, 205401 (2006).

[55] H.J. Choi, J. Ihm, S.G. Louie, and M.L. Cohen, Phys. Rev. Lett., **84**, 2917 (2000).

[56] P. Ayala, R. Arenal, A. Loiseau, A. Rubio, and T. Pichler, Rev. Mod. Phys., **82**, 43 (2010).

[57] R. Arenal, X. Blase, and A. Loiseau, Adv. Phys., **59**, 101 (2010).

[58] J.Y. Yi, and J. Bernholc, Phys. Rev. B, **47**, 1708 (1993).

[59] D. Wei, Y. Liu, Y. Wang, H. Zhang, L. Huang, and G. Yu, Nano Lett., **9**, 1752 (2009).

[60] L. Panchakarla, K. Subrahmanyam, S. Saha, A. Govindaraj, H. Krishnamurthy, U. Waghmare, and C. Rao, Adv. Mater., **21**, 4726 (2009).

[61] A.L. ElíAs, A.R. Botello-Méndez, D. Meneses-Rodríguez, V. Jehová González, D. Ramírez-González, L. Ci, E. Muñoz-Sandoval, P.M. Ajayan, H. Terrones, and M. Terrones, Nano Lett., **10**, 366 (2009).

[62] D. Yu, E. Nagelli, F. Du, and L. Dai, J. Phys. Chem. Lett., **1**, 2165 (2010).
[63] P. Ayala, R. Arenal, M.H. Rümmeli, A. Rubio, and T. Pichler, Carbon, **48**, 585 (2010).
[64] D. Golberg, Y. Bando, W. Han, K. Kurashima, and T. Sato, Chem. Phys. Lett., **308**, 337 (1999).
[65] D. Golberg, Y. Bando, L. Bourgeois, K. Kurashima, and T. Sato, Carbon, **38**, 2017 (2000).
[66] U. Bangert, A. Bleloch, M. Gass, A. Seepujak, and J. Van Den Berg, Phys. Rev. B, **81**, 245423 (2010).
[67] F. Xu, M. Minniti, C. Giallombardo, A. Cupolillo, P. Barone, A. Oliva, and L. Papagno, Surf. Sci., **601**, 2819 (2007).
[68] B. Zheng, P. Hermet, and L. Henrard, ACS Nano, **4**, 4165 (2010).
[69] A.H. Nevidomskyy, G. Csanyi, and M.C. Payne, Phys. Rev. Lett., **91**, 105502 (2003).
[70] C.P. Ewels, and M. Glerup, J. Nanosci. Nanotechnol., **5**, 1345 (2005).
[71] A. Rocha, M. Rossi, A. Silva, and A. Fazzio, Journal of Physics D: Appl. Phys., **43**, 374002 (2010).
[72] I. Gerber, P. Puech, A. Gannouni, and W. Bacsa, Phys. Rev. B, **79**, 075423 (2009).
[73] D. Deng, X. Pan, L. Yu, Y. Cui, Y. Jiang, J. Qi, W.-X. Li, Q. Fu, X. Ma, Q. Xue, G. Sun, and X. Bao, Chem. Mater., **23**, 1188 (2011).
[74] B. Cordero, V. Gomez, A.E. Platero-Prats, M. Reves, J. Echeverria, E. Cremades, F. Barragan, and S. Alvarez, J. Chem. Soc., Dalton Trans., 2832 (2008).
[75] R. Czerw, M. Terrones, J.C. Charlier, X. Blase, B. Foley, R. Kamalakaran, N. Grobert, H. Terrones, D. Tekleab, P.M. Ajayan, W. Blau, M. Ruhle, and D.L. Carroll, Nano Lett., **1**, 457 (2001).
[76] H. Kang, and S. Jeong, Phys. Rev. B, **70**, 233411 (2004).
[77] V. Krstic, G.L.J.A. Rikken, P. Bernier, S. Roth, and M. Glerup, Europhys. Lett., **77**, (2007).
[78] H. Lin, J. Lagoute, C. Chacon, R. Arenal, O. Stéphan, V. Repain, Y. Girard, S. Enouz, L. Bresson, and S. Rousset, Phys. Status Solidi B, **245**, 1986 (2008).
[79] A.G. Kudashov, A.V. Okotrub, L.G. Bulusheva, L.P. Asanov, Y.V. Shubin, N.F. Yudanov, L.I. Yudanova, V.S. Danilovich, and O.G. Abrosimov, J. Phys. Chem. B, **108**, 9048 (2004).
[80] C.H. Lin, H.L. Chang, C.M. Hsu, A.Y. Lo, and C.T. Kuo, Diam. Relat. Mater., **12**, 1851
[81] D. Deng, X. Pan, L. Yu, Y. Cui, Y. Jiang, J. Qi, W.X. Li, Q. Fu, X. Ma, and Q. Xue, Chem. Mater., **23**, 1188 (2011).

[82] P. Ayala, A. Gruneis, T. Gemming, D. Grimm, C. Kramberger, M.H. Rummeli, F.L. Freire Jr, H. Kuzmany, R. Pfeiffer, and A. Barreiro, J. Phys. Chem. C, **111**, 2879 (2007).

[83] A.L. Elías, P. Ayala, A. Zamudio, M. Grobosch, E. Cruz-Silva, J.M. Romo-Herrera, J. Campos-Delgado, H. Terrones, T. Pichler, and M. Terrones, J. Nanosci. Nanotechnol., **10**, 3959 (2010).

[84] K. Suenaga, Y. Sato, Z. Liu, H. Kataura, T. Okazaki, K. Kimoto, H. Sawada, T. Sasaki, K. Omoto, T. Tomita, T. Kaneyama, and Y. Kondo, Nat. Chem., **1**, 415 (2009).

[85] S. Latil, S. Roche, D. Mayou, and J.-C. Charlier, Phys. Rev. Lett., **92**, 256805 (2004).

[86] F. Villalpando-Paez, A. Zamudio, A.L. Elias, H. Son, E.B. Barros, S.G. Chou, Y.A. Kim, H. Muramatsu, T. Hayashi, J. Kong, H. Terrones, G. Dresselhaus, M. Endo, M. Terrones, and M.S. Dresselhaus, Chem. Phys. Lett., **424**, 345 (2006).

[87] E. Ibrahim, V. Khavrus, and A. Leonhardt, Diam. Relat. Mater., **19**, 1199 (2010).

[88] Y.S. Min, E.J. Bae, I.P. Asanov, U.J. Kim, and W. Park, Nanotechnology, **18**, 285601 (2007).

[89] G. Keskar, R. Rao, J. Luo, J. Hudson, J. Chen, and A.M. Rao, Chem. Phys. Lett., **412**, 269 (2005).

[90] E. Ibrahim, V. Khavrus, and A. Leonhardt, Diam. Relat. Mater., **19**, 1199 (2010).

[91] H. Liu, Y. Zhang, R. Li, X. Sun, S. Désilets, H. Abou-Rachid, M. Jaidann, and L.-S. Lussier, Carbon, **48**, 1498 (2009).

[92] Q.H. Yang, P.X. Hou, M. Unno, S. Yamauchi, R. Saito, and T. Kyotani, Nano Lett., **5**, 2465 (2005).

[93] P. Ayala, A. Grueneis, T. Gemming, B. Buchner, M.H. Rummeli, D. Grimm, J. Schumann, R. Kaltofen, F.L. Freire, H.D. Fonseca, and T. Pichler, Chem. Mater., **19**, 6131 (2007).

[94] I.O. Maciel, N. Anderson, M.A. Pimenta, A. Hartschuh, H. Qian, M. Terrones, H. Terrones, J. Campos-Delgado, A.M. Rao, L. Novotny, and A. Jorio, Nat. Mater., **7**, 878 (2008).

[95] Y. Ganesan, C. Peng, Y. Lu, L. Ci, A. Srivastava, P.M. Ajayan, and J. Lou, ACS Nano, **4**, 7637 (2010).

[96] A.A. Koós, M. Dowling, K. Jurkschat, A. Crossley, and N. Grobert, Carbon, **47**, 30 (2009).

[97] M. Glerup, J. Steinmetz, D. Samaille, O. Stephan, S. Enouz, A. Loiseau, S. Roth, and P. Bernier, Chem. Phys. Lett., **387**, 193 (2004).

[98] T. Loponen, A.V. Krasheninnikov, M. Kaukonen, and R.M. Nieminen, Phys. Rev. B, **74**, 073409 (2006).

[99] J. Kotakoski, C. Jin, O. Lehtinen, K. Suenaga, and A. Krasheninnikov, Phys. Rev. B, **82**, 113404 (2010).

[100] J.M. Jones, R.P. Malcolm, K.M. Thomas, and S.H. Bottrell, Carbon, **34**, 231 (1996).

[101] R.Q. Yun, M.X. Zhan, D.D. Cheng, S.Y. Yang, Z.Y. Liu, and L.S. Zheng, J. Phys. Chem., **99**, 1818 (1995).

[102] M.X. Zhan, R.Q. Yu, Y.H. Wang, S.Y. Yang, D.D. Cheng, C.Y. Liu, and L.S. Zheng, Chem. J. Chinese U., **16**, 1780 (1995).

[103] M. Yudasaka, R. Kikuchi, Y. Ohki, and S. Yoshimura, Carbon, **35**, 195 (1997).

[104] R. Sen, B. C. Satishkumar, A. Govindaraj, K. R. Harikumar, M. K. Renganathan, and C. N. R. Rao, J. Mater. Chem., **7**, 2335 (1997).

[105] M. Terrones, H. Terrones, N. Grobert, W.K. Hsu, Y.Q. Zhu, J.P. Hare, H.W. Kroto, D.R.M. Walton, P. Kohler-Redlich, M. Ruhle, J.P. Zhang, and A.K. Cheetham, Appl. Phys. Lett., **75**, 3932 (1999).

[106] Keywords Used:
CNTs: Topic=(carbon nanotubes OR graphitic microtubules OR graphene tubules);
Graphene: Title=(graphene NOT graphene tubules NOT carbon nanotube);
N-graphene: Title=(graphene) AND Topic=(nitrogen-doped OR N-doped OR CNx);
N-CNTs: Topic=(nitrogen-doped OR N-doped OR CNx AND carbon nanotubes);
N-SWCNTs: Topic=(nitrogen-doped OR N-doped OR CNx AND carbon nanotubes) AND Topic=(single-walled OR SW* OR CNx-SW*)

[107] M. Terrones, A. Filho, and A. Rao, *Doped Carbon Nanotubes: Synthesis, Characterization and Applications*, in *Carbon Nanotubes*. 2008, Springer Berlin / Heidelberg. p. 531.

[108] P. Ayala, R. Arenal, M. Rümmeli, A. Rubio, and T. Pichler, Carbon, **48**, 585 (2010).

[109] H. Lin, R. Arenal, S. Enouz-Vedrenne, O. Stephan, and A. Loiseau, J. Phys. Chem. C, **113**, 9509 (2009).

[110] P. Ayala, A. Grüneis, C. Kramberger, M.H. Rümmeli, I.G. Solorzano, F.L. Freire Jr, and T. Pichler, J. Chem. Phys., **127**, 184709 (2007).

[111] C.P. Ewels, M. Glerup, and V. Krstic, *Nitrogen and Boron Doping in Carbon Nanotubes*, in *Chemistry of Carbon Nanotubes*, V.A. Basiuk and E.V. Basiuk, Editors. 2008, American Scientific Publishers.

[112] R. Arenal, and A. Loiseau, Heteroatomic Single-Wall Nanotubes Made of Boron, Carbon, and Nitrogen, in B-C-N Nanotubes and Related Nanostructures. 2009, Springer New York. p. 45.

[113] K. Suenaga, M. Yudasaka, C. Colliex, and S. Iijima, Chem. Phys. Lett., **316**, 365 (2000).

[114] S. Trasobares, O. Stephan, C. Colliex, W.K. Hsu, H.W. Kroto, and D.R.M. Walton, J. Chem. Phys., **116**, 8966 (2002).

[115] B.G. Sumpter, J. Huang, V. Meunier, J.M. Romo-Herrera, E. Cruz-Silva, H. Terrones, and M. Terrones, Int. J. Quantum Chem., **109**, 97 (2009).

[116] A.G. Nasibulin, A. Moisala, D. Brown, H. Jiang, and E.I. Kauppinen, Chem. Phys. Lett., **402**, 227 (2005).

[117] Z. Wu, Z. Chen, X. Du, J.M. Logan, J. Sippel, M. Nikolou, K. Kamaras, J.R. Reynolds, D.B. Tanner, A.F. Hebard, and A.G. Rinzler, Science, **305**, 1273 (2004).

[118] A. Kaskela, A.G. Nasibulin, M. Timmermans, B. Aitchison, A. Papadimitratos, Y. Tian, H. Jiang, D. Brown, A. Zakhidov, and E.I. Kauppinen, Nano Lett., **10**, 4349 (2010).

[119] E. Artukovic, M. Kaempgen, D.S. Hecht, S. Roth, and G. Grüner, Nano Lett., **5**, 757 (2005).

[120] M.Y. Zavodchikova, T. Kulmala, A.G. Nasibulin, V. Ermolov, S. Franssila, K. Grigoras, and E.I. Kauppinen, Nanotechnology, **20**, 085201 (2009).

[121] D.-M. Sun, M.Y. Timmermans, Y. Tian, A.G. Nasibulin, E.I. Kauppinen, S. Kishimoto, T. Mizutani, and Y. Ohno, Nat. Nanotechnol., **6**, 156 (2011).

[122] C.M. Aguirre, S. Auvray, S. Pigeon, R. Izquierdo, P. Desjardins, and R. Martel, Appl. Phys. Lett., **88**, 183104 (2006).

[123] E.S. Snow, F.K. Perkins, E.J. Houser, S.C. Badescu, and T.L. Reinecke, Science, **307**, 1942 (2005).

[124] A. Kumar, and C. Zhou, ACS Nano, **4**, 11 (2010).

[125] J. Van De Lagemaat, D. Levi, G. Rumbles, T.J. Coutts, C.L. Weeks, D.A. Britz, I. Levitsky, J. Peltola, and P. Glatkowski, Phys. Rev. B, **75**, 235410 (2007).

[126] J. Vavro, N.M. Nemes, J.E. Fischer, F. Borondics, K. Kamarás, and D.B. Tanner, Phys. Rev. B, **71**, 205423 (2005).

[127] P.N. Nirmalraj, P.E. Lyons, S. De, J.N. Coleman, and J.J. Boland, Nano Lett., **9**, 6 (2009).

[128] J. Wiggins-Camacho, and K. Stevenson, J. Phys. Chem. C, **113**, 9 (2009).

[129] F. Villalpando-P·Ez, A.H. Romero, E. Muòoz-Sandoval, L.M. Martìnez, H. Terrones, and M. Terrones, Chem. Phys. Lett., **386**, 137 (2004).

[130] K. Gong, F. Du, Z. Xia, M. Durstock, and L. Dai, Science, **323**, 760 (2009).

[131] H.M. Cheng, F. Li, G. Su, H.Y. Pan, L.L. He, X. Sun, and M.S. Dresselhaus, Appl. Phys. Lett., **72**, 3282 (1998).

[132] B.C. Satishkumar, A. Govindaraj, R. Sen, and C.N.R. Rao, Chem. Phys. Lett., **293**, 47 (1998).
[133] K. Bladh, L.K.L. Falk, and F. Rohmund, Appl. Phys. A, **70**, 317 (2000).
[134] A. Moisala, A.G. Nasibulin, D.P. Brown, H. Jiang, L. Khriachtchev, and E.I. Kauppinen, Chem. Eng. Sci., **61**, 4393 (2006).
[135] L.S. Panchalkarla, A. Govindaraj, and C.N.R. Rao, ACS Nano, **1**, 494 (2007).
[136] T. Susi, A.G. Nasibulin, P. Ayala, Y. Tian, Z. Zhu, H. Jiang, C. Roquelet, D. Garrot, J.S. Lauret, and E.I. Kauppinen, Phys. Status Solidi B, **246**, 2507 (2009).
[137] J. Huang, Q. Zhang, M. Zhao, and F. Wei, Nano Res., **2**, 872 (2009).
[138] A.S. Anisimov, A.G. Nasibulin, H. Jiang, P. Launois, J. Cambedouzou, S.D. Shandakov, and E.I. Kauppinen, Carbon, **48**, 9 (2010).
[139] A.G. Nasibulin, S.D. Shandakov, M. Zavodchikova, and E.I. Kauppinen, Rus. Chem. Rev., accepted, (2011).
[140] F. Mercuri, J. Phys. Chem. C, **114**, 21322 (2010).
[141] B. Xiao, J.-X. Zhao, Y.-H. Ding, and C.-C. Sun, Chem. Phys. Chem., **11**, 3505 (2010).
[142] A.G. Nasibulin, S.D. Shandakov, A.S. Anisimov, D. Gonzalez, H. Jiang, M. Pudas, P. Queipo, and E.I. Kauppinen, J. Phys. Chem. C, **112**, 5762 (2008).
[143] A.G. Nasibulin, A. Ollikainen, A.S. Anisimov, D.P. Brown, P.V. Pikhitsa, S. Holopainen, J.S. Penttilä, P. Helistö, J. Ruokolainen, M. Choi, and E.I. Kauppinen, Chem. Eng. J., **136**, 409 (2008).
[144] K. Oura, V.G. Lifshits, A.A. Saranin, A.V. Zotov, and M. Katayama, *Surface Science, an Introduction*. 2003: Springer.
[145] S. Hamalainen, *Carbon Nanotube Supported Catalyst Nanoparticles for Fuel Cell Applications*. 2007, Helsinki University of Technology.
[146] M. Haider, S. Uhlemann, E. Schwan, H. Rose, B. Kabius, and K. Urban, Nature, **392**, 768 (1998).
[147] O.L. Krivanek, M.F. Chisholm, V. Nicolosi, T.J. Pennycook, G.J. Corbin, N. Dellby, M.F. Murfitt, C.S. Own, Z.S. Szilagyi, M.P. Oxley, S.T. Pantelides, and S.J. Pennycook, Nature, **464**, 571 (2010).
[148] H. Jiang, A.G. Nasibulin, D. Brown, and E.I. Kauppinen, Carbon, **45**, 662 (2007).
[149] Z. Liu, and L.-C. Qin, Chem. Phys. Lett., **408**, 75 (2005).
[150] X. Liu, T. Pichler, M. Knupfer, M.S. Golden, J. Fink, H. Kataura, and Y. Achiba, Phys. Rev. B, **66**, 045411 (2002).

[151] Y. Tian, H. Jiang, J.V. Pfaler, Z. Zhu, A.G. Nasibulin, T. Nikitin, B. Aitchison, L. Khriachtchev, D.P. Brown, and E.I. Kauppinen, J. Phys. Chem. Lett., **1**, 1143 (2010).

[152] H. Kataura, Y. Kumazawa, Y. Maniwa, I. Umezu, S. Suzuki, Y. Ohtsuka, and Y. Achiba, Synth. Metals, **103**, 2555 (1999).

[153] V.N. Popov, New J. Phys., **6**, 17 (2004).

[154] C.L. Kane, and E.J. Mele, Phys. Rev. Lett., **93**, 197402 (2004).

[155] C. Fantini, A. Jorio, M. Souza, M.S. Strano, M.S. Dresselhaus, and M.A. Pimenta, Phys. Rev. Lett., **93**, 147406 (2004).

[156] User:Jon_Chui. *Image:Spectroscopy Overview.Svg*. [cited 2011 March 9]; CC]. Available from: http://commons.wikimedia.org/wiki/File:Interferometer.svg.

[157] C. Jeanguillaume, and C. Colliex, Ultramicroscopy, **28**, 252 (1989).

[158] R. Arenal, F. De La Pena, O. Stephan, M. Walls, M. Tence, A. Loiseau, and C. Colliex, Ultramicroscopy, **109**, 32 (2008).

[159] T.W. Odom, J.-L. Huang, P. Kim, and C.M. Lieber, Nature, **391**, 62 (1998).

[160] J.W.G. Wilder, L.C. Venema, A.G. Rinzler, R.E. Smalley, and C. Dekker, Nature, **391**, 59 (1998).

[161] P.E. Lyons, S. De, F. Blighe, V. Nicolosi, L.F.C. Pereira, M.S. Ferreira, and J.N. Coleman, Journal of Appl. Phys., **104**, 044302 (2008).

[162] User:Stannered. *Image:Interferometer.Png*. [cited 2011 March 9]; CC]. Available from: http://commons.wikimedia.org/wiki/File:Interferometer.svg.

[163] P.J. De Pablo, M.T. Martínez, J. Colchero, J. Gómez-Herrero, W.K. Maser, A.M. Benito, E. Muñoz, and A.M. Baró, Adv. Mater., **12**, 573 (2000).

[164] W. Kohn, Rev. Mod. Phys., **71**, 1253 (1999).

[165] P.E. Blöchl, Phys. Rev. B, **50**, 17953 (1994).

[166] J. Mortensen, L. Hansen, and K. Jacobsen, Phys. Rev. B, **71**, 035109 (2005).

[167] G. Kresse, and J. Hafner, J. Phys. Condens. Matter, **6**, 8245 (1994).

[168] G. Lanzani, A.G. Nasibulin, K. Laasonen, and E.I. Kauppinen, Nano Res., **2**, 660 (2009).

[169] G. Lanzani, A.G. Nasibulin, K. Laasonen, and E.I. Kauppinen, J. Phys. Chem. C, **113**, 12939 (2009).

[170] B. Hammer, L. Hansen, and J. Nørskov, Phys. Rev. B, **59**, 7413 (1999).

[171] G. Henkelman, B. Uberuaga, and H. Jónsson, J. Chem. Phys., **113**, 9901 (2000).

[172] F. Ding, A.R. Harutyunyan, and B.I. Yakobson, PNAS, **106**, 2506 (2009).

[173] A.G. Souza Filho, A. Jorio, G.G. Samsonidze, G. Dresselhaus, M.A. Pimenta, M.S. Dresselhaus, A.K. Swan, Uuml, Nl, M. S., B.B. Goldberg, and R. Saito, Phys. Rev. B, **67**, 035427 (2003).

[174] G. Henkelman, and H. Jónsson, J. Chem. Phys., **113**, 9978 (2000).

[175] E. Bitzek, P. Koskinen, F. Gähler, M. Moseler, and P. Gumbsch, Phys. Rev. Lett., **97**, 170201 (2006).

[176] P. Li, D.E. Miser, S. Rabiei, R.T. Yadav, and M.R. Hajaligol, Appl. Cat. B: Environ., **43**, 151 (2003).

[177] U. Borstnik, M. Hodoscek, D. Janezic, and I.N. Lukovits, Chem. Phys. Lett., **411**, 384 (2005).

[178] O. Gülseren, T. Yildirim, and S. Ciraci, Phys. Rev. B, **65**, 153405 (2002).

[179] R. Arenal, M. Kociak, A. Loiseau, and D.J. Miller, Appl. Phys. Lett., **89**, 073104 (2006).

[180] X. Blase, J.C. Charlier, A. De Vita, R. Car, P. Redlich, M. Terrones, W.K. Hsu, H. Terrones, D.L. Carroll, and P.M. Ajayan, Phys. Rev. Lett., **83**, 5078 (1999).

[181] E.S. Snow, J.P. Novak, P.M. Campbell, and D. Park, Appl. Phys. Lett., **82**, 2145 (2003).

[182] A.H. Nevidomskyy, Cs, Aacute, G. Nyi, Bor, and M.C. Payne, Phys. Rev. Lett., **91**, 105502 (2003).

[183] R. Avriller, S. Latil, F. Triozon, X. Blase, and S. Roche, Phys. Rev. B, **74**, 121406 (2006).

[184] A. Lopez-Bezanilla, X. Blase, and S. Roche, Nano Res., **3**, 288 (2010).

[185] R.M. Van Hardeveld, R.A. Van Santen, and J.W. Niemantsverdriet, J. Phys. Chem. B, **101**, 7901 (1997).

[186] S. Delagrange, and Y. Schuurman, Cat. Today, **121**, 204 (2007).

[187] G. Schlesinger, and S.L. Miller, J. Molec. Evol., **19**, 383 (1983).

[188] N. Aylward, *The Synthesis of Biological Molecules in the Universe*, in *Proceedings of the 10th WSEAS International Conference on Mathematical Methods and Computational Techniques in Electrical Engineering*. 2008, World Scientific and Engineering Academy and Society (WSEAS): Sofia, Bulgaria. p. 267.

[189] T. Takagi, T. Tatsumi, and M. Ogasawara, Combust. Flame, **35**, 17 (1979).

[190] A. Harutyunyan, N. Awasthi, A. Jiang, W. Setyawan, E. Mora, T. Tokune, K. Bolton, and S. Curtarolo, Phys. Rev. Lett., **100**, 195502 (2008).

[191] T. Susi, Z. Zhu, G. Ruiz-Soria, R. Arenal, P. Ayala, A.G. Nasibulin, H. Lin, H. Jiang, O. Stephan, T. Pichler, A. Loiseau, and E.I. Kauppinen, Phys. Status Solidi B, **247**, 2726 (2010).

[192] Y. Ohta, Y. Okamoto, A. Page, S. Irle, and K. Morokuma, ACS Nano, **3**, 8 (2009).

[193] M. Moors, H. Amara, T. Visart De Bocarmé, C. Bichara, F. Ducastelle, N. Kruse, and J.-C. Charlier, ACS Nano, **3**, 6 (2009).

[194] Y. Shibuta, and S. Maruyama, Chem. Phys. Lett., **382**, 381 (2003).

[195] S. Irle, Y. Ohta, Y. Okamoto, A.J. Page, Y. Wang, and K. Morokuma, Nano Res., **2**, 755 (2009).

Carbon nanotubes are one of the most exciting materials for emerging practical nanotechnologies. However, a significant issue for applications is the mixture of semiconducting and metallic tubes in all typical samples. One of the proposed solutions for this problem, drawing inspiration from semiconductor technology, is to tailor the electronic structure by doping the lattice with heteroatoms, most notably nitrogen. In this thesis, thin films of nitrogen-doped single-walled carbon nanotubes (N-SWCNTs) were synthesized using a novel combination of precursors in an ambient pressure floating catalyst chemical vapor deposition reactor. The mechanism of the initial stages of their growth was also studied using tandem infrared and mass spectrometry gas measurements and first principles electronic-structure calculations. This work represents the first experimental report on macroscopic N-SWCNT thin films.

Aalto-DD 41/2011

ISBN: 978-952-60-4124-7 (pdf)
ISBN: 978-952-60-4123-0
ISSN-L: 1799-4934
ISSN: 1799-4942 (pdf)
ISSN: 1799-4934

Aalto University
School of Science
Department of Applied Physics
www.aalto.fi

BUSINESS + ECONOMY

ART + DESIGN + ARCHITECTURE

SCIENCE + TECHNOLOGY

CROSSOVER

DOCTORAL DISSERTATIONS